KU LEUVEN

FACULTEIT WETENSCHAPPEN

Tb radioisotopes for medical applications

Spallation cross section measurements and first isotope delivery from CERN-MEDICIS

Hannelore VERHOEVEN

Promotor: Prof. T. E. Cocolios
Instituut voor kern- en stralingsfysica
(KU Leuven)

Begeleider: K. Dockx
Instituut voor kern- en stralingsfysica
(KU Leuven)

Proefschrift ingediend tot het
behalen van de graad van
Master of Science in Physics

Academiejaar 2017-2018

Preface

During this master's thesis the production of Tb radioisotopes for medical applications is investigated. The aim of this work is to optimise the production of neutron deficient Tb isotopes that are produced by proton induced spallation reactions of Ta targets. This thesis would not have been the same without the support of many people.

First, I would like to thank my promotor Prof. Cocolios for giving me the opportunity to make this thesis and to give me an insight on how it is like to be part of a research group. Furthermore, I would like to thank my supervisor Kristof for his guidance throughout the year. I am also grateful for Simon and Greg, it was nice to share an office with you. Wouter, thank you for solving so many of my computer related problems.

Daarnaast wil ik natuurlijk mijn ouders en mijn broer bedanken. Mama en papa, bedankt om mij de kans te geven om fysica te studeren en om mij altijd te steunen. Bedankt ook voor alle etentjes op zaterdagavond tijdens de weekends dat ik in Leuven bleef werken. Dat betekent veel voor mij. Graag bedank ik ook de rest van mijn familie, ze hebben mij allemaal geholpen op hun eigen manier.

Ik wil graag mijn vrienden van Van Gogh A bedanken. Mijn vijf jaar in Leuven zouden niet hetzelfde zijn geweest zonder jullie. Bedankt om altijd voor mij klaar te staan, om te luisteren naar mijn frustraties en om te zorgen voor de nodige ontspanning. Jullie zijn geweldig! Tot slot, Simon, wil ik jou bedanken. Zonder jouw motivatie was ik nooit zover geraakt, je geloofde altijd in mij en misschien het belangrijkste van al, je maakt me gelukkig. Bedankt!

Scientific summary

Tb has four different isotopes that are useful in the context of nuclear medicine, i.e. ^{149}Tb, ^{152}Tb, ^{155}Tb and ^{161}Tb. In nuclear medicine, radiopharmaceuticals are applied for the diagnostics and treatment of certain deceases. Their chemical equivalence means that Tb-labelled radiopharmaceuticals for diagnostics or therapy will have identical pharmacological properties. This is an important advantage for so-called theranostic applications, where therapy and diagnostics are combined to improve the results of the therapy.

^{161}Tb is efficiently produced by irradiating ^{160}Gd with thermal neutrons to form ^{161}Gd, which quickly decays into ^{161}Tb. For the neutron deficient isotopes mentioned above, i.e. ^{149}Tb, ^{152}Tb and ^{155}Tb, one of the most promising production methods is high-energy proton-induced spallation of Ta targets, coupled with isotope separation on-line or off-line. It is however unavoidable to collect isobaric contaminants. These include so-called pseudo-isobars, which are molecules with the same total mass, such as oxides or fluorides. An example is the presence of ^{139}Ce impurities in the collection of ^{155}Tb, as ^{139}Ce^{16}O. These contaminant often need to be chemically removed before the Tb isotopes can be used in nuclear medicine. Therefore, it is beneficial to optimise the production protocol such that these isobaric contaminants are minimised. This work describes two methods to achieve this. One way is to select the most appropriate proton energy for the production of the isotopes of interest, while minimising isobaric contaminants. Another way is to choose the target temperature to optimise the extraction purity of the isotope of interest.

To analyse the effect of the proton energy on the in-target production, Ta foils are irradiated with protons of an energy between 300 and 2500 MeV at the COoler SYnchrotron (COSY) in the Forschungszentrum Jülich in Germany. Subsequently, γ-ray energy spectra are analysed for some of these foils in order to calculate cumulative cross sections. Because of a decay time of at least a month between the irradiation of the foils and the measurement of the spectra, cumulative cross sections are only calculated for longer-lived isotopes. Some of these isotopes are present as a contaminant in the collection of Tb isotopes. This analysis shows that a lower proton energy reduces the number of nucleons evaporated in the spallation process. Therefore, for the collection of ^{155}Tb, protons with an energy below 800 MeV should be used to minimise the contamination with ^{139}Ce^{16}O. This work also presents the cumulative cross section data of ^{149}Tb that was obtained from an α-analysis, done by other people, of the same foils. The goal of this analysis is to solve the discrepancy between different data sets in literature. The results presented here, show that the values of Winsberg [1] and Miranov [2] are preferred.

Another way to minimise the collection of isobaric contaminants is by optimising the target temperature for the extraction. For this, the results of the first isotope delivery from CERN-MEDICIS are analysed. Here, ^{155}Tb is collected after it is produced by the irradiation of a Ta target with 1400 MeV protons. Different collections are executed, each with the target at a different temperature. The results show that temperatures below 2000 °C can be used to extract CeO, while a higher temperature is needed to extract Tb. Because this is the first isotope collection at the CERN-MEDICIS facility, it is a great opportunity to compare FLUKA simulations to estimate the ambient dose equivalent rates in the experimental hall with measurements. The results show that these kind of simulations can give a qualitative idea of the dose distribution and of the main contributions to the dose. However, quantitative results should be handled with care.

Vulgariserende samenvatting

Aan het einde van de 19e eeuw werd radioactiviteit ontdekt. Sindsdien wordt het gebruikt in verschillende toepassingen. In de geneeskunde worden radioactieve bronnen onder andere gebruikt in de nucleaire geneeskunde. Hier worden zogenaamde radiofarmaca gebruikt. Een radiofarmacon bestaat uit een radioactief isotoop dat verbonden wordt met een molecule dat zich naar een specifieke plaats in het lichaam zal begeven, bijvoorbeeld naar een tumor. Dit kan dan, afhankelijk van de soort isotoop, gebruikt worden om een beeld te vormen van het lichaam of voor de behandeling van bijvoorbeeld kanker door tumoren te doden.

In een vrij recente techniek, krijgt de patiënt eerst een radiofarmacon toegediend dat geschikt is voor beeldvorming. Later, na de analyse van de beelden, krijgt de patiënt een radiofarmacon dat speciaal ontwikkeld is voor de behandeling. Deze methode zorgt ervoor dat de behandeling specifiek afgestemd kan worden op de noden van de patiënt. Het is wel belangrijk dat het radiofarmacon dat gebruikt werd bij de beeldvorming chemisch exact hetzelfde is als dat voor de behandeling, zodat ze zich op dezelfde manier verplaatsen doorheen het lichaam. Dit is de reden waarom de terbium isotopen, waar deze thesis over gaat, zo interessant zijn. Het chemische element terbium heeft namelijk vier verschillende isotopen die gebruikt kunnen worden voor beeldvorming en/of voor behandeling in de nucleaire geneeskunde.

De terbium isotopen die nuttig zijn in nucleaire geneeskunde komen niet in de natuur voor, ze moeten dus geproduceerd worden. Een veel gebruikte methode om terbium isotopen te maken is protonen met een zeer hoge energie afvuren op een trefschijf gemaakt van tantaal. Bij de reacties die dan ontstaan, worden er zeer veel verschillende isotopen gemaakt, waaronder een aantal van de terbium isotopen. Vervolgens wordt de trefschijf sterk verhit, zodat de geproduceerde isotopen er gemakkelijker uitgehaald kunnen worden. Tot slot, worden de geproduceerde isotopen gescheiden op basis van hun massa, zodat enkel de gewenste isotopen verzameld kunnen worden. Er zijn echter vaak nog ongewenste isotopen met dezelfde massa aanwezig, zogenaamde isobare contaminanten. Omdat ze dezelfde massa hebben, worden ze immers ook verzameld. Deze moeten vaak nog op een andere manier verwijderd worden voordat men de gewenste isotopen kan gebruiken in de nucleaire geneeskunde.

In dit werk worden twee methodes onderzocht om de productie van terbium isotopen te optimaliseren. In een eerste methode wordt de energie van de protonen, die op de trefschijf afgevuurd worden, gevarieerd. Afhankelijk van de energie zullen bepaalde isotopen meer geproduceerd worden dan anderen. Uit de resultaten blijkt dat het voor bepaalde terbium isotopen beter is een lagere protonen energie te kiezen, omdat de contaminan-

ten voornamelijk bij een hogere energie geproduceerd worden. Bij een tweede methode wordt onderzocht hoe de temperatuur van de trefschijf invloed heeft op de extractie van verschillende elementen. Hier blijkt dat de belangrijkste contaminanten al bij een lagere temperatuur uit de trefschijf komen dan de gewenste isotopen. Het is daarom aangewezen om eerst de bij een lagere temperatuur zo veel mogelijk van de contaminanten uit de trefschijf te halen en om vervolgens naar een hogere temperatuur te gaan voor de verzameling van de gewenste isotopen.

List of abbreviations

A	atomic mass number
BR	Branching Ratio
CERN	Conseil Européen pour la Recherche Nucléaire
COSY	COoler SYnchrotron
CR	Count Rate
CT	Computed Tomography
DNA	DeoxyriboNucleic Acid
FWHM	Full Width at Half Maximum
HVL	Half Value Layer
ISOLDE	Isotope Separation OnLine DEvice
JULIC	JÜlich Light Ion Cyclotron
LET	Linear Energy Transfer
MEDICIS	MEDical Isotopes Collected from ISOLDE
MRI	Magnetic Resonance Imaging
N	neutron number
PET	Positron Emission Tomography
PSB	Proton-Synchrotron Booster
SPECT	Single Photon Emission Computed Tomography
Z	atomic number or proton number

Contents

1 Introduction **1**

2 Tb radioisotopes for medical applications **3**
2.1 Radioactive decay . . . 3
2.2 Interaction of radiation with matter . . . 6
2.2.1 Charged particles . . . 6
2.2.2 Uncharged particles . . . 9
2.3 Biological effects of ionising radiation . . . 13
2.4 Radiation protection . . . 14
2.5 Nuclear medicine . . . 17
2.5.1 Imaging . . . 17
2.5.2 Therapy . . . 19
2.5.3 Theranostics . . . 19
2.5.4 Tb isotopes . . . 20

3 Production of neutron deficient Tb isotopes **21**
3.1 Isotope separation on-line and off-line . . . 21
3.2 Spallation . . . 22
3.3 Cumulative cross section . . . 25
3.4 FLUKA . . . 26

4 Cumulative cross section measurement **27**
4.1 Experimental setup . . . 27
4.1.1 Irradiation of the foils . . . 27
4.1.2 Measuring γ-ray energy spectra . . . 28
4.2 Methods . . . 30
4.2.1 Detector characterisation . . . 30
4.2.2 Analysis of the spectra . . . 34
4.2.3 Cumulative cross section . . . 34
4.3 Results & Discussion . . . 36
4.3.1 Detector characterisation . . . 36
4.3.2 Analysis of the spectra . . . 41
4.3.3 Cumulative cross section . . . 44

5 First isotope collection at CERN-MEDICIS **51**
5.1 The CERN-MEDICIS facility . . . 51
5.2 First isotope collection . . . 52

5.2.1 Temperature dependence of the collection 52
5.2.2 Ambient dose equivalent 52
5.3 Results & Discussion 55
5.3.1 Temperature dependence of the collection 55
5.3.2 Ambient dose equivalent 56

6 Conclusions & Outlook **67**

Appendices **69**

A Background spectrum **70**

B Example spectrum **71**

C Cumulative cross sections **73**

Bibliography **78**

1 | Introduction

Already shortly after the discovery of radioactivity, it became apparent that radioactive isotopes could be applied in medicine. The branch of medicine that uses radioactive isotopes for the diagnostics and therapy of certain diseases is called nuclear medicine. One of the first times radioactive isotopes were applied in nuclear medicine was in 1946 when S. Seidlin reported the successful treatment of a patient with thyroid cancer with ^{131}I [3]. Since then, many different isotopes have been produced, isolated and applied, not only for the treatment of diseases, but also for their diagnostics.

In the context of nuclear medicine, Tb is a very special element because is has four different isotopes that are applicable for therapeutic and/or diagnostic purposes. These isotopes are ^{149}Tb, ^{152}Tb, ^{155}Tb and ^{161}Tb [4]. Due to their chemical similarity, radiopharmaceuticals for therapy and diagnostics can be made with exactly the same pharmacological properties (e.g. uptake, targeting, biodistribution). Therefore, the Tb isotopes are very interesting for theranostics, where therapy and diagnostics are combined to improve the effects of the treatment. This is explained in more detail in Chapt. 2.

Before the Tb isotopes can be routinely applied in a medical setting, their production and delivery first need to be reliable. In Chapt. 3, the main production methods of these isotopes are explained. However, the focus is on the production of the neutron deficient isotopes i.e. ^{149}Tb, ^{152}Tb and ^{155}Tb. More specifically, this work concentrates on the production of the neutron deficient Tb isotopes by spallation reactions that result from the irradiation of Ta targets with protons. After the production, the isotopes are extracted from the target and subsequently separated based on their mass-to-charge ratio. Finally, the selected isotopes are collected, such that they can be used in specific applications. Since the produced isotopes are separated based on their mass-to-charge ratio, it is inevitable to also collect isobaric contaminants, which often have to be removed chemically. Therefore, Chapt. 4 and 5 investigate two possible methods to minimise these isobaric contaminants.

As a first method, in Chapt. 4 an experiment is described to study the proton beam energy impact on the production probability for different longer-lived isotopes. Therefore, thin Ta foils are irradiated with protons of an energy between 300 and 2500 MeV at the COoler SYnchrotron (COSY) in the Forschungszentrum Jülich (Germany). Gamma-ray energy spectra are analysed for these foils in order to calculate cumulative cross sections at different proton energies. Longer lived isotopes are selected by letting the foils decay for one to two and a half months before γ-ray energy spectra are measured. In this chapter also some simulations are performed to cross check the results of the calculations.

For the extraction of the produced isotopes from the target, the material is heated to enhance the diffusion and evaporation. Depending on this temperature, some isotopes will be extracted more than others. In Chapt. 5, this is investigated by looking at the results from the first isotope collection from CERN-MEDICIS. Here, three batches of ^{155}Tb are collected after a Ta target has been irradiated with 1400 MeV protons. For each collection, the target is at a different temperature. Analysing the collected samples allows investigating the temperature dependence of the collection. At the same time, this experiment allows to check the reliability of simulations that are performed to calculate the radiation dose for people working near the collection point. For this, simulations are compared with actual data from radiation monitors in the experimental hall.

2 | Tb radioisotopes for medical applications

Tb offers four radioisotopes that are interesting for applications in nuclear medicine, i.e. ^{149}Tb, ^{152}Tb, ^{155}Tb and ^{161}Tb [4]. By giving an introduction on radioactive decay and how different types of ionising radiation interact with matter, this chapter describes the biological effects of ionising radiation. Related to this, this chapter provides some fundamental aspects of radiation protection and finally also of nuclear medicine.

2.1 Radioactive decay

Some unstable nuclei can emit particles to lose energy; this is called radioactive decay. Radioactive decay is a stochastic process, it is impossible to predict when exactly a nucleus will decay. However, one can calculate the probability that it will decay in a time interval dt. This probability is equal to λdt, where λ $[s^{-1}]$ is the decay constant, which is isotope dependent. When N radioactive nuclei are present at some time t_0, one can expect $dN = -N\lambda dt$ nuclei to decay in the time interval dt. This leads to the radioactive decay law [5]:

$$-\frac{dN}{dt} = \lambda N \equiv A. \tag{2.1}$$

Here, N is the number of radioactive nuclei and A is the activity. The SI unit of activity is becquerel (Bq), where one becquerel is defined as one disintegration per second. Related to the decay rate, one can define the half-life ($t_{1/2}$) as the time it takes to reduce the initial number of radioactive nuclei to half of its value.

$$t_{1/2} = \frac{\ln 2}{\lambda} \tag{2.2}$$

The energy of the emitted radiation is usually expressed in electron volt (eV) instead of joule (J). One electron volt is defined as the kinetic energy an electron gains when it is accelerated by a potential difference of 1 volt [6].

$$1\ eV \approx 1.602 \times 10^{-19} J \tag{2.3}$$

There are different types of radioactive decay, two of the most relevant ones being α- and β-decay. In the first type, α-decay, a nucleus emits a ^{4}He nucleus, which is also called an

α-particle, according to the following reaction:

$$^{A}_{N}X \rightarrow ^{A-4}_{N-2}Y + \alpha \tag{2.4}$$

The α-particles emitted by a specific isotope are monoenergetic with an energy typically between 4 and 6 MeV [6].
Another type of radioactive decay is β-decay. An electron (β^--particle) or a positron (β^+-particle) is emitted by a nucleus with a neutron or proton excess, respectively. In β^--decay a neutron (n) is transformed into a proton (p) with the emission of an electron (e^-) and an electron antineutrino ($\overline{\nu}_e$):

$$n \rightarrow p + e^- + \overline{\nu}_e. \tag{2.5}$$

β^+-decay is similar to β^--decay, only now a proton (p) is converted into a neutron (n) with the emission of a positron (e^+) and an electron neutrino (ν_e):

$$p \rightarrow n + e^+ + \nu_e. \tag{2.6}$$

The excess energy of the reaction is spread over the two emitted particles, the β-particle and the neutrino, and the recoiling nucleus. Therefore, the energy of the β-particles ranges from zero to the endpoint energy, which is equal to the total decay energy. All isotopes that can decay via β^+-decay can also decay via a competing process called electron capture, in which an orbital electron is captured by a proton [6]:

$$p + e^- \rightarrow n + \nu_e. \tag{2.7}$$

Radioactive decay often leaves the daughter nucleus in an excited state, after which it rapidly decays to the ground state by emitting one or more photons, called γ-rays. The excited states in the daughter nucleus typically have very short lifetimes, such that γ-decay is generally much faster than the foregoing decay. Therefore, the γ-rays will be emitted with the half-life of the parent nucleus and the energy of the γ-rays will provide information about the level structure of the daughter nucleus [6].
In competition with γ-decay, nuclei in an excited state can decay to the ground state by transferring energy to an orbital electron, which is then emitted. This process is called internal conversion. The energy of this conversion electron is smaller than that of the related γ-ray by the binding energy of the electron [6].

Some of the above processes i.e. electron capture and internal conversion, can create a vacancy in an electron shell or can leave the atom in an excited state. The electrons will quickly rearrange themselves to return the atom to its ground state. An electron in an outer shell fills a vacancy in an inner shell. In this process, a characteristic X-ray photon can be emitted to release the excess energy. In a competitive process, the excess energy is released by the emission of an orbital electron called an Auger electron. These processes themselves result in an electron vacancy, which is again filled by an electron from an outer shell. This thus results in a cascade of characteristic X-rays or Auger electrons [6]. In Figure 2.1 an example of both processes is shown.

Some isotopes have different decay modes, each with their own probability. The branching ratio (BR) is defined as the fraction of particles that decays via a specific decay mode with respect to the total number of decaying particles [8]. As an example, Figure 2.2 shows a simplified version of the decay scheme of ^{149}Tb, which decays by α-decay to ^{145}Eu and by β^+-decay or electron capture to ^{149}Gd. For each decay mode the type of decay and the branching ratio is shown.

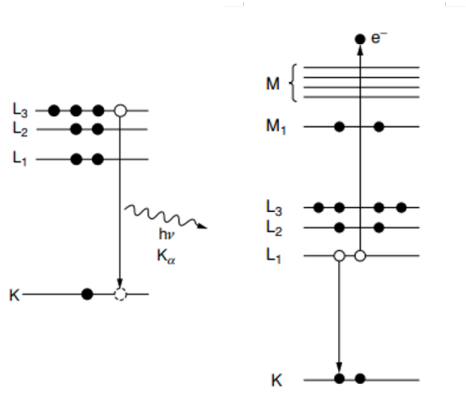

Figure 2.1: (a) Characteristic X-ray and (b) Auger electron that can result from an initial vacancy in the K electron shell [7].

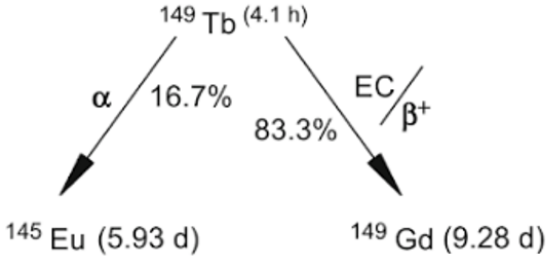

Figure 2.2: Simplified decay scheme of ^{149}Tb (adapted from [9]).

2.2 Interaction of radiation with matter

The way in which radiation interacts with matter forms the basis for the working principle of radiation detectors and for the biological effects of ionising radiation. The latter is important for radiation protection and the medical applications of ionising radiation. The interaction of radiation with matter depends on the energy and type of the radiation. Moreover, it is also dependent on the material with which the radiation interacts. In what follows, the interaction of charged and uncharged particles with matter will be discussed separately, because the way they interact with matter differs.

2.2.1 Charged particles

Charged particles such as protons, α-particles, heavy ions, electrons and positrons, mainly interact with orbital electrons through the Coulomb force. Besides that, interactions with the nuclei in the material are also possible. However, these events are rare at the energy range of interest to this work, so they will not play a significant role here. Through the continuous interaction with the orbital electrons, energy is transferred to these electrons. The transferred energy can be large enough to promote an electron to a higher lying shell, i.e. to excite the atom. Larger energy transfer results in ionisation of the atoms in the medium. This leads to the formation of ion pairs along the track of the charged particle. These are pairs of charged particles where one is positively charged and the other is negatively charged, usually a single charged ion and an electron. Sometimes the transferred energy is large enough such that the electrons themselves have enough kinetic energy to cause ionisation. These electrons are called δ-rays. Because the transfer of energy is small in each interaction, the charged particles continuously lose kinetic energy until the particles are completely stopped in the medium. This decrease in energy is described by the linear stopping power, S [eV/nm], which is defined as the differential energy loss of the particles, divided by the differential path length in the material [6]:

$$S \equiv -\frac{dE}{dx} \tag{2.8}$$

In what follows heavy charged particles such as protons, α-particles and heavy ions, will be discussed separately from β-particles. The reason behind this is twofold. The first reason is that the path followed by heavy charged particles is more straight compared to the much lighter β-particles that have the same mass as the orbital electrons with which they interact. Furthermore, due to their smaller mass, radiative processes can no longer be neglected for β-particles, as will be explained later.

Heavy charged particles

For heavy charged particles the linear stopping power is given by the Bethe formula [6]:

$$S \equiv -\frac{dE}{dx} \propto \frac{z^2}{v^2} NZ \tag{2.9}$$

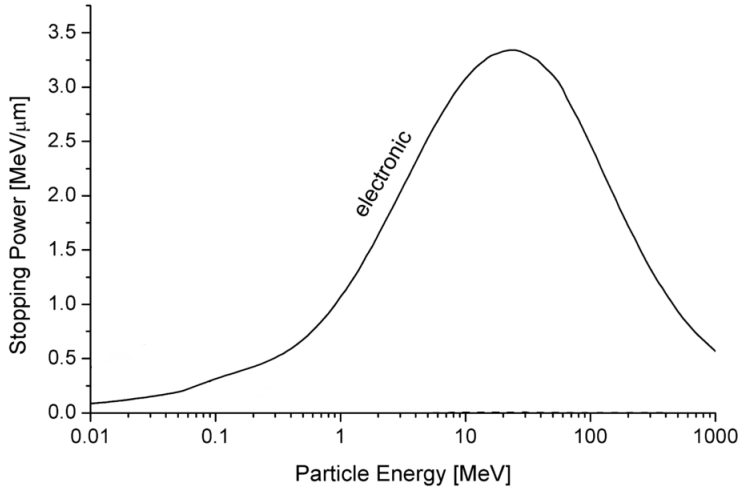

Figure 2.3: The linear stopping power as a function of the particle energy per nucleon for aluminium ions in aluminium (adapted from [10]).

In this equation, z is the charge of the particle expressed in units of elementary charge, v [m/s] is its velocity, N [-] is the number density of the matter and Z is the atomic number of the matter. From equation (2.9), one can see that the linear stopping power is proportional to $1/v^2$. Therefore, the linear stopping power is inversely proportional to the energy of the particle. One can explain this dependence as follows. If the energy of the charged particle is smaller, the particles spends more time in the vicinity of an orbital electron, such that more energy can be transferred. Besides the energy of the particle, also its charge will contribute to the linear stopping power. The linear stopping power is proportional to the charge of the particle squared, such that particles with a larger charge encounter a much larger linear stopping power. The linear stopping power also depends on the material with which the charged particle interacts. From equation (2.9) it is apparent that the linear stopping power increases for larger $N \cdot Z$, which corresponds to the electron density in the medium. Although, it was stated before that S increases with decreasing energy, the linear stopping power actually starts to decrease again for very low energies. The reason for this is that at low energies the particles start to pick up electrons from the absorber. This reduces the charge of the particles and thus reduces the energy loss. Figure 2.3 shows how the linear stopping power varies with the energy of the ion. When a particle enters the medium, first the energy loss increases as the particle penetrates further into the medium, decreasing its velocity. When the energy is low enough, it starts to bind electrons. This rapidly reduces the energy loss and results in a peak at the end of the particle's track, called the Bragg peak. Figure 2.4 shows the energy loss as a function of distance both for a single heavy charged particle as for a beam of heavy charged particles with the same initial energy. The Bragg peak is broadened for the beam of particles due to an effect called energy straggling. Although all particles in the beam have the same initial energy, their path lengths will not be exactly the same due to slight variations in the details of the interactions. We call this energy straggling [6].

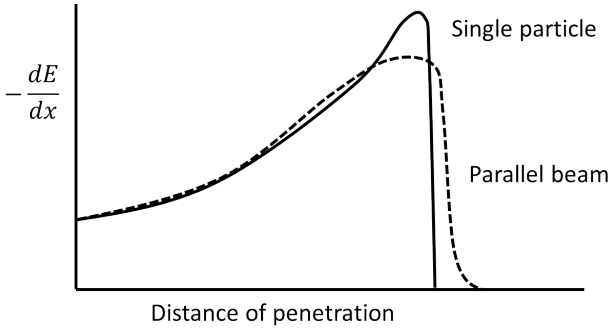

Figure 2.4: The energy a particle loses along its track as a function of the penetration distance both for a single heavy charged particle (solid line) and for a parallel beam of heavy charged particles (dashed line). At the end of the track, the Bragg peak is visible. The peak is broadened for a parallel beam due to energy straggling (adapted from [6]).

Related to the linear stopping power is the range of charged particles, which is the distance the particle travels in a medium before it is stopped. The range, R [nm], of a particles can be expressed as [7]:

$$R = \int_{E_0}^{0} \frac{dx}{dE} dE, \tag{2.10}$$

where E_0 [eV] is the initial energy of the particle. This equation actually describes the path length of the particle, which is equal to the particle range if the trajectory of the particle is straight. For heavy charged particles this approximation is valid because the mass of the particles is much larger than the mass of the orbital electrons they interact with. For example the mass of the proton is 1836 times larger than the electron mass [7]. Therefore, the particles are almost not deflected from their straight path and the range is very well approximated by equation (2.10). The range of 4 MeV α-particles in tissue is for example about 25 μm [11].

β-particles

Electrons and positrons are different from heavy charged particles in the sense that they can lose energy by radiative processes as well as by collisional processes, i.e. excitation and ionisation. The linear stopping power can then be written as a sum of collisional and radiative losses [6]:

$$S \equiv -\left(\frac{dE}{dx}\right)_c - \left(\frac{dE}{dx}\right)_r. \tag{2.11}$$

Similar to equation (2.9) an expression can be derived for the energy loss of electrons or positrons by collisional losses:

$$-\left(\frac{dE}{dx}\right)_c \propto \frac{NZ}{v^2} \tag{2.12}$$

where the charge, z, is 1 for electrons. For light charged particles such as β-particles, energy loss by radiative processes can no longer be neglected. When charged particles are accelerated (or decelerated), they will lose energy by the emission of electromagnetic

radiation called Bremsstrahlung. The energy loss through radiative losses can be expressed in the following way:

$$-\left(\frac{dE}{dx}\right)_r \propto NEZ^2 \tag{2.13}$$

This shows that radiative losses will become more important for high-energy particles and for materials with high density and high atomic number.
Because the mass of β-particles is equal to that of the orbital electrons, there will be large deviations in the path of these particles. Therefore, equation (2.10) overestimates the range of β-particles. For 4 MeV β-particles, the range in tissue is about 2 cm [11].

Electrons and positrons are very similar in the way they lose energy in a material, such that their ranges will be comparable for equal initial energies. There is however one striking difference between electrons and positrons in their interaction with matter. At the end of their track, positrons combine with electrons in the material in a process called electron-positron annihilation. The annihilation energy is emitted as two oppositely directed photons with an energy of 511 keV each, which is equal to the rest mass of the electron and positron [5].

2.2.2 Uncharged particles

Photons and neutrons are both uncharged particles; as a result, they will not interact continuously with matter through the Coulomb interaction. Instead, uncharged particles will undergo a limited number of interactions with full or partial energy transfer from the incident photon or neutron to electrons or nuclei in the material, respectively. As a result, secondary charged particles are produced, namely, fast electrons or heavy charged particles. These charged particles on their turn will cause excitations and ionizations of atoms in the medium. The interaction of uncharged particles with matter is a stochastic process. This means that there is always a probability that the particles pass through a medium without interaction [6].

Photons

There are multiple possible interaction mechanisms between high-energy photon, e.g. γ-rays, and matter [12]. In what follows, the most important ones will be discussed: photoelectric effect, Compton scattering and pair production. In these processes, the energy of the photon is completely or partially transferred to an electron. This electron in its turn will deposit all or part of its energy in the material. Also worth mentioning is Rayleigh scattering, however, no energy is deposited by this process.

In the photoelectric effect, a photon is completely absorbed when it interacts with an atom. As a result, an electron, usually from an inner shell, is ejected. This high-energy electron is called a photoelectron. The energy of the photon needs to be high enough to overcome the binding energy of the orbital electron. Therefore, the energy of the photoelectron will be equal to $E_{e^-} = E_\gamma - E_b$, where E_γ is the energy of the photon and E_b is the binding energy of the electron. Subsequently, the electron will continuously interact with the surrounding material, depositing its energy. The atom is now left with

a vacancy in one of its shells. The other electrons quickly rearrange themselves. The difference in energy level is then released as X-ray photons or as Auger electrons. The probability per unit of length, τ [m^{-1}], for a photon to interact through the photoelectric effect is approximately [6]:

$$\tau \propto \frac{Z^n}{E_\gamma^{3.5}}, \tag{2.14}$$

where Z is the atomic number of the interacting atoms and n ranges between 4 and 5 over the energy region of interest. From this expression, it is clear that the photoelectric effect becomes more important for low energy γ-rays and X-rays and that its probability increases for materials with high atomic number. Because the energy of the photon is completely absorbed by the materials when it interacts through the photoelectric effect, this is the preferred interaction for the detection of photons. This is under the assumption that the photoelectron, the Auger electrons and the characteristic X-rays are completely stopped.

Another way photons can interact with matter is by Compton scattering. In this process, a photon is deflected from its original direction by a collision with an electron from an outer shell, which is considered to be a free electron. Part of the energy of the photon is transferred to the electron, which is called the recoil electron. Applying conservation of energy and momentum, one can write an expression relating the energy of the scattered photon to the angle θ over which it is scattered [6]:

$$E'_\gamma = \frac{E_\gamma}{1 + \frac{E_\gamma}{m_0 c^2}(1 - \cos\theta)}, \tag{2.15}$$

where m_0c^2 is the rest-mass energy of the electron. Note from this formula that always part of the energy is kept by the photon even in the case $\theta = \pi$, where the energy transfer to the electron is maximal. For small scattering angles, very little energy is transferred to the electron. The probability per unit of length, σ [m^{-1}], that a photon interacts through Compton scattering increases linearly with Z and varies slowly with the photon energy as can be seen in Figure 2.5, which shows the energy dependence of the different interaction types of photons:

$$\sigma \propto Z. \tag{2.16}$$

For high energy γ-rays, with an energy that is larger than twice the electron rest-mass energy ($E_\gamma > 1022$ keV), it is possible to interact via pair production. In this interaction, that can only take place near an atomic nucleus, a photon is converted into an electron-positron pair. Afterwards, the electron and the positron are slowed down in the medium after which the positron annihilates with an electron and two 511 keV γ-rays are emitted. The probability per unit of length, κ [m^{-1}], for a photon to interact via pair production increases approximately with the square of the atomic number of the interacting material:

$$\kappa \propto Z^2. \tag{2.17}$$

κ also sharply increases with increasing photon energy and it is zero for energies below 1022 keV, this can be seen in Figure 2.5.

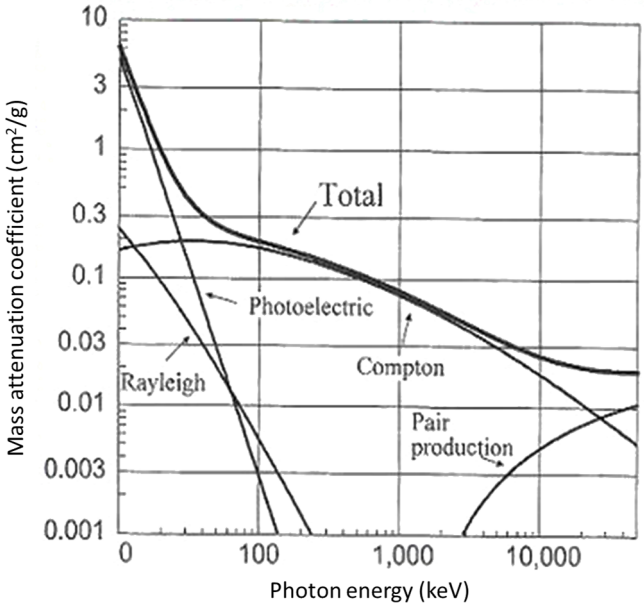

Figure 2.5: Energy dependence of the different interactions of photons for the interaction with soft tissue (adapted from [11]).

Another, but less important, interaction mechanism between photons and matter is Rayleigh scattering. The difference with Compton scattering is that Rayleigh scattering can be regarded as a collision of a photon with an entire atom, rather than a single electron. Due to the large mass difference between the photon and the atom, the photon only loses a negligible amount of energy. However, the direction in which the photon travels will be changed in the process.

Figure 2.6 shows which of the above interactions is dominant as a function of the photon energy ($h\nu$) and the atomic number (Z) of the medium. The photoelectric effect is most important for low energy photons and in materials with a high atomic number. In materials with a low atomic number, Compton scattering will be the main interaction type. Finally, for high-energy photons, pair production will be dominant.

For uncharged particles it is impossible to define the range of the particles in the same way as was done in equation (2.10). This is due to the stochastic nature of the interactions; it is never certain whether a photon will interact with the material or not. All that is known is the probability that a photon will interact per unit length, this is the linear attenuation coefficient, μ [m^{-1}], which is equal to the sum of the probabilities of all possible interaction mechanisms explained above. So the linear attenuation coefficient is given by [6]:

$$\mu = \tau + \sigma + \kappa, \tag{2.18}$$

which will depend on the photon energy and on the material through which the photon travels. The number of photons transmitted through a piece of material will decrease if the thickness increases. The fraction of photons that is eliminated over a distance dx is:

$$\frac{dN}{dx} = -\mu N. \tag{2.19}$$

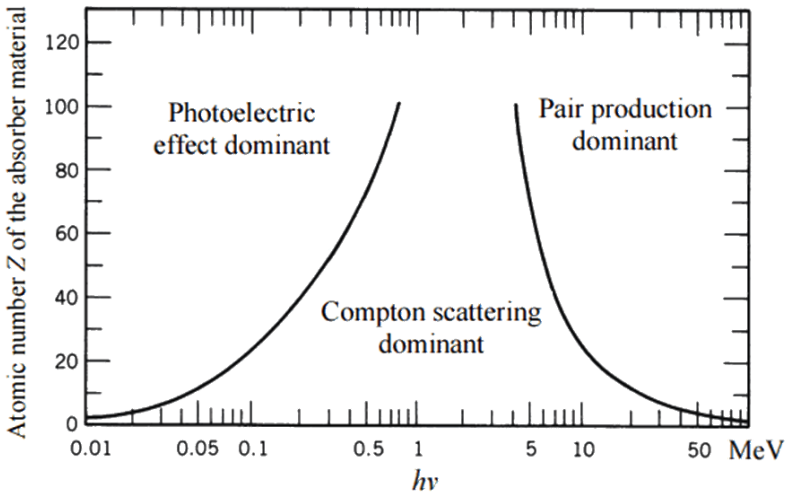

Figure 2.6: Dominant interaction type for photons as a function of the photon energy ($h\nu$) and the atomic number of the absorber material (adapted from [6]).

This expression is very similar to equation (2.1) and in an analogous way as was done in equation (2.2) for the half-life, the half value layer, HVL [m], can be defined:

$$HVL = \frac{\ln 2}{\mu}. \tag{2.20}$$

The half value layer is defined as the thickness of a certain material that is needed to reduce the number of photons by a factor 2. In tissue, the half value layer of 140 keV photons is about 44 mm [11].

Neutrons

The secondary particles resulting from interactions with neutrons are usually heavy charged particles instead of electrons as it was the case for photons. These heavy charged particles can be a product of neutron induced nuclear reactions or they can be the nuclei in the material that have gained energy by collisions with neutrons. To describe the interaction of neutrons with matter a distinction is made between slow and fast neutrons, because their properties are quite different. The pivot point between slow and fast neutrons is usually taken at about 0.5 eV [6].

Slow neutrons mainly interact through elastic scattering with nuclei in the material and through neutron-induced nuclear reactions. In elastic scattering, very little energy is transferred to the nuclei, due to the small energy of slow neutrons. However, since these reactions have a large probability to occur, elastic scattering can effectively slow down the neutrons. Furthermore, slow neutrons can interact through neutron-induced nuclear reactions, where the neutron is captured by a nucleus, which induces a nuclear reaction. These reactions can result in the emission of a photon, α-particle, proton or fission fragments.

For fast neutrons, neutron induced nuclear reactions are not important since the probability for these reactions to occur drops rapidly with increasing energy. Scattering with

nuclei becomes more important at high energies. The fast neutrons can transfer enough energy to the nuclei to transform them into secondary charged particles. If the energy of the fast neutrons is high enough, the scattering reactions can leave the nucleus in an excited state that quickly releases its energy by emitting a γ-ray.

2.3 Biological effects of ionising radiation

As biological tissue is composed of matter, ionising radiation will also interact with it. When ionising radiation interacts with biological tissue, it causes damaging effects. To get an understanding of the effect of radiation, one has to look at the effects of the interaction with radiation on a sub-cellular or molecular level. The reason for this is that radiation damage to tissue or organs is always a result of damage to individual cells in the tissue, which in its turn results from damage to the constituents of the cell. As discussed before, when ionising radiation travels through material, it will transfer energy to the material along its track. This transfer of energy can break chemical bonds and, consequently, alter or even destroy the function of a molecule. On a sub-cellular level, DNA is the most important molecule to take into account. The reason for this is that DNA contains all the information needed for the functioning, development and reproduction of the cell, such that DNA mainly determines the survival of the cell. Furthermore, due to its large size, DNA is more prone to the damaging effects of radiation compared to other constituents of the cell, because the probability of interaction is larger [13].

Ionising radiation can cause damage to the DNA in two different ways: through direct and indirect action [14]. In direct action, the ionising radiation directly interacts with the DNA molecule and as a result damages it. However, since most of the body consist of water, ionising radiation will mainly interact with water molecules. This results in the formation of highly reactive free radicals, which contain one unpaired electron. These hydrogen (H$\cdot$) and hydroxyl radicals (HO$\cdot$) can on their turn interact with the DNA molecule to cause damage; this is called indirect action. The difference between direct and indirect action is shown in Figure 2.7.

Damage to DNA occurs mostly in the form of a single or double strand break, which is a break in one or both of the strands of the DNA double helix. These breaks can be caused by both direct and indirect action. Luckily, the cells have repair mechanisms that can repair these types of damage. However, these repair mechanisms are not perfect and breaks are sometimes repaired incorrectly or not repaired at all. Since double strand breaks are the most complex to repair, this type of damage is the most severe. When a break in the DNA strand is not (correctly) repaired, there are three possible outcomes [14].
Firstly, it is possible that the radiation damage has no negative effect on the cell and the cell will still be able to function as before.
Secondly, the damage can be so severe that the cell kills itself in a process called apoptosis. If this happens to many cells in the same organ, the organ can lose its functionality, specifically in the case of germ cells, it can result in sterility. These are the so-called deterministic effects. Deterministic effects only occur when a certain minimum dose is exceeded and once this happens, the severity of the effect will increase with increasing dose.

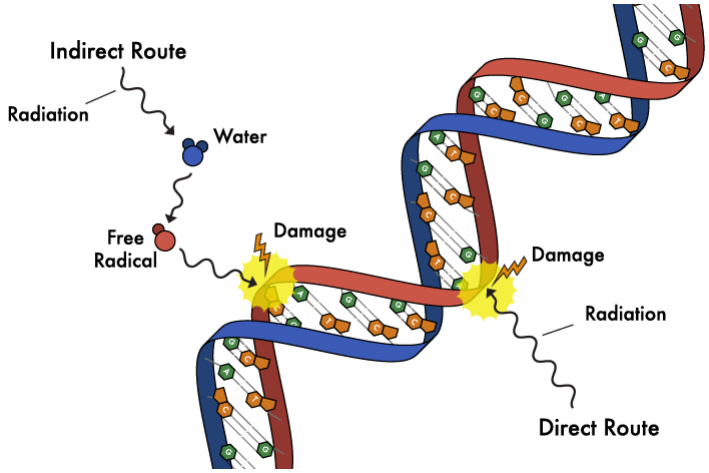

Figure 2.7: Illustration of the structure of DNA and the difference between direct and indirect action of ionising radiation [15].

Finally, incorrectly repaired DNA can result in a cell that is still able to survive, but that has an altered functionality. These mutations can lead to cancer or to genetic defects in the case of germ cells. These effects have a stochastic origin. Contrary to deterministic effects, for stochastic effects, it is assumed that there is no threshold dose below which no effects occur. Consequently, mutations can occur at any received dose. For stochastic effects, occurrence cannot be predicted, however, the probability of occurrence increases with increasing dose. Due to this uncertainty, stochastic effects are not unambiguously related to ionising radiation.
In the context of radiation protection, stochastic effects will be the most important, because they will already occur for very low doses. Contrarily, therapeutic medical applications will rely on deterministic effects. Figure 2.8 shows the dose-effect curves for stochastic and deterministic effects. It shows both the occurrence frequency and the severity of the effects of ionising radiation as a function of the received dose. It can be seen that the frequency of occurrence of deterministic effects is not a step function as expected. The reason for this is that each person has a slightly different response, which causes the curve to be slightly spread out. The causes of the differences in individual susceptibilities are among a large number of things: age, gender and genetics [14].

2.4 Radiation protection

As explained in the previous chapter, ionising radiation can cause damage to biological tissue. Therefore, it is important to protect people from the harmful effects of exposure to ionising radiation. In order to assess the biological effects of ionising radiation, radiation protection dose quantities have been developed.
The basic quantity for radiation protection is the absorbed dose, D. This is a purely physical quantity and is defined as the average amount of energy that is absorbed per unit of mass.

$$D = \frac{d\bar{\varepsilon}}{dm} \tag{2.21}$$

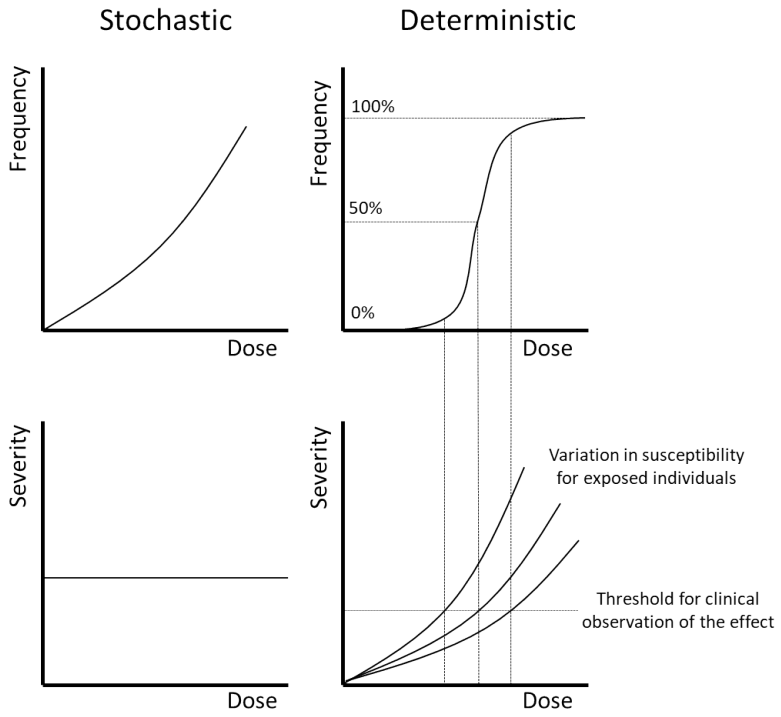

Figure 2.8: Frequency of occurrence and severity of the effects of ionising radiation as a function of dose for stochastic and deterministic effects (adapted from [16]).

The absorbed dose is defined as a point quantity, however, in the context of radiation protection it is usually used as the average value over an organ [11]. The unit of absorbed dose is gray (Gy), where 1 Gy is equal to 1 J/kg [17].

The biological effects of radiation are not directly related to the amount of energy that is absorbed; also the type of radiation and which organ it interacts with is important. Therefore, protection dose quantities are created. The first protection dose quantity is the equivalent dose, H, which includes the effect of the type of radiation. Different types of radiation can be more harmful than others depending on their linear energy transfer (LET), which is the energy loss per unit of path length. The LET is approximately equal to the stopping power for charged particles. If the LET is higher, more chemical bonds can be broken per unit of path length. Therefore, the probability for double strand breaks in the DNA increases. These are harder to repair than single strand breaks. As a result, high LET radiation, such as α-particles and neutrons, is more harmful for the same absorbed dose than low LET radiation, such as photons and electrons. The equivalent dose considers this by including a radiation weighting factor, w_R. The equivalent dose for a certain organ (T) is defined as:

$$H_T = \sum_R w_R \cdot D_{R,T} \tag{2.22}$$

where a sum is made over the different types of radiation and $D_{R,T}$ is the average absorbed dose in a specific organ (T) due to a specific type of radiation (R). The radiation weighting factors, w_R, are shown in Table 2.1. For neutrons, the interaction with matter strongly

Table 2.1: Radiation weighting factors for different types of radiation [18].

radiation	w_R
photons, electrons and muons	1
neutrons	see Figure 2.9
protons >2 MeV	2
α-particles and heavy ions	20

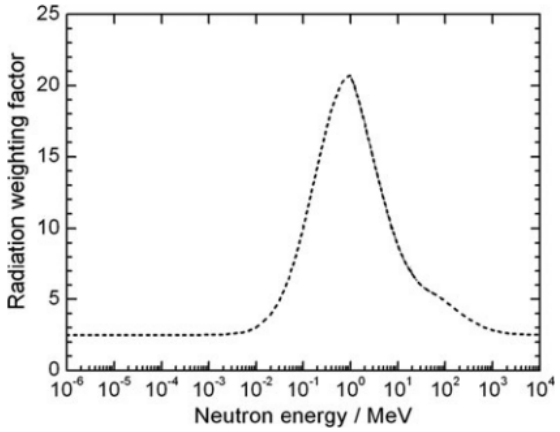

Figure 2.9: The energy dependence of the radiation weighting factor for neutrons [18].

depends on the energy. Accordingly, the radiation weighting factor is energy dependent for neutrons, as shown in Figure 2.9. The unit of absorbed dose is sievert (Sv), which has the same physical dimensions as the absorbed dose, because the radiation weighting factors are dimensionless.
Some organs are more sensitive to ionising radiation than others are. To take this into account the effective dose, E, is defined. This protection quantity includes tissue weighting factors, w_T as follows:

$$E = \sum_T w_T \sum_R w_R D_{R,T} \tag{2.23}$$

The tissue weighting factors for different organs are shown in Table 2.2. The unit for the effective dose is also sievert (Sv) [17].

The protection dose quantities, equivalent dose and effective dose, are directly related to the biological effects of the exposure to ionising radiation; however, they cannot be measured. Therefore, operational dose quantities are defined in such a way that they provide an estimate for the protection dose quantities. For individual monitoring the personal

Table 2.2: Tissue weighting factors for different organs [18].

Organ/tissue	w_T
Bone marrow, colon, lung, stomach, breast, remainder	0.12
Gonads	0.08
Bladder, liver, oesophagus, thyroid	0.04
Bone surface, skin, brain, salivary glands	0.01

dose equivalent, $H_p(d)$, is used as operational quantity. It is the dose equivalent in standard soft tissue at a depth d below a specific point on the human body. To estimate the effective dose, the personal dose equivalent at a depth of 10 mm, $H_p(10)$, is frequently used.
For area monitoring, the ambient dose equivalent, $H^*(10)$, is the used operational dose quantity. The ambient dose equivalent is defined as the dose equivalent at a point in a radiation field that would result from a corresponding expanded and aligned field in a 30 cm diameter sphere of tissue of unit density at a depth of 10 mm on the radius vector opposite to the direction of the aligned field. An expanded aligned field is a uniform, unidirectional field that corresponds to the actual field at the specified point. Radiation monitors for radiation protection, such as dosimeters and environmental radiation monitors are often calibrated in terms of operational dose quantities [17].

2.5 Nuclear medicine

In nuclear medicine, one takes advantage of the way ionising radiation interacts with matter and especially with biological tissue for the diagnosis and treatment of certain diseases. For this purpose, nuclear medicine makes use of radiopharmaceuticals. These consist of a radioactive isotope that is linked to a molecule with specific biological affinity or it can be a radioisotope that itself has biological affinity. A radiopharmaceutical is delivered to the patient and will follow a specific metabolic pathway in the body or will bind to a specific type of cells. For example, cancer cells overexpress certain receptors on their surface, which are hardly present in other cells. The radiopharmaceuticals can be designed in such a way that they specifically bind to this receptor to target the cancer cells [19]. The radiopharmaceutical carries a radioisotope and depending on the type of radionuclide it carries, it can be used for imaging or therapy [5].

2.5.1 Imaging

When the radionuclide emits γ-rays it is possible to follow the radiopharmaceutical in its travel through the body by detecting the emitted γ-rays. Due to its large HVL, a significant amount of γ-rays is still detectable outside the body. The radiopharmaceutical gets involved is some metabolic process, such that nuclear medicine measures function, whereas other techniques e.g. CT, MRI, measure anatomy. Since often metabolic changes happen much sooner than anatomic changes, abnormal tracer distributions can be an early indication for certain diseases [20]. The γ-rays can either be directly emitted by the radionuclide or originate from the annihilation of an emitted positron with an electron in the matter. In the first case the imaging technique is called Single Photon Emission Computed Tomography (SPECT) and in the second case it is called Positron Emission Tomography (PET).

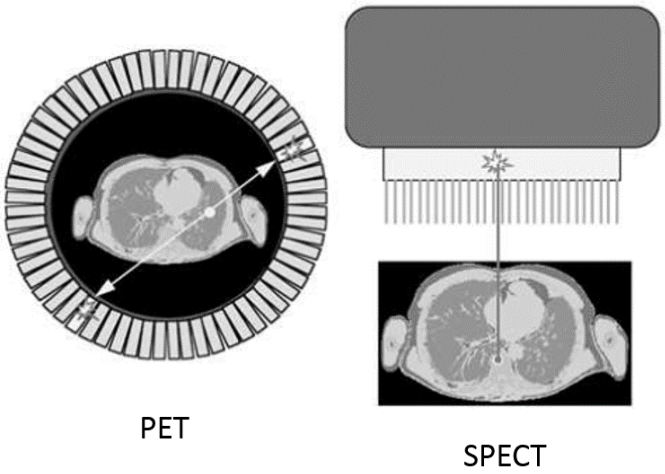

Figure 2.10: Illustration of the PET and SPECT process. In PET the patient is surrounded by a ring of detectors and in SPECT a mechanical collimator is used [5].

SPECT

With SPECT an image of the spatial distribution of the radiopharmaceutical can be made by detecting the γ-rays emitted by the radioactive isotope. To make an image, one needs a lens and a detector. Unfortunately no lenses exists that can focus high-energy photons such as γ-rays. Therefore, a more primitive method needs to be used namely collimation. A mechanical collimator is essentially a sieve that blocks all photons that are not directed perpendicular to the detector surface. It is typically made out of a high-Z material that strongly attenuates γ-rays, such as lead, and consists of long narrow holes through which the photons can pass. Since the collimator blocks most of the photons, the detector needs to have a high sensitivity. Furthermore, because the photoelectric effect is the preferred interaction mechanism for detection, the detector needs to have a high atomic number, as seen in Figure 2.6. Therefore, usually inorganic scintillation detectors are used. By making multiple planar images along different directions, it is possible to compute a complete 3D drawing of the distribution of the radiopharmaceutical [5].

PET

The annihilation radiation, that results from the interaction of a positron with an electron from the surrounding medium, can be used to image the distribution of a radiopharmaceutical carrying a β^+-emitter. When a positron annihilates, two 511 MeV γ-rays are emitted in opposite directions. These photons can be detected outside the body by a ring of detectors. By detecting two photons in coincidence, it is possible to recreate a 3D image of the tracer distribution. This is called Positron Emission Tomography or PET. Since the two photons are always directed along the same line, no extra collimation is necessary. Similar to SPECT, mostly inorganic scintillation detectors are used for PET. Figure 2.10 shows a schematic image of the PET and SPECT process.

In order to be useful as a radionuclide in a radiopharmaceutical for imaging, an isotope should meet some requirements. First of all, ideally, the energy of the emitted photons should be between 30 and 300 keV for SPECT [21]. If the energy is too small, not enough photons will penetrate through the tissue and if the energy is too large, detection and collimation become more difficult. For PET the energy of the γ-rays is of course fixed at 511 keV. However, for PET the energy of the positron is important: this should be as small as possible. This is because higher energy positrons travel a longer distance before annihilation and, therefore, reduce the resolution of the PET image [5]. Besides the energy of the decay, also the half-life is important. Ideally, the half-life should be about 1.5 times the examination time [21]. This largely depends on how fast the radiopharmaceutical travels to its destination, the so-called biodistribution. For example, antibodies are rather large molecules, which move rather slowly. Therefore, a radioisotope with a longer half-life should be used. As another requirement, radioisotopes for SPECT and PET should ideally not emit additional α- or β^--particles. Those increase the radiation dose for the patient, without additional diagnostic value [4].

2.5.2 Therapy

In contrast to γ-rays, α- and β-particles deposit all their energy in a very short range. Accordingly, they can cause a lot of damage to a very small region. This property is exploited in radionuclide therapy where a radiopharmaceutical carries an α- or β-emitter. The radiopharmaceutical is a complex molecule that is designed to specifically bind to a certain target, such as a tumour. Radionuclide therapy has a few advantages compared to other cancer therapies. Every tumour cell in the body is systematically targeted, which is not possible with other treatments like surgery and radiation therapy. Moreover, it mostly affects the malignant cells, which is not the case in chemotherapy, where also healthy cells in the body are exposed to the drug [20].

For radioisotopes in therapeutic radiopharmaceuticals, also some requirements should be met. First, the range of the emitted radiation should match with the size of the area that is targeted. Typically, β-emitters are used for larger tumours and α-emitters for smaller ones [20]. Again, the half-life should match with the biodistribution of the radiopharmaceutical. Finally, in the ideal case, the daughter of the radioisotope is stable, such that it does not give an unnecessary extra dose. This is often a problem for α-emitters, where there is an additional problem that the daughter nucleus can be released from the radiopharmaceutical due to its recoil [21].

2.5.3 Theranostics

Imaging and therapy can be combined. This is called theranostics (therapy + diagnostics) and is useful in for example cancer treatments. The goal is to optimise the therapy based on the information obtained from a specific diagnostic test. In theranostics, the radiopharmaceutical is first labelled with an isotope suitable for SPECT or PET. In this way, the image will demonstrate whether or not the cancer cells are present, where they

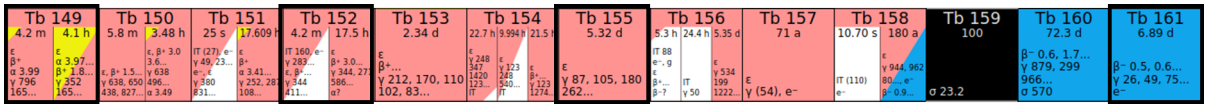

Figure 2.11: Part of the Tb isotopic chain [23].

are located and whether the half-life and biodistribution are well matched. Subsequently, the radiopharmaceutical can be labelled with a therapeutic radionuclide to kill the cancer cells. By combining the two, not only can it be decided whether radionuclide therapy is appropriate for the patient, but also an estimate of the required and delivered doses can be made in advance. It is important that diagnostic and therapeutic radiopharmaceuticals have similar chemical properties, such that their pharmacokinetics and pharmacodynamics are identical [4]. Ideally, the radioisotopes used for diagnostics and therapy are of the same element. Sometimes one isotope can be used for treatment and imaging at the same time. An example of such isotope is ^{177}Lu, which emits β-particles and γ-rays [21]. This can for example be useful to evaluate the effect of a previous treatment. One can also use two different isotopes of the same element, where one is useful for imaging and the other for treatment, these are called matched pairs [19].

2.5.4 Tb isotopes

Terbium is one of the few elements that has not just two, but four isotopes that are interesting for applications in the context of nuclear medicine. ^{149}Tb, ^{152}Tb, ^{155}Tb and ^{161}Tb form a matched quadruplet [4]. Since these radionuclides are all chemically identical, tracer molecules can be made for both imaging and therapy with exactly the same pharmacological characteristics. ^{149}Tb emits short range α-particles with an energy of 3.967 MeV and a branching ratio of 17 %, it has a half-life of 4.16 hours. This terbium isotope can be used for radionuclide therapy. Moreover, it also emits β^+-particles that can be used for PET [22]. ^{152}Tb is a positron emitter that emits positrons of an average energy of 1.080 MeV with a branching ratio of 17 %, it has a half-life of 17.5 hours. Therefore, it is suitable for imaging using PET. ^{155}Tb decays by electron capture and has a half-life of 5.32 days. It emits γ-rays of 86.55 keV and 105.3 keV with a branching ratio of 32 % and 25 % respectively, such that it can be applied for SPECT. The last terbium isotope of interest is ^{161}Tb. It is a β^--emitter that emits low energy electrons with an average energy of 154 keV with a branching ratio of 100 %. Additionally, it emits Auger electrons and γ-rays with an energy of 48.92 keV (17 %), 57.19 keV (1.8 %) and 74.57 keV (10 %). Therefore, this radionuclide can be used for β^-- and Auger therapy and for SPECT [4]. Figure 2.11 shows a part of the Tb isotopic chain with these four isotopes.

3 | Production of neutron deficient Tb isotopes

To be useful for medical applications, the interesting Tb isotopes first need to be produced and delivered reliably. The neutron rich isotope in the quadruplet, ^{161}Tb, can be produced by irradiating highly enriched ^{160}Gd targets with neutrons in a nuclear reactor to form ^{161}Gd through a (n,γ)-reaction. ^{161}Gd has a short half-life ($t_{1/2}$ = 3.66 min [24]) and will decay quite fast by β^--decay to form ^{161}Tb [25]. Such production is already possible at research reactors such as the Belgian Reactor 2 (BR2) of the SCK•CEN in Mol, or at the Institut Laue-Langevin (ILL) in Grenoble (France). For the neutron deficient isotopes, ^{149}Tb, ^{152}Tb and ^{155}Tb, two main production methods are currently being investigated in parallel [4]. First, similar to ^{161}Tb, the proton rich Tb isotopes can be produced by the irradiation of enriched Gd targets, this time with protons instead of neutrons [26]. The following nuclear reactions are suitable to produce these isotopes: ^{152}Gd(p,4n)^{149}Tb*, ^{152}Gd(p,n)^{152}Tb and ^{155}Gd(p,n)^{155}Tb. This gives an efficient method for the production of ^{155}Tb, because of the high enrichment grade of commercially available ^{155}Gd (>99 %). However, for ^{149}Tb and ^{152}Tb the disadvantage is that, due to the low enrichment grade of commercially available ^{152}Gd (∼30 %), plenty Tb impurities will be present [4]. This work will focus on a second production method for the neutron deficient Tb isotopes, namely proton-induced spallation of tantalum (Ta) targets. In what follows this method will be explained in detail.

3.1 Isotope separation on-line and off-line

For the production of Tb isotopes by proton-induced spallation reactions, the isotope separation on-line and off-line methods are used. These methods involve different stages: production, extraction, ionisation, separation and collection [27]. The difference between the on-line and the off-line isotope separation is that in the off-line method the production is separated from the rest of the stages, while in the on-line method they directly follow each other.

The first stage is the production, where a beam of neutrons, electrons or light or heavy ions interacts with a target [27]. This results in the production of many different nuclei through various reactions e.g. fission, spallation and fragmentation [28]. The neutron deficient Tb isotopes are produced by spallation reactions when high-energy protons hit a Ta target. This process is explained in detail in the next section.

After the production, isotopes are extracted from the target material. First, the produced nuclei diffuse through the target and after that, they effuse out of the target. The efficiency of these processes depends on the physical and chemical properties of both the target material and the produced atoms. To improve this step, the target is heated to high temperatures of about 2000 °C [28].
In the following stage, the produced atoms are ionised. In general, single charged ions are produced [27]. The three main ionisation mechanism are surface ionisation, electron impact ionisation and resonant laser ionisation. Surface ionisation is based on the ionisation of atoms when they interact with a hot surface. It works best for atoms with a low ionisation potential such as alkali and alkaline earth metals or for atoms with a large electron affinity such as halogens [28]. In electron impact ionisation, the atoms lose one or more electrons due to the bombardment with electrons [27]. This is a more universal process i.e. it can be used to ionizer many different atoms [28]. This is both an advantage and a disadvantage as it typically results in poor chemical selectivity of the overall process. Resonant laser ionisation uses multiple lasers, typically two or three, to excite the atoms stepwise, until they are ionised. This process can select specific elements, because the energy levels of the electrons are element specific [27].
After the ionisation, the ions are accelerated by an electric field to the separator. The separation is done by a dipole magnet, which bends the ions trajectory into a circular path with a radius that depends on their mass-to-charge ratio. The resolving power of a typical dipole magnet is good enough to select ions with a given mass number A, but not to separate different isobars. Therefore, when a contaminant with the same A is ionised, it will also pass through the separator. This is often the case, even with resonant laser ionisation, because atoms can still be ionised by surface ionisation [28]. These isobaric contaminants can also be present as pseudo-isobars. These are molecules, for example monoxide ions, that have the same total mass [29].
Once the ions are separated, they can be collected. This is done by implanting them in e.g. thin metal foils [30]. After the collection, further purification is possible with chemical methods such as cation exchange chromatography [29].

It is clear that it is beneficial to minimise the collection of isobaric contaminants. Accordingly, this work looks at two different methods to optimise the production protocols to produce the neutron deficient Tb isotopes. First, in Chapt. 4, the dependence on the energy of the incoming proton of the production probability is investigated for longer-lived contaminants. Subsequently, in Chapt. 5, the influence of the target temperature on the dominant isotope present in the collection is studied.

3.2 Spallation

The neutron deficient Tb isotopes can be produced by proton-induced spallation of Ta targets. Before explaining spallation reactions, it is important to mention that two different definitions are used in literature. First, spallation is used as collective name for the three reactions that can result from the interaction between high-energy light projectiles and heavy targets: high-energy fission, fragmentation and evaporation. Besides that, spallation is also used as the name for one of these high-energy nuclear reactions. High-energy nuclear reactions consist of fission, fragmentation and spallation, where spallation can be

seen as a synonym for evaporation. This last definition is the one adopted here.
This work is about proton-induced spallation of Ta targets, so the light projectile will be protons and the heavy target will be Ta.

As explained before, when high-energy protons, with an energy higher than approximately 500 MeV, hit a target, three kinds of reactions can occur: fission, spallation and fragmentation [27]. In high-energy fission reactions, the nuclei that are hit by the protons are divided into two or more roughly equal parts. In spallation, nucleons or light nuclei are emitted from the target nucleus and in fragmentation, an excited nucleus breaks-up in a very fast reaction. The products of these high-energy reactions are spread over many mass numbers [31] and N-over-Z ratios [32].

High-energy nuclear reactions can be described as a two stage process [31]. The first stage is called the intra-nuclear cascade. At high energies (>500 MeV), the De Broglie wavelength of the incoming protons is smaller than the inter-nucleon distance in the nucleus, which is of the order of 1 fm. Therefore, the interaction can be described as a collision between free nucleons [32]. In this process, high-energy protons, neutrons and pions are created inside the nucleus, with an energy higher than 20 MeV [33]. Some of these high-energy particles are rapidly emitted, mainly in the direction of the incident particle, this is called pre-equilibrium emission. Others stay in the nucleus and spread their energy such that they leave the target nucleus in an excited state [32].
In the second stage, the de-excitation stage, the excited nucleus, also called pre-fragment, dissipates its energy. This can happen by evaporation of low energy (<20 MeV) particles, such as neutrons and light charged particles, e.g. protons and α-particles: this is called spallation. In contrast to the pre-equilibrium emission, these particles are emitted isotropically. Furthermore, the excited nucleus can de-excite by the emission of γ-rays. In addition, these de-excitation processes are in competition with fission [33]. In another process, fragmentation, nuclei are split off from the excited nucleus in a rapid break-up that happens before energy equilibrium is reached throughout the nucleus [31]. Figure 3.1 gives a schematic overview of a high-energy nuclear reaction. Fragmentation is not shown in this image.

High-energy nuclear reactions produce nucleons and small clusters of nucleons and result in the production of residual nuclei. These residual nuclei can typically be divided into three groups, as can be seen in Figure 3.2 for proton induced reactions with U. The first group of nuclei have a high mass, close to that of the target nuclei. These nuclei are a result of the spallation process. The evaporation of neutrons is governed by the binding energy. For protons it is governed by the binding energy and the Coulomb barrier. Therefore, neutrons are more easily released than protons. For this reason, the residual nuclei are often neutron deficient. A second group of residual nuclei is located in the intermediate mass region. These nuclei are produced by fission of the pre-fragments. For stability, higher mass nuclei need a neutron excess. The fission process typically maintains the N-over-Z ratio of the pre-fragment. Therefore, the neutron excess of the higher mass target nuclei is often preserved, such that the residual nuclei tend to be neutron rich. Finally at low masses a third group of nuclei can be found, they are emitted in the fragmentation process [32].

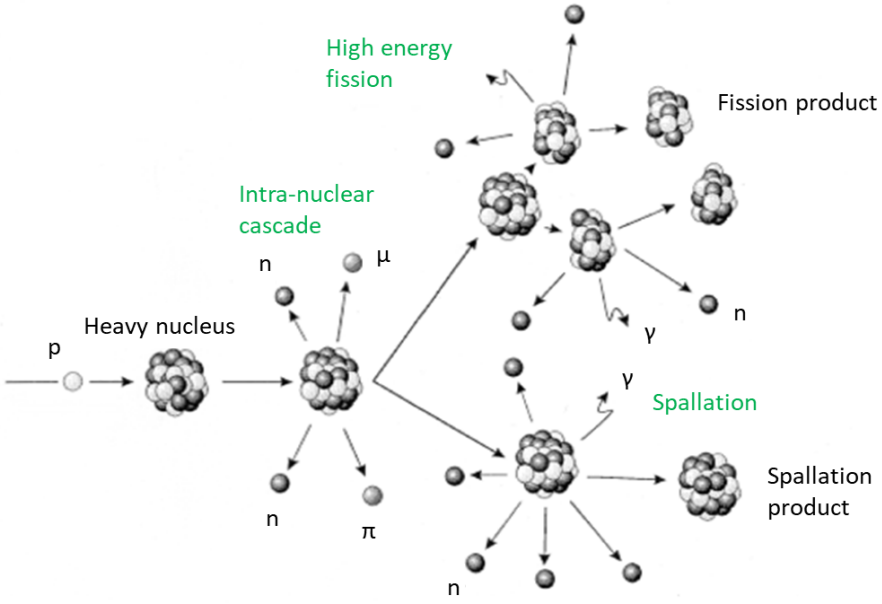

Figure 3.1: Schematic overview of a high-energy nuclear reaction, with high-energy fission and spallation. Fragmentation is not shown (adapted from [34]).

In this work, the interest will be on proton-induced spallation of Ta targets. Due to its lower mass than that of U, for Ta no fission will occur, because the energy released in the reaction is too small to cross the fission barrier. Therefore, only spallation and fragmentation products will be formed.

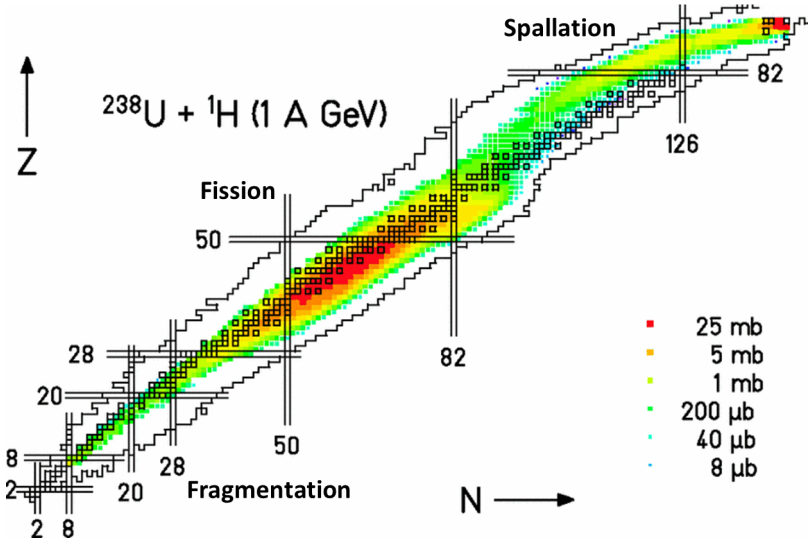

Figure 3.2: Residual nuclei produced by the irradiation of ^{238}U with 1 GeV protons (adapted from [35]).

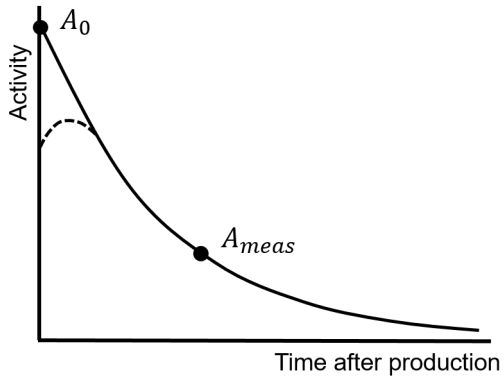

Figure 3.3: Activity of a longer-lived isotope as a function of the time after the production. Shorter-lived isotopes will decay into this longer-lived isotope (dotted line).

3.3 Cumulative cross section

A large part of this work will be devoted to the measurement of cumulative cross sections for some long-lived isotopes that are produced by proton-induced spallation of Ta. The cumulative cross section of a certain isotope is the production cross section for that isotope, which includes the decay of shorter-lived isotopes into that isotope. Figure 3.3 shows the activity of a certain isotope as a function of the time after its production. The dashed line is the curve that is followed in reality. A certain activity of that isotope is created, but also shorter-lived isotopes will be produced at the same time. These shorter-lived isotopes will decay into the longer-lived isotopes until they have completely decayed. From this moment, the solid line is followed. For the calculation of cumulative cross sections, one assumes that the shorter-lived isotopes never existed, such that A_0 represents the assumed activity after production for pure, direct isotope production. This means that for cumulative cross sections, the solid line in Figure 3.3 is followed completely. A_0 can then be calculated from the measured activity, A_{meas}, by solving equation (2.1), assuming that at the time of the measurement all short-lived isotopes have decayed.
The concept of cumulative cross section is useful in the context of the collection of radioisotopes for applications. When working with an off-line separation method, the produced isotopes will have the chance to decay in the target before they are separated. The cumulative cross section will therefore be a measure for the amount that will be collected. Also for on-line separation, cumulative cross section is a useful concept. Most radioisotopes that are produced by the proton-induced spallation of Ta will be β-emitters and therefore their daughters will be on the same isobar. As an example, Figure 3.4 shows a part of the β-decay chain of A=155. As explained before, during collection all isotopes of a specific isobar will be selected. This means that in the collected sample decay will happen towards the isotopes closer to stability, so with longer half-lives. The activity that is eventually left of such a longer-lived isotope after a few hours consist not only of the direct production of that isotope, but also of the decay of shorter-lived isotopes. For example, ^{155}Tb can be produced by extracting its precursor ^{155}Dy after the irradiation of a Ta target with protons. A cooling time of a few days is enough to make sure most of the ^{155}Dy has decayed to ^{155}Tb [29].

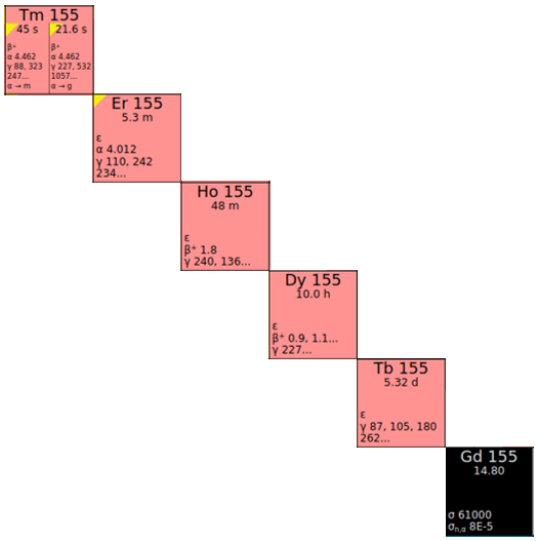

Figure 3.4: Part of the β-decay chain of A=155 [23].

3.4 FLUKA

In this work different types of simulations are performed. These simulations are all done with FLUKA, a multi-particle transport code [36, 37]. FLUKA is a Monte Carlo simulation package that is able to simulate the transport and interaction of particles and nuclei in matter with complex geometries. It can be used for various applications such as dosimetry, target design, calorimetry, shielding design, etc.
In FLUKA, one starts with an initial amount of particles, called primaries, defined by the user. The transport and interaction of these particles is then handled stepwise. The possible interactions between the particle and the material are randomly sampled with each step, depending on their probability. An important feature of FLUKA is that microscopic models are selected as much as possible. Moreover, at each step conservation laws are enforced and results are checked against experimental data [37]. When the particle stops, the code starts with a new particle until all initial particles are simulated. Then, detectors can be defined that can measure physical quantities such as activity and fluence. With the first set of simulations, an estimation is made of the activity of different isotopes that are produced by proton-induced spallation reactions in Ta foils. These simulations are explained in more detail in the next chapter. In Chapt. 5, simulations are performed to estimate the ambient dose equivalent that results from the collection of radioisotopes for the first collection at CERN-MEDICIS. For this, FLUKA estimates the particle fluence after which fluence to ambient dose equivalent conversion factors are used to determine the ambient dose equivalent [38]. These simulations can then be compared to experimentally obtained results.

4 | Cumulative cross section measurement

The cross section for the production of isotopes by proton-induced spallation is energy dependent, such that the in-source production of isotopes will depend on the energy of the protons. By selecting the correct proton energy, it is possible to maximise the production of the isotope of interest, while minimising isobaric contaminations. To investigate this, Ta foils are irradiated with protons of different energies at the COoler SYnchrotron (COSY) at FZ Jülich. In this work, γ-ray energy spectra of these foils are analysed for the calculation of cumulative cross sections. The spectra are measured after a decay time of one up to two and a half months, to look for isotopes with long half-lives.

4.1 Experimental setup

4.1.1 Irradiation of the foils

The Ta foils are irradiated with protons provided by the synchrotron COSY at the Institute for Nuclear Physics at FZ Jülich. To produce protons, first H^--ions are made in an ion source, after which a high voltage of about 4000 V is used to extract them from the plasma. These ions are then accelerated from 4 keV to 45 MeV in the JÜlich Light Ion Cyclotron (JULIC). Subsequently, the H^--ions are send through a thin carbon foil, before they are transported to COSY. This carbon foil strips off the electrons, so that protons

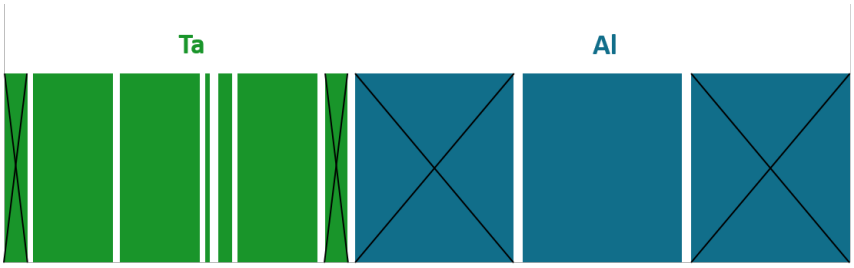

Figure 4.1: Schematic drawing of the experimental setup used for the irradiation of the Ta foils with protons. The proton beam is incident on the left side. The foils have different sizes ranging from 2 μm to 50 μm. The foils covered with a cross were discarded (see text for details).

will circulate in COSY. Here, the protons are accelerated to their experimentally required energy. If needed, the protons can then be cooled to improve the beam quality [39].
Protons with an energy between 300 and 2500 MeV are send onto a stack of Ta and Al foils with irradiation times of about two to three hours. The stack is as follows: seven Ta foils with thicknesses of 10, 25, 25, 2, 6, 25, 10 μm, followed by three Al foils with each a thickness of 50 μm. All foils have a diameter of 1 cm. A schematic drawing of the setup is shown in Figure 4.1. The Al foils are used to determine very precisely the proton current used during the experiment. This is possible because the cross sections for the proton-induced reactions in Al are very well known. For each material, the first and the last foil is not used because, due to recoil, some atoms may be lost or gained in these foils. This would result in wrong cumulative cross sections. For the other foils, it is assumed that the amount of atoms that enter the foil is the same as the amount of atoms that leave the foil.
In this work γ-ray energy spectra are analysed for nine foils: the 2 μm foil irradiated with 300 MeV protons and the 6 μm foils irradiated with protons with an energy of 300, 500, 600, 700, 900, 1100, 1300 and 1700 MeV. The spectra are measured between one and two and a half months after the irradiations. Therefore, shorter-lived nuclei, with a half-life shorter than a few days, will have completely decayed before the spectra are measured. Accordingly, ^{149}Tb, ^{152}Tb and ^{155}Tb will probably not be detected here. However, this method allows looking at longer-lived nuclei that can be present as contamination during the collection of the Tb isotopes.
This analysis is part of a larger collaboration. Besides γ-analysis with long decay times, an α-analysis is performed and a γ-analysis of spectra that are measured shortly after the irradiation. These combined give a more complete picture of the energy dependence of the production of isotopes by proton-induced spallation of Ta targets. The main goal of this experiment is to solve the discrepancy between different literature values for the cumulative cross sections for the production of ^{149}Tb and ^{152}Tb by proton-induced spallation of Ta [19].
To check the results obtained in the analysis of the γ-ray energy spectra, FLUKA simulations of the irradiations are performed. To reduce the computing time, instead of the complete stack, only one foil is used here. The activity of the different isotopes produced by the proton-induced reactions is simulated, so that it can be compared to the measured activity. For these simulations, the same irradiation time and decay time as the actual measurements is used. The proton current for the simulations is however only an estimate, because the analysis of the Al foils was not finished when the simulations were started.

4.1.2 Measuring γ-ray energy spectra

After the irradiation of the Ta foils with protons, γ-ray energy spectra are measured for some of the foils. For each of the selected foils, γ-rays are measured for multiple days. The spectra are measured with a Ge detector that is placed inside a lead shielding. A schematic drawing of the set-up is shown in Figure 4.2. A Ge detector is chosen, since this detector type has a very good energy resolution, which is needed considering the many different isotopes that are expected to be present in the foils. In order to reduce the background, the Ge detector is placed inside a lead shielding. This is necessary because the activity of the foils is expected to be low [6].

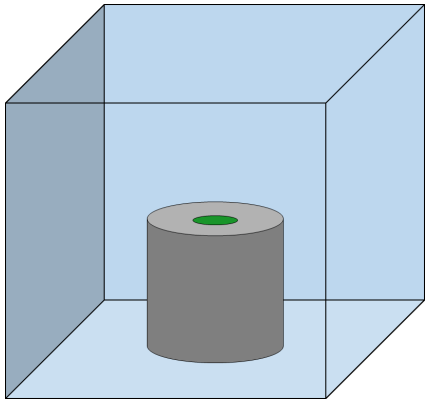

Figure 4.2: Schematic drawing of the experimental setup used to measure the γ-ray energy spectra. The Ge detector (grey) is shown with the Ta foil (green) on top of it, inside the lead shielding (blue).

Ge detectors are a type of semiconductor detectors. For semiconductors, the band gap between the valence band and the conduction band is small, of the order of one eV. When ionising radiation interacts with the semiconductor crystal, electrons will be promoted from the occupied valance band to the empty conduction band, thus creating an electron-hole pair. The number of electron-hole pairs that is generated is in general proportional to the energy of the radiation and is independent of the type of radiation. By applying an electric field to the crystal, the electrons and the holes will move to opposite ends of the semiconductor, where their charges can be collected. In order to collect the charges and hence to measure the energy of the γ-ray, an electrical contact is needed. The two ends of a p-n junction are the most suitable type of contacts for semiconductor detectors. A p-n junction is the interface between an n-type semiconductor and a p-type semiconductor. Although both types of semiconductors are neutral, a p-type semiconductor contains loosely bound holes and in an n-type semiconductor loosely bound electrons are present. In a p-n junction, holes will diffuse from the p-region to the n-region and electrons will diffuse from the n-region to the p-region. This results in a net negative charge in the n-region and a net positive charge in the p-region and thus the generation of an electric field that will eventually stop the diffusion of charge carriers. At the interface, a depletion region is created that has a very low concentration of free holes and electrons. This depletion region is useful as radiation detection medium, because electrons and holes that are created by the ionising radiation are removed from the depletion region by the electric field, such that they can be collected. The electric field that is generated in a p-n junction is too weak to make the charge carriers move fast through the detector and as a result, some of the charges can be trapped in crystal impurities. Moreover, the thickness of the depletion layer is quite small. For this reason an external potential is applied such that the junction becomes reverse biased. This means that the voltage is applied in such a way that the holes are pulled away from the p-region and electrons are pulled away from the n-region; this will thus increase the width of the depletion region [6].

For the detection of γ-rays, Ge detectors are often used. The first reason for this is that Ge has a quite high atomic number for a semiconductor (Z = 32). Therefore, the probability of interacting through the photoelectric effect is larger than that of for example Si (Z = 14), which is another typically used semiconductor for radiation detectors. Accord-

ingly, the detection efficiency for detecting γ-rays is larger for Ge than for Si. However, other detector types, namely scintillator detectors, have a much better detection efficiency than semiconductor detectors. The reason for this is that they have much higher atomic numbers. For example, I in NaI scintillator detectors has an atomic number of 53.
Another advantage of Ge is that very pure crystals can be produced. This is beneficial for the size of the depletion region, which ideally is as large as possible. The thickness of the depletion region d [m] is approximated by this formula.

$$d \cong \sqrt{\frac{2\epsilon V}{eN}} \tag{4.1}$$

Where ϵ [C/V·m] is the dielectric constant, V [V] is the reverse bias voltage, N [m^{-3}] is the impurity concentration and e [C] is the electronic charge. The voltage that can be applied to the semiconductor will be limited, because at some point a breakdown will occur. Therefore, the only way to further increase the size of the depletion region is by reducing the number of impurities.
The most important advantage of Ge detectors is their good energy resolution. Ge has a small band gap of about 0.7 eV. As a result, the energy needed to create one information carrier (in this case an electron-hole pair) is only a few eV. This is much smaller than the energy needed to produce an ion pair in a gas ionisation detector ($\sim$ 30 eV) or to produce a photoelectron in a scintillator detector ($\sim$ 100 eV). Accordingly, much more information carriers are created for the same energy for Ge detectors. For this reason, Ge detectors have a much better energy resolution than these other detector types, due to the higher statistics.
The small band gap also has a disadvantage. Because the energy to create an electron-hole pair is so small, thermal energy can produce electron-hole pairs. To reduce this effect the detectors are cooled, often to liquid nitrogen temperatures (-196 °C).
Another disadvantage of Ge detectors is that the time resolution of these detectors is not very good. This is because even with high reverse bias voltage, the time required for a charge carrier to travel 1 cm is about 100 ns. Moreover, the velocity is often different for holes and electrons. Therefore, the time it takes for the complete collection of the charges also depends on the position in the detector, which makes the time resolution even worse [6].

4.2 Methods

4.2.1 Detector characterisation

To obtain information from the measured γ-ray energy spectra, the detector first has to be characterised. Therefore, the energy calibration of the detector is conducted, a background spectrum is acquired and the detection efficiency is determined.

During the detection process, the energy of the measured photon is converted into a voltage. This voltage is then converted into a channel number by the multichannel analyser. To know the energy of a γ-ray of an unknown source, each channel number needs to be linked to a specific photon energy; this is called the energy calibration. For the energy

calibration, the spectrum of a well-known source is measured; here ^{152}Eu is used. The peaks in this spectrum are fitted with a Gaussian fit using a χ^2 fitting procedure. The channel numbers of the different peaks are then compared to the literature value [40] to obtain the energy calibration. Afterwards, the relation between the channel number and the energy is fitted using a χ^2 fitting procedure with either a linear or a quadratic curve.

Subsequently, a background spectrum is acquired. Eventhough measurements are done inside a lead shielding, still some background γ-rays will be present. It is important to subtract any background peaks from the peaks in the spectra. In principle this can be done by subtracting the complete background spectrum from the normal spectrum, of course normalised to the measurement time, and then analyse this resulting spectrum. However, here it is chosen to compare the individual peaks in the normal spectra and the background spectrum, because this procedure gives a better estimate of the uncertainty on the count rates. This is done by fitting the peaks in both spectra with Gaussian curves, from which the energy and the count rate of the peaks can be deduced. Then, the results are compared and for the peaks for which there is also a peak in the background spectrum, the count rates are subtracted.

In order to convert the measured count rate into activity, it is important to know the detection efficiency of the detector. Not every γ-ray emitted by a source will be detected by the detector. First, this is due to geometrical effects that are virtually independent of the photon energy. The radiation emitted by a source will be isotropically distributed in space, but the detector only covers a part of this. The solid angle of a detector Ω is a measure for the part of space that is covered by the detector and is defined by the following equation [6]:

$$\Omega = \int_A \frac{cos\alpha}{r^2} dA, \tag{4.2}$$

where r is the distance from the source to the surface element dA and α is the angle between the direction of the source and the normal of the surface element. Note that the solid angle of the complete space is equal to 4π. For a cylindrical detector, as is used here, with a point source placed along the axis of the cylinder, equation (4.2) becomes [6]:

$$\Omega = 2\pi \left(1 - \frac{d}{\sqrt{d^2 + a^2}}\right), \tag{4.3}$$

with a the radius of the detector crystal and d the distance from the source to the circular surface of the detector.
Besides the geometrical efficiency, also the intrinsic efficiency of the detector will contribute. Not all photons that are incident on the detector will be completely stopped in the crystal and thus fully measured. The intrinsic efficiency of the detector is equal to the number of counts in the full energy peak divided by the number of photons that are incident on the detector. This will be energy dependent for a given detector. Low energy photons have a higher probability to be stopped by the detector casing, resulting in a lower efficiency. For high energy photons the probability for interaction through the photoelectric effect becomes smaller (see Figure 2.6), which also results in a lower efficiency.

To determine the detector efficiency as a function of photon energy for the measurements of the Ta foils, two sources of known activity are measured. Here a 30.2(9) kBq ^{152}Eu

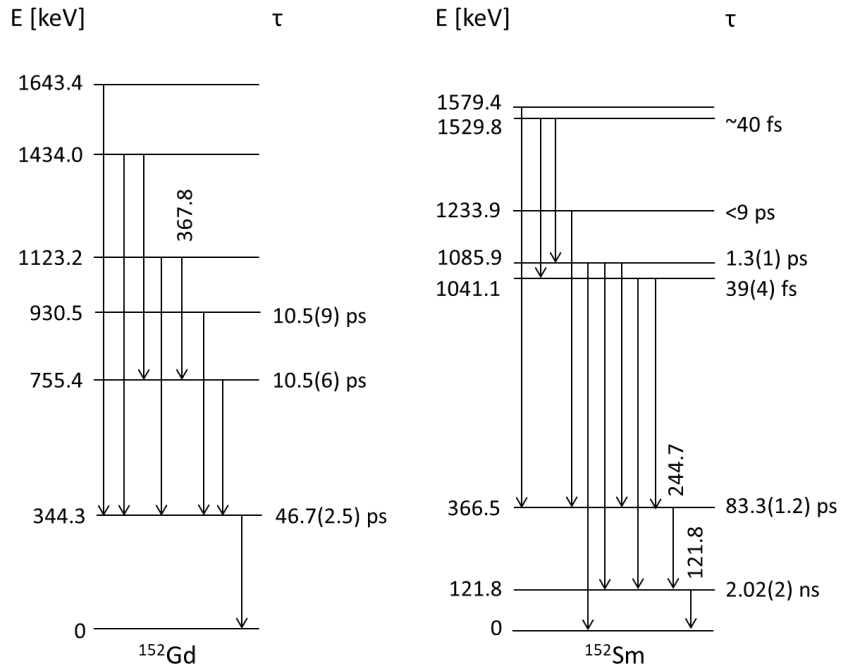

Figure 4.3: Simplified version of the decay scheme of ^{152}Eu to ^{152}Gd and ^{152}Sm, with the energy and the main lifetime of the levels (adapted from [41]).

source and a 78.4(20) kBq ^{133}Ba source are used. These isotopes have many intense γ-rays distributed over the energy range of interest. The detection efficiency, ε [-], which is energy dependent, is then obtained by dividing the count rate, CR [s^{-1}], in a certain γ-peak by the activity, A [Bq], of the source, multiplied with the branching ratio, BR [-], of that specific decay.

$$\varepsilon = \frac{CR}{A \cdot BR} \tag{4.4}$$

Due to their low activity, the Ta foils are measured directly on top of the detector casing in order to capture as many γ-rays as possible. Ideally, the efficiency calibration sources are measured with approximately the same geometry as the foils, so also directly on top of the detector casing. Therefore, the efficiency that is obtained from the ^{152}Eu and ^{133}Ba would be equal to that for the measurements of the foils and no geometrical correction factor would be needed. Unfortunately, this is not possible and the sources need to be measured at a distance further away from the detector, after which a geometrical correction factor is applied to calculate the efficiency for the geometry of the measurement of the foils. The reason for this is twofold.

When the efficiency calibration sources are measured very close to the detector, a problem called summing can occur. ^{133}Ba and certainly ^{152}Eu emit many different γ-rays. Many of these γ-rays are emitted in a cascade of multiple γ-rays that are emitted within a few ns after each other. Figure 4.3 shows a simplified version of the decay scheme of ^{152}Eu to ^{152}Gd and ^{152}Sm. Due to the bad timing resolution of Ge detectors, it is possible that two or more of these γ-rays are seen by the detector as one, such that their energies are summed. When a specific γ-ray sums up with another γ-ray, the count rate for these γ-rays will be smaller than they really are, because some of the counts go to the sum peak.

Contrarily, if the energy of a γ-ray is equal to that of the sum of two other γ-rays, its count rate can be higher due to summing. These so-called summing effects can both increase and decrease the number of counts in a γ-peak, resulting in an efficiency that seems higher or lower than it really is. The probability of summing becomes larger if the detector solid angle is larger. Therefore, the effect can be reduced by increasing the distance between the detector and the source. Correcting for summing effects is really difficult, since it depends on many different factors such as the angular correlation between the different γ-rays. It is possible that summing effects also occur in the measurements of the foils. However, the effect is expected to be smaller due to the low activity. Furthermore, measuring at a larger distance is not possible, because the number of detected γ-rays would be too small to have sufficient statistics.
Another problem that can occur when measuring the efficiency calibration sources directly on top of the detector is dead time. When a γ-ray is detected, the detection system needs some time to process the signal, before a new γ-ray can be detected. This time is called the dead time of a detector. When the dead time of the detector becomes too large compared to the frequency at which particles interact with it, some counts will be lost. From experience, it is known that the detection system of a typical Ge detector suffers from efficiency loss due to dead time when the frequency of photons incident on the detector is around 10 kHz or higher. A quick calculation shows that with the sources directly on top of the detector casing, an incidence frequency of about 12 and 31 kHz is expected for the ^{152}Eu and ^{133}Ba source respectively. This reduced to about 2 and 5 kHz if the distance from the detector casing is increased to 35 mm.

As argued above, the efficiency calibration sources are measured at some distance from the detector. For this, a plastic cap with a height of 35 mm is used. The thus obtained efficiency needs to be corrected for the difference in solid angle to be applicable for the measurements of the foils. This can be done by using equation (4.3). This equation can only be applied for point sources. The ^{152}Eu and ^{133}Ba sources are very small and can therefore be assumed to be point sources. The foils are very thin, but have a diameter of 10 mm. FLUKA simulations are used to check whether they behave as point sources. To use equation (4.3), the radius of the Ge crystal and the distance from the top of the detector casing to the crystal is needed. This cannot be measured, because the Ge crystal is surrounded by an Al casing and a vacuum gap is left between them. The distance from the top of the casing to the beginning of the detector is 5 mm and the radius of the crystal is 25(1) mm, as provided by the manufacturer. The efficiency deduced from the calibration sources needs to be multiplied with $\Omega(d = 5mm)/\Omega(d = 40mm)$, to obtain the efficiency in the geometry of the measurements of the foils. For the ^{152}Eu source another small correction is needed because the actual source is located 1.5 mm deep inside a plastic coin. For the ^{133}Ba source this is not needed, because it is a very thin source.
Once the efficiency at certain energies is known, this curve needs to be fitted. The detection efficiency ε in function of the photon energy is fitted with the following 5 parameter function:

$$\varepsilon = \frac{\sum_{i=0}^{4} a_i \cdot ln(E)^i}{E} \tag{4.5}$$

where the energy, E, is expressed in MeV. This fitting is done with a maximum likelihood fitting routine and the uncertainty is estimated with the use of a random walk through parameter space [42].

4.2.2 Analysis of the spectra

The purpose of the γ-ray energy spectra of the foils is to identify the isotopes that are present in the foils and to obtain their activity, in order to calculate the cumulative cross section. For this, all the peaks in the spectra are first fitted and the possible background is subtracted. The individual peaks are fitted with a Gaussian shape on a linear background, to obtain the energy, the count rate and the FWHM of each peak. Fitting is done with a χ^2 minimisation, that is modified to be suitable for low-statistics counting experiments, from the SATLAS package in python [42].
Subsequently, the different γ-rays have to be linked to possible isotopes they originate from. For this, a database is searched [24]. The procedure is as follows. The energy of a γ-ray is entered in the search bar with an uncertainty of 1 to 2 keV; this includes the energy resolution of the detector and the uncertainty on the energy calibration. To make the search more specific, only a limited number of isotopes is used in the search. Only isotopes with mass number between 100 and 181 and with a half-life between 1 day and 50 years are selected. Isotopes with other masses are not expected to result from spallation reactions and isotopes with other half-lives cannot be detected with this setup. Once a possible isotope is found, it is checked whether its other γ-rays are visible in the spectrum. If this is not the case, the isotope is rejected. This is done for all γ-rays present in the different spectra. Once this is done, the region of the nuclear chart where the spallation products are expected is checked to look for isotopes that are possibly missed in the previous process. This can for example happen for isotopes with a very short half-life, but that result from the decay of a longer-lived isotope. Then, as a third step, the found isotopes are compared with FLUKA simulations. Isotopes that show up in the simulations but not in the measurements are carefully checked. At the end of this process, most γ-rays can be linked to at least one isotope.

Once all isotopes are identified, their measured activity, A_{meas}, is calculated from the count rate, CR, in the peaks. For this, the following equation needs to be solved for every γ-ray:

$$CR = \varepsilon \cdot BR \cdot A_{meas}, \tag{4.6}$$

where ε is the detection efficiency of the detector at the energy of the γ-ray and BR is the branching ratio of the specific decay. Since some γ-rays can come from different isotopes, this means that a coupled set of linear equations needs to be solved, where A_{meas} and CR can be represented as a vector and BR and ε can be combined into a matrix. The easiest way to find the measured activity, A_{meas}, for each of the isotopes is by inverting the matrix and multiplying it with CR. However, this matrix is not a square matrix. Therefore, a Moore-Penrose inverse is used. This is a generalisation of the matrix inverse for singular or non-square matrices and is often used to find the least squares solution to a system of linear equations.

4.2.3 Cumulative cross section

When the activity of the different isotopes present in the foils is known, the cumulative cross section can be calculated. First, for each isotope the activity just after production,

A_0, is calculated. This is done with the following equation (see also Figure 3.3):

$$A_0 = A_{meas} \cdot e^{\lambda t}. \tag{4.7}$$

Here, λ [s^{-1}] is the decay constant of the isotope and t [s] is the decay time, i.e. the time between the end of the production and the middle of the measurement of the γ-ray energy spectrum. Note that this equation assumes that the activity is constant during the measurement, which is justified since the half-life of the isotopes is much longer than the measurement time.
During the production of the isotopes, the number of particles, N, changes in time according to this formula [43]:

$$\frac{dN}{dt} = N_p \cdot d_t a_t \cdot \sigma - \lambda N, \tag{4.8}$$

where N_p [s^{-1}] is the number of protons that hit the target per second, d_t [cm^{-3}] is the number density of the target, a_t [cm] is the thickness of the target and σ [cm^2] is the cross section of the reaction. The first part of equation (4.8) represents the production of a certain isotope and the second part represents its decay. This differential equation can be solved to give:

$$N(t) = \frac{N_p \cdot d_t a_t \cdot \sigma}{\lambda}(1 - e^{-\lambda t}) \tag{4.9}$$

from which follows:

$$A_0 = \lambda \cdot N = N_p \cdot d_t a_t \cdot \sigma(1 - e^{-\lambda t_{irr}}). \tag{4.10}$$

Where t_{irr} is the irradiation time of the target.
As explained before, there are both Ta and Al foils present, where the Al foils are used to deduce the proton current. Equation (4.10) can be written for both Ta and Al:

$$\begin{cases} A_{Ta} = N_p \cdot d_{Ta} a_{Ta} \cdot \sigma_{Ta}(1 - e^{-\lambda_{Ta} t_{irr}}) \\ A_{Al} = N_p \cdot d_{Al} a_{Al} \cdot \sigma_{Al}(1 - e^{-\lambda_{Al} t_{irr}}) \end{cases} \tag{4.11}$$

Here, A_{Ta} and A_{Al} are the activities of the isotopes that are produced in the Ta and Al foils respectively, d_{Ta}, d_{Al}, a_{Ta} and a_{Al} are the density and thickness of the Ta and Al foils, σ_{Ta} and σ_{Al} are the cross sections of the isotopes that are produced in the Ta and Al foils, respectively, and λ_{Ta} and λ_{Al} are their decay constants. Since the cross sections for the isotopes produced from Al are well known, the proton current, N_p, can be calculated by measuring the activities A_{Al}.
The thicknesses of the foils is deduced by precisely measuring their radius and mass, such that $d_t a_t$ [cm^{-2}] can be calculated as:

$$d_t a_t = \frac{m\ N_A}{\pi r^2 M}, \tag{4.12}$$

where m [g] is the mass of the foil, N_A [mol^{-1}] is Avogadro's constant, r [cm] is the radius of the foil and M [g/mol] is the atomic mass of the material it is made of, which can be obtained from [44].
N_p can then be calculated from the second equation in (4.11), using also equation (4.12):

$$N_p = \frac{A_{Al}\pi r^2 M_{Al}}{m_{Al} N_A \sigma_{Al}(1 - e^{-\lambda_{Al} t_{irr}})} \tag{4.13}$$

Combining this with the first line of (4.11) gives:

$$A_{Ta} = \frac{A_{Al}\cancel{\pi r^2} M_{Al}}{m_{Al}\cancel{N_A}\sigma_{Al}(1 - e^{-\lambda_{Al} t_{irr}})} \frac{m_{Ta}\cancel{N_A}\sigma_{Ta}(1 - e^{-\lambda_{Ta} t_{irr}})}{\cancel{\pi r^2} M_{Ta}} \tag{4.14}$$

The cross section for the isotopes produced in the Ta foils can then be calculated:

$$\sigma_{Ta} = \frac{A_{Ta}\ M_{Ta}\ m_{Al}\ \sigma_{Al}(1 - e^{-\lambda_{Al} t_{irr}})}{A_{Al}\ M_{Al}\ m_{Ta}(1 - e^{-\lambda_{Ta} t_{irr}})} \tag{4.15}$$

Note that this cross section is a cumulative cross section because of the way the activity at the end of the irradiation is calculated in (4.7).
Once the activity of the different isotopes in the Ta foils, A_{Ta}, is known, equation (4.15) can be used to calculate their cumulative cross section. However, some other parameters need to be known. The masses of the foils, m_{Ta} and m_{Al}, are measured before the irradiations, and also the irradiation time is known. The activity, A_{Al}, of ^{24}Na, i.e. the isotope produced in the Al foils, is determined in a similar way as is described here for the Ta foils. Finally, the cross section for the production ^{24}Na is obtained from Aleksandrov et al. [45]. These data points have been interpolated to find relevant cross sections for our measurements.
In this work, cross sections will be expressed in millibarn (mb), where 1 mb = 10^{-27} cm^2.

4.3 Results & Discussion

4.3.1 Detector characterisation

Energy calibration

For the detector characterisation, first an energy calibration is performed. For this a spectrum of an ^{152}Eu source is measured for about 45 minutes. The relation between the channel number and the energy is fitted with a linear and a quadratic fit. For this the uncertainty on the channel number is given by the fitting program and the uncertainty on the energy is taken from the literature value. Figures 4.4 and 4.5 show the results of the linear and the quadratic fit, respectively, and the thus obtained fitting parameters are shown in Table 4.1.

Table 4.1: Fitting parameters for the energy calibration. The fit is performed with the following function: $energy = a \cdot channel^2 + b \cdot channel + c$.

	linear fit	quadratic fit
a	0	$-3.3(5) \times 10^{-7}$
b	0.62111(7)	0.6219(1)
c	20.7(1)	20.42(5)
χ^2_{red}	3064	252

The results of the linear and the quadratic fit can now be compared. By looking at Figures 4.4 and 4.5 it is clear that the difference between the two fitting procedures is small. This

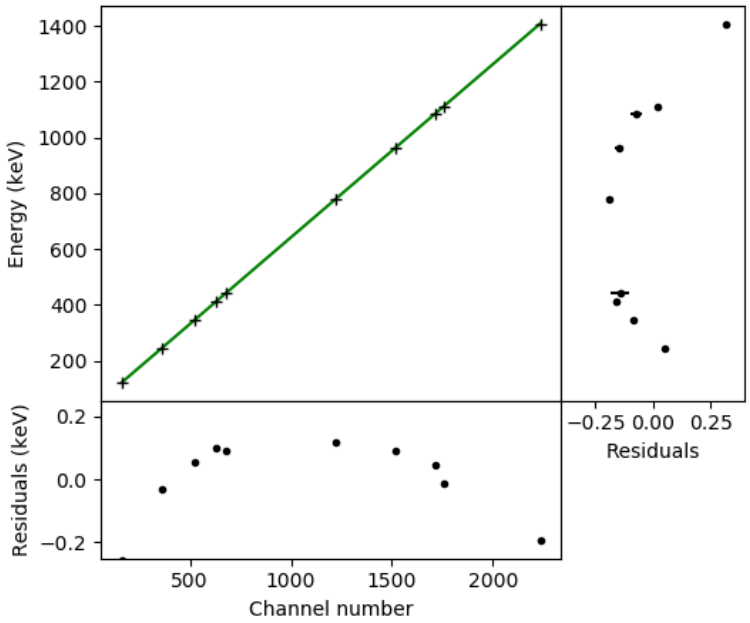

Figure 4.4: The linear energy calibration. The residuals, which are shown in both directions, show a clear trend.

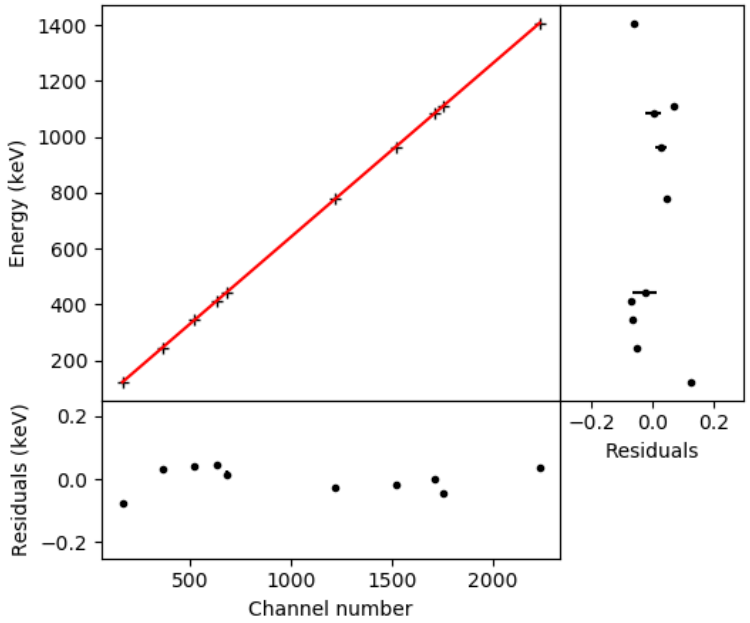

Figure 4.5: The quadratic energy calibration. The residuals show less systematic behaviour than that of the linear calibration.

is also confirmed by the fitting parameters in Table 4.1. The second order fit parameter, a, is very small for the quadratic fit and also the difference between the linear and the quadratic fit is small for the parameters b and c. However, by looking at the residuals in Figures 4.4 and 4.5, the quadratic fit seems to be the best choice. The residuals for the linear fit show a clear trend, which is not present in the quadratic fit. Comparing the χ^2 values in Table 4.1 result in the same conclusion. Although the χ^2_{red} is quite large for both fits, it is significantly smaller for the quadratic fit.
Even though the quadratic fit seems to be better, here it was chosen to work with the linear fit. There are a few reasons to do so. First, a linear calibration is easier to work with in the rest of the work. Moreover, the difference between the two fits is quite small; the maximal difference is of the order of 0.2 keV. This is small compared to the typical FWHM of the peaks, which is of the order of 1 keV. Finally, high precision on the energy is not essential here, since the energy is only needed to identify the isotopes.

Background spectrum

A background spectrum is measured to be able to exclude counts originating from background radiation. For this, a spectrum is measured for about 5 days without a source on the detector. This spectrum is analysed to find the origin of the different photon-peaks. Figure A.1 shows the measured background spectrum with the origin of the most prominent peaks. All the peaks in the spectrum could be assigned to one of the following origins: electron-positron annihilation radiation, X-rays coming from Pb and γ-rays coming from: ^{40}K, ^{108}Tl, ^{212}Pb, ^{214}Pb, ^{214}Bi, ^{226}Ra, ^{228}Ac, ^{238}Th and ^{234}Pa.

Detection efficiency

To determine the efficiency with which the detector detects γ-rays, two sources with known activity are measured, i.e. ^{152}Eu and ^{133}Ba at a distance of 40 mm from the Ge crystal. The most intense peaks in these spectra are fitted in order to deduce their count rates. Then, equation (4.4) is used to calculate the efficiency. The branching ratios of the different γ-rays are obtained from [40]. The activity of the sources is equal to 30.2(9) kBq for ^{152}Eu and 78.4(20) kBq for ^{133}Ba at the time of the measurement.
The efficiency that is thus obtained, needs to be corrected for the difference in solid angle between the measurement of the sources and the foils. For this, it is first checked whether the Ta foils can be assumed point sources. This is done by comparing FLUKA simulations where a thin cylinder and a point source are used as a source. They give the same results within error bars. Therefore, equation (4.3) can be used to calculate the difference in solid angle.

To check the effect of summing and dead time, the ^{152}Eu source is also measured close to the detector. Figure 4.6 shows the efficiency of the detector as a function of the energy of the γ-ray, obtained from the measurements of ^{152}Eu, both close to the detector and further away. Both data sets are corrected for the solid angle and, therefore, show the corresponding efficiency for the geometry of the foils, directly on top of the detectors. The two data sets should overlap, which is not the case. This effect is attributed to efficiency loss due to dead time when measured close to the detector.

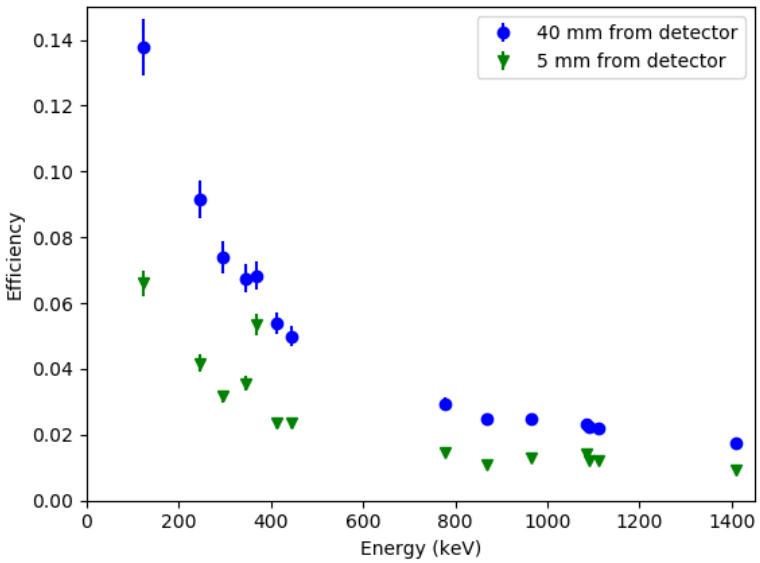

Figure 4.6: Detection efficiency determined from two measurements of the ^{152}Eu source. Data obtained from the measurement at 40 mm from the detector crystal is indicated with blue dots and data from the measurement at 5 mm from the detector with green triangles. Both data sets are corrected for the solid angle and therefore correspond to the efficiency in the geometry of the measurement of the Ta foils.

Moreover, this figure shows that the measurement close to the detector suffers from summing problems. As a result, not all data points follow the same trend. Certainly the point at 367.8 keV is clearly affected by summing. The reason for this can be seen in Figure 4.3. Two of the most intense γ-rays of ^{152}Eu, namely the one at 244.7 keV and the one at 121.8 keV follow each other in a cascade and sum up to a γ-ray with an energy of 366.5 keV. This is very close in energy to the γ-ray at 367.8 keV, which has a much smaller branching ratio (0.8 % compared to 7.6 % and 28.6 %). As a result, many of the counts in the 367.8 keV peak are actually counts originating from summing. Also in the measurement further away from the detector, this point does not completely match with the rest of the points. Based on this argument, this data point is removed. Note that the number of counts that is lost in the 244.7 keV and the 121.8 keV peaks is negligible, because their branching ratios are much larger.

Next, the curve of the efficiency as a function of energy is fitted with equation (4.5). For this the efficiency is calculated from ^{152}Eu and ^{133}Ba, both are measured at a distance of 40 mm from the detector crystal and corrected for the solid angle, using equation (4.3). Figure 4.7 shows this fit with its uncertainty. Furthermore, a slight discrepancy between the values obtained from ^{152}Eu and ^{133}Ba can be observed, although the data matches within 1 σ.

From this fit, the efficiencies for each of the different γ-rays in the foils can be deduced. However, one of the foils, the one irradiated with 900 MeV protons, is slightly bend. Therefore, the efficiency of this foil will be smaller compared to the efficiency curve, as a

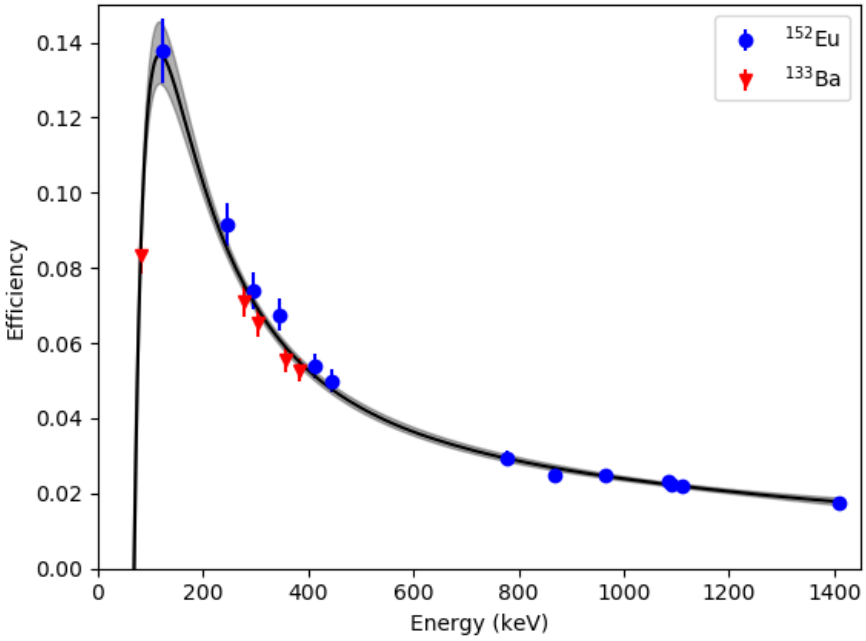

Figure 4.7: Efficiency curve of the Ge detector corrected for the geometry of the measurement of the Ta foils. Data is obtained from a ^{152}Eu and a ^{133}Ba source, both measured at 40 mm from the detector crystal. The full line is a fit to the data according to equation (4.5) and the shaded area represents the uncertainty from the fit.

part of the foil is further away from the detector. Therefore, the efficiency is recalculated for the case that the whole foil is at the maximum distance from the detector; this distance is 4 mm. The average efficiency between the two is taken and a systematic error of half the difference in efficiency is included.

4.3.2 Analysis of the spectra

Isotope identification

Gamma-ray energy spectra are measured for 9 different foils. Each spectrum is measured for a few days up to a week, in order to attain enough statistics. The spectra are measured at least one month after the irradiations. Therefore, all isotopes with a half-life shorter than a few days will have completely decayed. Figure B.1 shows an example of a spectrum together with the origin of some of the most prominent peaks.
For each peak in the spectrum, the count rate and the energy are obtained by fitting the peaks with a Gaussian line profile. Figure B.2 shows an example of a few γ-peaks that are fitted. To obtain the correct count rate, possible background peaks are subtracted. Then, the different γ-rays can be assigned to different isotopes. After going through the complete procedure described in the first part of section 4.2.2, most of the γ-rays in the spectra can be attributed to at least one isotope. For each foil that is analysed, also a simulation is done to calculate the activity of the different isotopes created in the foils. However, for the simulations, only one foil is used instead of the complete stack of foils that is used for the real experiment. By doing one of the simulations also with the complete stack and by comparing the results, it is confirmed that this yields the same results within uncertainty. This is because FLUKA does not take recoil into account.
The isotopes found in the measurement are compared with those in the simulations. From this, it is found that some isotopes present in the simulations are not seen in the measurements. For all these isotopes, the reason of this discrepancy is checked. Table 4.2 shows the isotopes that are found in the simulations, but not in the measurements for any of the foils, together with their possible explanation. Besides that, there are also some isotopes that are found in only some of the foils, namely ^{173}Lu, ^{172}Lu and ^{171}Lu. For these isotopes it was not possible to properly fit the γ-peaks in some foils. Finally, there are isotopes, which are found in the measurement, but not in the simulations. These isotopes are not (yet) removed. If they are indeed not present in the foils, their activity should become zero when it is calculated.

Activity calculation

Most γ-peaks in the spectrum can be assigned to one or more isotopes. Now the activity of these isotopes can be determined in the different foils by solving the matrix equation (4.6). As explained in section 4.2.2, this is done by inverting the matrix which contains the efficiencies and the branching ratios and then multiplying it with the count rates. This method is easy to implement, but has one weakness, i.e. one cannot impose boundary conditions on the obtained results. Therefore, negative activities, which are of course not physical, cannot be excluded from the solution. This turns out to be a problem, because

Table 4.2: Isotopes that are seen in the simulations, but not in the measurements. When the γ-rays are in a region that makes them difficult to detect this can be because the efficiency is low there or because there is a large background of other γ-rays.

^{179}Ta	no γ-rays
^{178}W	no γ-rays
^{178}Ta	γ-rays with small BR or in an energy region difficult to detect
^{177}Ta	γ-rays with small BR
^{174}Lu	γ-rays with small BR or in an energy region difficult to detect
^{159}Dy	γ-rays with small BR
^{145}Sm	γ-rays with small BR or in an energy region difficult to detect
^{131}Cs	no γ-rays
^{125}I	γ-rays in an energy region difficult to detect

when the activity is calculated, some isotopes seem to have a negative activity. Therefore, these isotopes are thoroughly analysed by checking if their γ-rays overlap with those of other isotopes. If this is the case it is possible that they just 'match' with the γ-rays in the spectra, but are not really present. All isotopes, for which negative activities are found, have overlapping γ-rays with other isotopes. Furthermore, we look at the results from the simulations. All isotopes that give a negative activity, are not present in the simulations or only in very small (not detectable) amounts. Based on these arguments, these isotopes are removed from the activity calculations.
Subsequently, the activity of the residual isotopes is recalculated and compared to the simulations. The resulting activities of the isotopes, together with their half-lives are shown in Table 4.3. From this table, multiple things can be concluded. First, it shows that the method applied here is only sensitive to isotopes with a half-life between multiple days and a few years. Shorter-lived isotopes will have completely decayed before the spectra are measured and longer-lived isotopes do not emit enough γ-rays to result in a detectable signal. ^{172}Lu and ^{146}Eu have a quite small half-life ($t_{1/2}$ = 6.7 d and 4.61 d). The reason they can be found in the spectra is because their parents ^{172}Hf and ^{146}Gd have a long half-life ($t_{1/2}$ = 1.87 y and 48.27 d). Moreover, this table shows that at higher proton energies, lower mass spallation products are created. This can be expected, because higher energetic protons can more easily split off more protons and neutrons from the target atom. Finally, one can see that for all isotopes, more neutrons are ejected than protons during the production. It was already explained in section 3.2 that this is because neutrons are not affected by the Coulomb barrier and, therefore, are more easily released.

As an example, Figure 4.8 shows the experimental and simulated activity of the different isotopes present in the foil that was irradiated with 600 MeV protons. This figure shows that for most isotopes, the measured activity matches with the simulated activity. However, for other isotopes, there is a discrepancy between the results of the measurement and the simulation. The origin of this is unclear. As explained before, the simulations are done with an estimate of the proton current obtained during the experiment. However, if this were the problem, one would expect to see a shift for all isotopes, which is not the case. Therefore, for some isotopes, probably the activity is not correctly deduced, either from the measurement or from the simulation. Similar results are obtained for the other

Table 4.3: Isotopes for which the activity is calculated.

Energy (MeV)	300	300	500	600	700	900	1100	1300	1700
Thickness (μm)	6	2	6	6	6	6	6	6	6
Half-life									
70 d	^{175}Hf	^{175}Hf	^{175}Hf	^{175}Hf	^{175}Hf	^{175}Hf	^{175}Hf	^{175}Hf	^{175}Hf
1.37 y	^{173}Lu	^{173}Lu	^{173}Lu			^{173}Lu	^{173}Lu		
1.87 y	^{172}Hf	^{172}Hf	^{172}Hf	^{172}Hf	^{172}Hf	^{172}Hf			
6.7 d	^{172}Lu	^{172}Lu	^{172}Lu	^{172}Lu	^{172}Lu	^{172}Lu		^{172}Lu	^{172}Lu
8.24 d	^{171}Lu	^{171}Lu	^{171}Lu	^{171}Lu	^{171}Lu	^{171}Lu			
32.026 d	^{169}Yb	^{169}Yb	^{169}Yb	^{169}Yb	^{169}Yb	^{169}Yb	^{169}Yb	^{169}Yb	^{169}Yb
9.25 d	^{167}Tm	^{167}Tm	^{167}Tm	^{167}Tm	^{167}Tm	^{167}Tm	^{167}Tm		
240.4 d			^{153}Gd	^{153}Gd	^{153}Gd	^{153}Gd	^{153}Gd	^{153}Gd	^{153}Gd
124 d			^{151}Gd	^{151}Gd	^{151}Gd	^{151}Gd	^{151}Gd	^{151}Gd	^{151}Gd
9.28 d			^{149}Gd	^{149}Gd	^{149}Gd	^{149}Gd	^{149}Gd	^{149}Gd	^{149}Gd
93.1 d			^{149}Eu	^{149}Eu	^{149}Eu	^{149}Eu	^{149}Eu	^{149}Eu	^{149}Eu
24.1 d			^{147}Eu	^{147}Eu	^{147}Eu	^{147}Eu	^{147}Eu	^{147}Eu	^{147}Eu
48.27 d			^{146}Gd	^{146}Gd	^{146}Gd	^{146}Gd	^{146}Gd	^{146}Gd	^{146}Gd
4.61 d			^{146}Eu	^{146}Eu	^{146}Eu	^{146}Eu	^{146}Eu	^{146}Eu	^{146}Eu
265 d					^{143}Pm	^{143}Pm	^{143}Pm	^{143}Pm	^{143}Pm
137.640 d				^{139}Ce	^{139}Ce	^{139}Ce	^{139}Ce	^{139}Ce	^{139}Ce
36.4 d						^{127}Xe	^{127}Xe	^{127}Xe	^{127}Xe
16.78 d								^{121}Te	^{121}Te
115.09 d									^{113}Sn
51.29 d									^{105}Ag

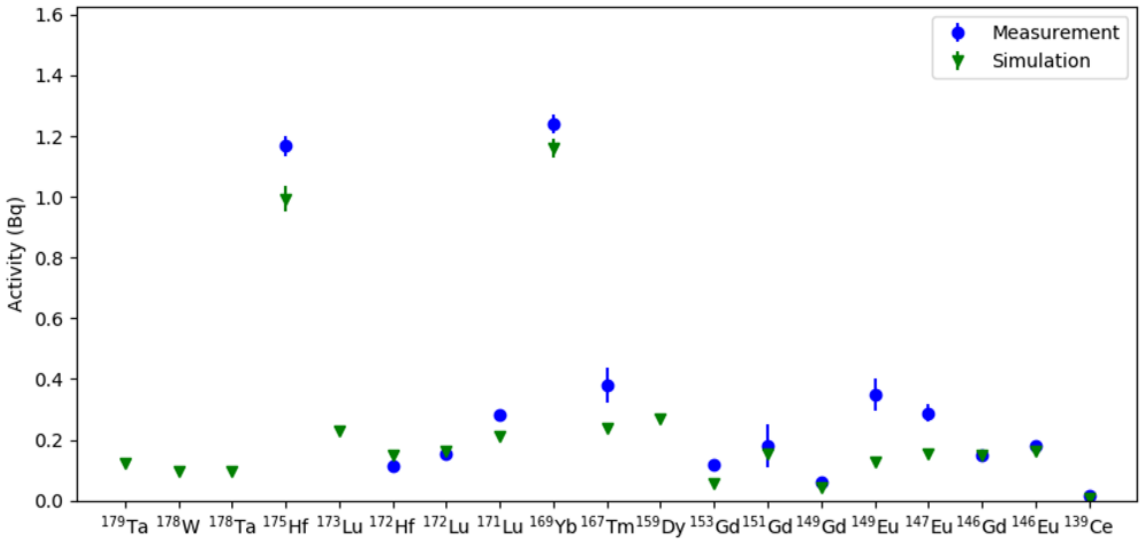

Figure 4.8: Activity obtained from measurement and simulation for the foil that is irradiated with 600 MeV protons.

foils, as is shown in Figure 4.9. This figure shows the ratio of the activity obtained from the measurements to the activity obtained from the simulations. From this figure, it is clear that for some isotopes, e.g. ^{175}Hf and ^{169}Yb, the results from the measurements and the simulations match very good for all foils. The reason for this is probably that these isotopes result in a high activity, which makes them easier to measure. For isotopes such as ^{149}Eu, there seems to be a consistent discrepancy between the simulations and the measurements. This indicates that the problem probably lies in the simulations, because it is very unlikely to measure the activity wrong in each foil. However, other isotopes, such as ^{167}Tm seem to suggest that in some foils the activity was calculated wrong, while in others it was not. This indicates more that there is a problem with the measurement. From this figure, it can also be seen that for lower masses, the discrepancy between measurements and simulations becomes larger. This is probably because these isotopes are produced in small amounts, making it difficult to deduce their activity, both in the measurements and in the simulations.

4.3.3 Cumulative cross section

Before the cumulative cross section can be calculated from equation (4.15), the data from the Al foils is needed, as explained at the end of 4.2.3. More specifically, we need the activity for ^{24}Na and the cross section as a function of energy for the well known ^{27}Al(p,$*$)^{24}Na reaction. Moreover, the masses of the foils need to be known. Here, a few problems occur. A first problem is that only preliminary results are available for the activities of ^{24}Na at the moment of this analysis. It is mainly uncertain whether the efficiency of the detectors used to measure the γ-ray energy spectra from the Al foils is

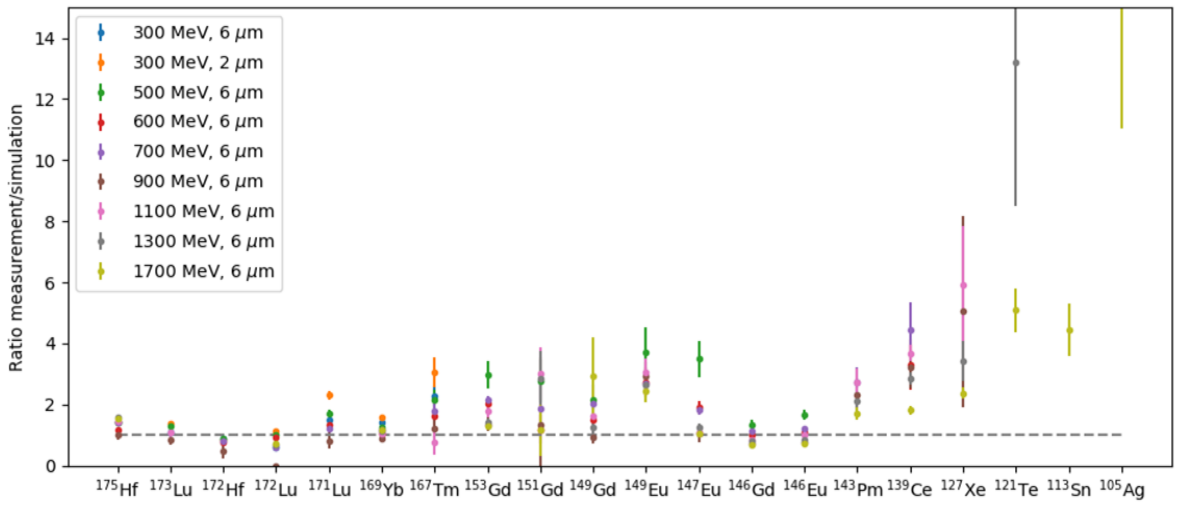

Figure 4.9: Ratio between the activities obtained from measurements and simulations for all isotopes in the foils. For clarity, only the ratios below 15 are shown in this graph. However, for ^{105}Ag the ratio is larger than 15.

determined correctly. Despite these concerns, it was decided to use these values as current best estimates. For the irradiation with 1100 MeV protons, the masses of the Ta and Al foils are not measured. However, since all foils are cut from one larger foil, one can assume that they will have approximately the same mass. Therefore, the masses of the Ta and the Al foil used during this irradiation are assumed as the average of the masses of the other Ta and Al foils. The cross sections for the production of ^{24}Na are obtained from Aleksandrov et al. [45]. The different data points are fitted with the following function that relates the cross section, σ, in mb to the proton energy in MeV.

$$\sigma = a + b \cdot \sqrt{E} + c \cdot E + d \cdot E^2 \tag{4.16}$$

The fit and the obtained fitting parameters are shown in Figure 4.10 and Table 4.4.

Table 4.4: Fitting parameters for the cross section of the production of ^{24}Na by proton-induced reactions in Al. The fit is performed with equation (4.16).

	^{24}Na
a	1.1(5)
b	$8.4(5) \times 10^{-1}$
c	$-2.0(1) \times 10^{-2}$
d	$2.6(2) \times 10^{-6}$
χ^2_{red}	0.31

Now the cumulative cross sections of the different isotopes can be calculated from equation (4.15). However, for some isotopes the cumulative cross section cannot be calculated, because for these isotopes one cannot assume that their parent isotopes have completely decayed. These isotopes are ^{172}Lu, ^{149}Eu and ^{146}Eu, because their parents ^{172}Hf, ^{149}Gd and ^{146}Gd are also present in the spectra. For the other isotopes, it is carefully checked that

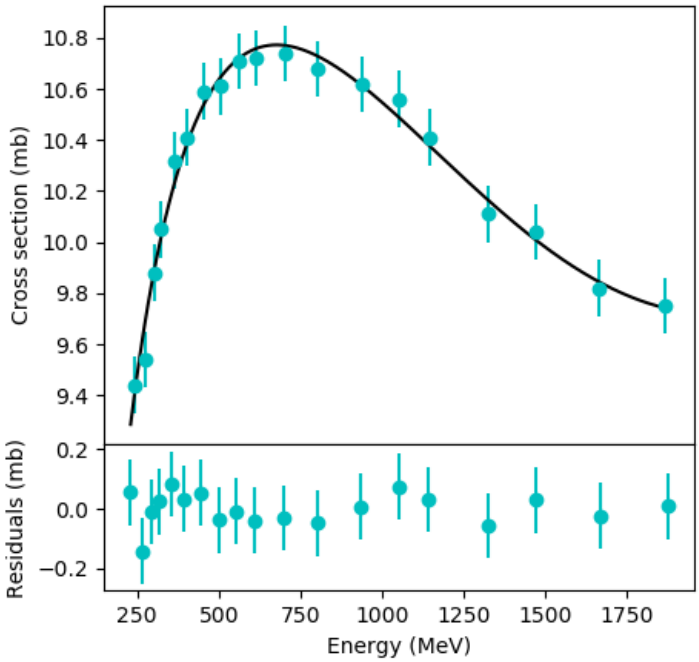

Figure 4.10: Cross section in function of the proton energy for the production of ^{24}Na by the reaction Al(p,$*$)^{24}Na. Data is obtained from [45] and fitted with function (4.16).

their parent isotopes are short-lived. The longest-lived parent is ^{153}Tb ($t_{1/2}$ = 2.34 d), which is the parent of ^{153}Gd. It emits a high intensity (BR = 31 %) γ-ray at 212 keV. This means that if it would be present in the foils, it would have been detected. It is concluded that for all isotopes for which an activity is calculated, except for ^{172}Lu, ^{149}Eu and ^{146}Eu, the cumulative cross section can be determined.

Table 4.5 shows the cumulative cross sections for the production of different isotopes by proton-induced spallation of Ta targets as a function of the energy of the incident protons. One can see that in general the cumulative cross section becomes smaller for lighter nuclei. This indicates that it is more difficult to remove many particles from the Ta nuclei than it is to remove a few. Moreover, it is clear that at higher proton energies more particles are removed from the Ta nuclei, resulting in lower mass spallation products. The evaporation of nucleons during the spallation process becomes more efficient at higher proton energies. This can also be seen by comparing Figures 4.11a, 4.11b and 4.11c. They show the cumulative cross sections as a function of the energy of the incident protons for ^{169}Yb, ^{153}Gd and ^{139}Ce, respectively. Graphs for the other isotopes can be found in appendix C. When going from high to low mass nuclei, the maximum cumulative cross section shifts to higher energies. Moreover, these figures show that in general the cumulative cross section becomes smaller for smaller mass nuclei.
By comparing the results with literature values one can see that, qualitatively, the results follow the same trend as can be found in literature [46, 47]. However, quantitatively there is a discrepancy between the two for some isotopes. The measurements here seem to result in a higher cumulative cross section than what is found literature. A possible explanation

Table 4.5: Cumulative cross sections in mb.

Energy (MeV)		300	300	500	600	700	900	1100	1300	1700
Thickness (μm)		6	2	6	6	6	6	6	6	6
Nuclide	Half-life									
^{175}Hf	70 d	159 ±7	162 ±9	115 ±4	93 ±3	94 ±4	61 ±11	73 ±3	74 ±4	59 ±3
^{173}Lu	1.37 y	123 ±12	155 ±11	112 ±6			55 ±10	56 ±13		
^{172}Hf	1.87 y	93 ±11	84 ±14	68 ±11	57 ±9	49 ±9	27 ±13			
^{171}Lu	8.24 d	162 ±7	1718 ±11	143 ±8	114 ±7	84 ±11	51 ±17			
^{169}Yb	32.026 d	113 ±4	117 ±6	98 ±3	82 ±3	80 ±3	52 ±7	57 ±3	54 ±3	44 ±2
^{167}Tm	9.25 d	127 ±19	129 ±20	133 ±20	109 ±17	109 ±17	73 ±19	39 ±21		
^{153}Gd	240.4 d			19 ±2	22 ±2	32 ±2	29 ±5	41 ±4	37 ±4	27 ±2
^{151}Gd	124 d			27 ±7	21 ±8	42 ±18	44 $^{+74}_{-44}$	105 ±29	99 ±31	36 ±26
^{149}Gd	9.28 d			10 ±2	17 ±2	30 ±3	23 ±6	46 ±17	41 ±14	85 ±37
^{147}Eu	24.1 d			17 ±3	21 ±2	34 ±3	35 ±9	46 ±4	57 ±5	45 ±4
^{146}Gd	48.27 d			4.6 ±0.4	10 ±1	19 ±1	22 ±5	30 ±2	34 ±3	29 ±2
^{143}Pm	265 d					14 ±3	25 ±6	47 ±7	48 ±6	44 ±5
^{139}Ce	137.640 d				2.1 ±0.3	6.6 ±0.5	13 ±3	31 ±2	38 ±3	39 ±2
^{127}Xe	36.4 d						2.9 ±0.6	6 ±1	11 ±1	22 ±1
^{121}Te	16.78 d								13 ±3	21 ±3
^{113}Sn	115.09 d									8 ±1
^{105}Ag	51.29 d									6 ±2

for this is that the activities of ^{24}Na obtained from the Al foils are not completely correct. As explained before, these data are only preliminary and should still be thoroughly analysed. Because not all Al foils are measured with the same detector, discrepancies here can affect the different data points separately. It is also possible that the detector efficiency for the measurement of the Ta foils is not correct. However, this should affect all data points by shifting them with the same factor. Another possible explanation of why the measured cross sections do not completely match with literature is that, although the spectra were thoroughly analysed, still some isotopes are missed. This would mean that the same total amount of activity is shared between fewer isotopes, which would result in a too high activity and, therefore, cumulative cross section. This is expected to have a different impact on different isotopes and, therefore, could explain why there is a better match with literature for some isotopes compared to others.
The uncertainty on the calculated cumulative cross sections is mainly due to the uncertainty on the activity of the different isotopes in the foils. The main origin for this is the small amount of statistics in the γ-ray energy spectra. For example for ^{151}Gd, ^{149}Gd, ^{143}Pm, ^{121}Te and ^{105}Ag, the uncertainty on the cumulative cross sections is at most energies above 20 %. For these isotopes only one or two γ-rays can be found in the spectra. Moreover, these γ-peaks are all very small or are shared between multiple isotopes, such that the uncertainty on the number of counts is large. The uncertainty on the efficiency of the Ge detector is of the order of 5 %. For most isotopes this is not important. However, for isotopes such as ^{175}Hf and ^{169}Yb, which have many different, high intensity γ-rays, it does contribute, because the uncertainty on the count rate is very small. One can see that the uncertainty on the cumulative cross section is larger at 900 MeV than at the other energies. As explained before, this is because this foil was bend and a systematic uncertainty was added to the detector efficiency for that foil.

In the context of the production of Tb isotopes for medical applications, we are here mainly interested in the cumulative cross section of ^{139}Ce, because this isotopes is known to be often present as an isobaric contamination under the form of ^{139}Ce^{16}O in the collection of ^{155}Tb [29]. From literature [46, 47], it is known that the cumulative cross section of ^{155}Tb shows a maximum at a proton energy of around 800 MeV. Figure 4.11c shows that for ^{139}Ce the maximum is at a much higher energy, while the cross section is small at about 800 MeV. Therefore, it is recommended to use low proton energies, of about 800 MeV or lower, for the production of ^{155}Tb by proton-induced spallation of Ta in order to minimise the contamination with ^{139}Ce.
ISOL@MYRRHA is an isotope separation on-line facility that is under development at SCK•CEN in Mol. This facility will operate with a proton beam at 600 MeV and, therefore, should be nearly ideal for the optimised production of ^{155}Tb [48].

As explained before, the here performed γ-analysis is part of a larger collaboration. Figure 4.12 shows the cumulative cross sections for ^{149}Tb, that is obtained from an α-analysis of the same foils just after their irradiation. The activities at the end of the irradiation are calculated by other people. From this, the cumulative cross section is calculated as described in section 4.2.3. At each energy, two data points are shown, because for each irradiation, both the 2 μm and the 6 μm foil is analysed. One can see from this figure that the cumulative cross section at 900 MeV seems to be too small. This is also seen in the results of the here performed γ-analysis. Therefore, the origin of this probably lies in the calculation of the activity of ^{24}Na at this energy. The Al foil from which this activity

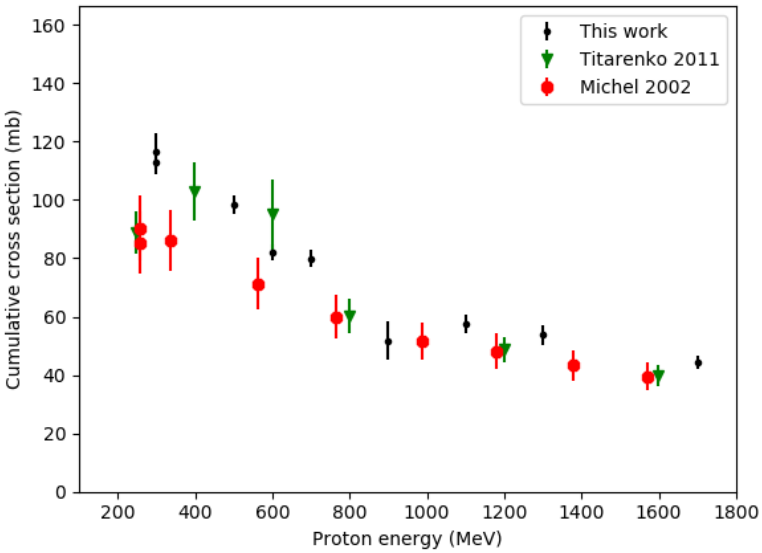

(a) ^{169}Yb

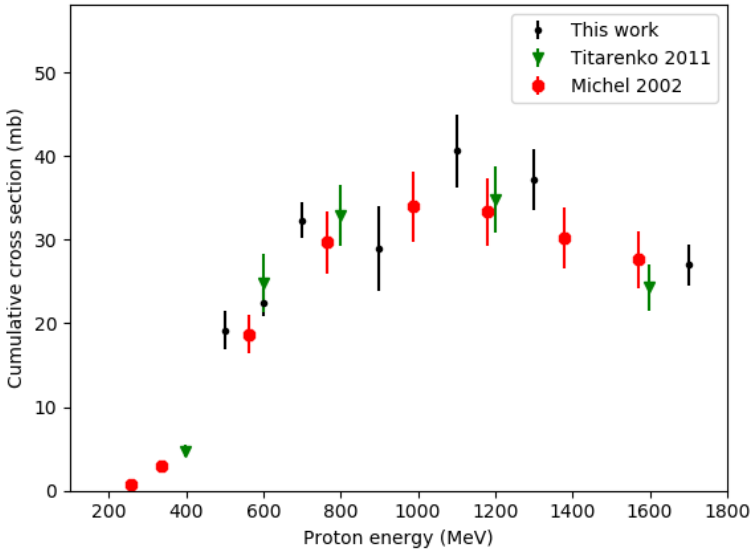

(b) ^{153}Gd

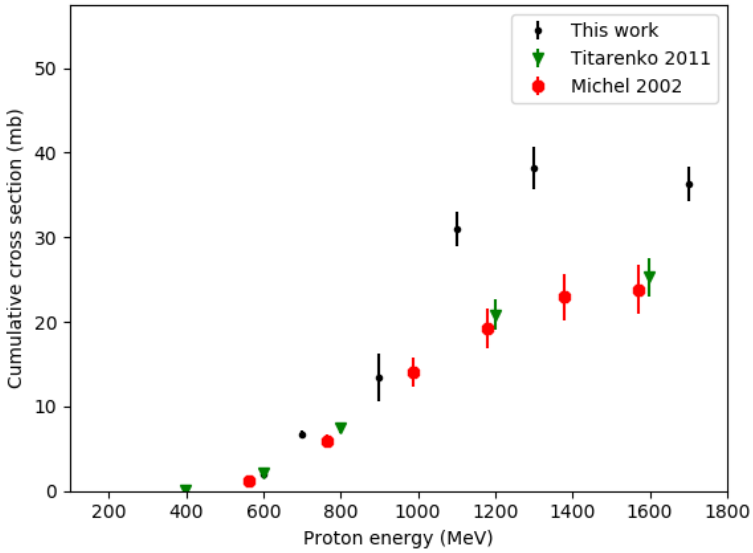

(c) ^{139}Ce

Figure 4.11: Cumulative cross section as a function of incident proton energy.

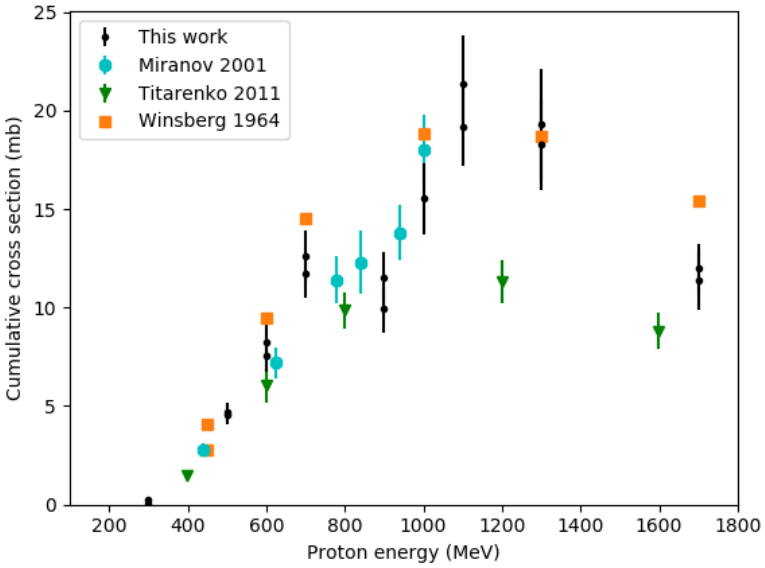

Figure 4.12: Cumulative cross section as a function of incident proton energy for ^{149}Tb [46, 1, 2].

is calculated, is the only one that was measured with a certain detector. If the efficiency of this detector is underestimated, this would explain the here obtained results. One can see that there is a discrepancy between different literature values. If the cumulative cross section at 900 MeV is indeed wrong, the results presented here seem to favour the values of Winsberg [1] and Miranov [2] over the values of Titarenko [46].

As a conclusion to this chapter, we can say that the analysis of γ-ray energy spectra has led to new cumulative cross section measurements. These measurements are performed at different energies, compared to what is available in literature and, thus, complete the existing data sets. The data on ^{139}Ce shows that for the production of ^{155}Tb by proton induced spallation of Ta targets, operation at or below 800 MeV is preferable. Therefore, ISOL@MYRRHA, which will operate at 600 MeV, will be almost optimal for the production of ^{155}Tb. There are still some uncertainties on the normalisation from the measurements of the Al foils, specifically related to the activity of ^{24}Na. These will be addressed in the coming months.
Besides the results from the γ-analysis, new cumulative cross section data on ^{149}Tb is presented. These results show that the literature values of Winsberg [1] and Miranov [2] are preferred.

5 | First isotope collection at CERN-MEDICIS

The extraction efficiency of isotopes depends on the temperature to which the target is heated. Some isotopes will be released at lower temperatures than others will, depending on chemical parameters such as diffusion through the target matrix and vapour pressure. Therefore, selecting a correct temperature can be used to improve the collection of isotopes of interest. This is investigated at CERN-MEDICIS, where off-line isotope separation is used to collect ^{155}Tb from the irradiation of a Ta target with 1400 MeV protons. This is the first collection of radioisotopes from the CERN-MEDICIS facility. This experiment also allows checking the reliability of FLUKA simulations that are done to estimate the radiation dose for people working in the MEDICIS experimental hall. For this, simulations are compared with data from radiation monitors in the experimental hall at the time of the collection.

5.1 The CERN-MEDICIS facility

CERN-MEDICIS (MEDical Isotopes Collected from ISOLDE) is a specialised facility for the collection of radioactive isotopes for medical applications. About 50 % of the protons that are accelerated to 1400 MeV in the Proton Synchrotron Booster (PSB) at CERN are sent onto a target at the Isotope Separation OnLine DEvice (ISOLDE). This allows for the production of beams of many different stable and radioactive nuclides that can be used for research in the many different experimental setups at ISOLDE. About 85 % of the protons that are send onto the ISOLDE target traverse it without interaction and hit the beam dump. To partly recover these protons, a second target, the MEDICIS target, is placed behind the ISOLDE target. This allows CERN-MEDICIS to take advantage of the protons of ISOLDE, while it does not disturb its operation. After irradiation, the MEDICIS target is transported to the CERN-MEDICIS facility by a rail conveyor system. There, the target is placed in a shielded decay and monitoring area. The time it stays there depends on the isotope that one wants to collect and on the type of target. Subsequently, the target can be transferred to a hot cell for further preparation or it is directly connected to the separator, after which isotopes can be extracted as explained in section3.1 [30]. In the experiment described in this chapter, surface ionisation is used to ionise the extracted species.

5.2 First isotope collection

On the 11th and 12th of December 2017 for the first time radioactive isotopes were delivered from CERN-MEDICIS. Three batches were collected, resulting in about 100 Bq of ^{155}Tb [49]. However, the future goal is to collect up to a few GBq per week [30]. During these three collections, the target was at a different temperature each time. Possibly, some isotopes are extracted more efficiently from the target than others at a specific temperature. This is checked with this first collection. Moreover, this collection allows making a comparison between the ambient dose in the MEDICIS experimental hall predicted by FLUKA simulations and measured by radiation monitors.

5.2.1 Temperature dependence of the collection

During the collection of ^{155}Tb one expects also to collect isobaric contaminants, among which ^{139}Ce^{16}O [29]. To extract the produced isotopes from the target, it is heated to temperatures between 1750 and 2050 °C. This is done by applying a high current through the casing of the target. For each of the three batches that are collected, a different current is applied to the target, so a different temperature is used for the extractions. It is expected that depending on the temperature, different isotopes may be collected. As explained in section 3.1, the extraction of atoms or molecules from the target is based on their diffusion and effusion behaviour. These are chemical effects and, therefore, different isotopes of the same element will be extracted in the same way. Important properties are for example the melting point and the vapour pressure. Elements with a low melting temperature and a high vapour pressure are released more easily. By forming volatile compounds such as fluorides or oxides, elements that are normally difficult to extract, can be released from the target more easily [50].
To correlate the current to the temperature of the target, a target calibration is performed. For this, information from the data sheet of the target is used, after which this is fitted with a linear or a quadratic curve with a least square method. The temperature, T [°C], of the target is expected to be proportional to the power, P [W], that is dissipated, which is equal to the resistance, R [Ω], multiplied with the current, I [A], squared.

$$T \propto P = R \cdot I^2 \tag{5.1}$$

Unfortunately, data for the target calibration is given without an uncertainty, such that a proper analysis is difficult. The data on the data sheet is measured before the target is irradiated, so possible influences of the radioactivity are not included. However, these effects are expected to be small. In addition, the effect of the line which connects the target to the separator and which is heated, is expected to be small.
After the collections, a quick analysis is performed to determine which isotopes are collected.

5.2.2 Ambient dose equivalent

Because this is the first isotope collection at CERN-MEDICIS, this is the first time simulations of the ambient dose equivalent can be verified experimentally. For this purpose,

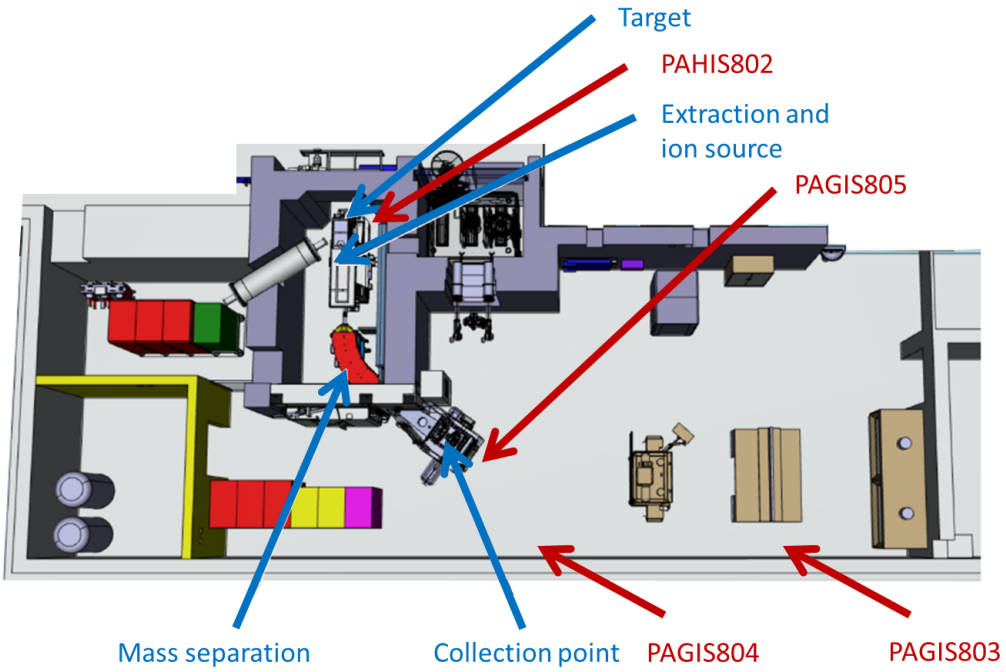

Figure 5.1: Top view of the CERN-MEDICIS experimental hall with the four radiation monitors: PAHIS802, PAGIS803, PAGIS804 and PAGIS805 (adapted from [51]).

simulations are compared to the ambient dose equivalent rates measured by four different detectors in the experimental hall. Figure 5.1 shows a top view of the CERN-MEDICIS facility with the location of the four detectors. PAHIS802 is located near the irradiated target, PAGIS805 is located near the collection point and PAGIS803 and PAGIS804 are located on the wall in the experimental hall. The positions of the detectors are measured with a tape measure. Because the position of PAGIS805 was changed just before the experiment, the position of this detector is estimated based on photographs.

The simulations that are performed here are based on work of a previous student [51]. Only slight adaptations are needed to use these simulations: these include the addition of some extra shielding that was purposely set during the experiment. The ambient dose equivalent rate is simulated in the same four detectors as the measurements, to be able to compare the simulations and the measurements. This is done after each collection. The simulations are split into two parts. In the first part, the dose due to the presence of the irradiated target is simulated. The second part of the simulations represents the collections of radioisotopes.

Although the irradiated target is located in the bunker, which is separated from the experimental hall by a thick concrete wall, it can still contribute to the ambient dose equivalent in the hall. The main reason for this is that a hole is left in the wall through which the beamline passes.
Simulating the contribution of the irradiated target poses some difficulties. In reality, the MEDICIS target is irradiated at a different location compared to where the isotopes extraction happens. However, FLUKA can only simulate on-line target activation, such

that the irradiation and the extraction happen at the same location. To solve this, the target in FLUKA is surrounded by a special material. This material stops all incoming protons, while it leaves the produced particles untouched. The target is then placed in the geometry of the extraction, where it is irradiated. In this way, off-line target activation can be simulated with FLUKA. For the simulation of the target irradiation, information from the logbook of the experiment is used to do the simulation with the correct proton current and irradiation time. A current of $1.9{\cdot}10^{12}$ protons per second is used over an irradiation time of 24 hours. The time between the irradiation of the target and the start of the collections is also obtained from the logbook and is about 4 days.
Beside an estimate of the ambient dose equivalent, this simulation also provides information on which isotopes are produced in what quantities, which will become important in the second part of the simulations.

The second contribution to the ambient dose equivalent is the collection of radioisotopes. Because the collection point is located in the experimental hall, this is expected to give a large contribution to the dose. To estimate the ambient dose equivalent, the trajectories of the different isotopes through the separator magnet is simulated. For this, beams of different isotopes are defined. It is important to not only define a beam for nuclides that are collected, but also for other isotopes of the same element. Although they will not reach the collection point, these isotopes will be extracted from the target and will be deposited on the walls and the slits in the mass separator, where they will still contribute to the dose. After the collection, the collected samples are analysed to deduce which isotopes are present. This information is used to determine which beams should be defined in the simulations. During the experiment, the beam current of the collected beam is measured. This is used to define the beam current of the collected isotopes in the simulations. The relative yield of the species that are produced in the target is then used to calculate the beam current of the other isotopes of the same element.
The use of beams of isotopes in the simulations approximates what happens in reality. In the simulations a 'new' beam of ions is defined, while in reality these isotopes are extracted from the target. However, the difference between the two will not be very large because the fraction of nuclei that is extracted from the target is quite small.
Unfortunately, the use of beams of isotopes in the simulations poses a problem. When a beam of isotopes is defined, FLUKA uses not only particles in the ground state, but also isomers. Many of these isomers are short-lived, so in the real experiment they have long decayed before the collections happen. However, in the simulations they will have a large contribution to the dose. This needs to be taken into account. This is done by measuring the ambient dose equivalent rate 1000 s after the end of the collections instead of just after the collections. This delay was chosen such that the short-lived isomers have decayed and no longer contribute to the dose. However, the effect of the decay of the ground state nuclei will be negligible during this time, because they all have long enough half-lives. Some particles in the beam, i.e. the short-lived isomers, are now filtered out of the beam. Therefore, the beam current needs to be increased. For this we need to know what fraction of the beam consists of short-lived isomers. Unfortunately, FLUKA gives no information about how it make the distribution of the ground state and isomeric states. Therefore, this needs to be estimated. This is done by assuming that the dose rate just after the collection, D_1, is mainly coming from the short-lived isomer. Because this short-lived isomer will be completely decayed after 1000 s, the dose rate 1000 s after

the collection, D_2, comes mainly from the long-lived ground state. Since the dose rate is related to the activity, the following can be calculated.

$$\frac{D_1}{D_2} \propto \frac{A_1}{A_2} = \frac{\lambda_1 N_1}{\lambda_2 N_2} \tag{5.2}$$

The old beam current, C_{old}, only took into account the long-lived isomer, amounting to N_2. The new beam current should also include the short-lived isomer, which has an amount N_1. The adapted beam current can then be calculated from the old one as follows.

$$C_{new} = C_{old} \left(\frac{N_1}{N_2} + 1 \right) \tag{5.3}$$

This method is of course only a rough approximation. Unfortunately, it will only work for isomers with very short half-lives of the order of seconds. However, this limitation did not pose too many problems for our calculations.

5.3 Results & Discussion

5.3.1 Temperature dependence of the collection

Figure 5.2 shows the results of the target calibration, where the current applied to the target is linked to the target temperature, for a linear and a quadratic fit. The thus obtained fitting parameters are given in table 5.1. Because the uncertainties on the data points are not provided, the reduced χ^2 value cannot be calculated. However, by looking at the residuals, it can be concluded that the quadratic fit is the best.

Table 5.1: Fitting parameters for the target calibration. The fit is performed with the following function: $temperature = a \cdot current^2 + b \cdot current + c$.

	linear fit	quadratic fit
a	0	-0.003782
b	2.1645	5.7717
c	625.1890	-172.1289

During the first collection, the current on the target was increased from 470 A to 490 A, which corresponds to a temperature of about 1750 °C. For the second collection the current on the target was 630 A, corresponding to an temperature of about 1950 °C. finally for the last collection, the current was increased to 750 A, resulting in a temperature of about 2050 °C.
The analysis of the collected samples showed that in the first two batches mainly ^{139}Ce was present, in the form of ^{139}Ce^{16}O. The oxygen probably originates from traces of air or humidity left in the pores of the Ta target or from tantalum oxides present on the surface of the target. In the last batch, only ^{155}Tb was found. Note that Ce will also be extracted from the target at high temperatures. It is not found in the collected sample after the third collection because it is already fully released from the target because the target was heated to a low temperature for a long time. The results are summarised in

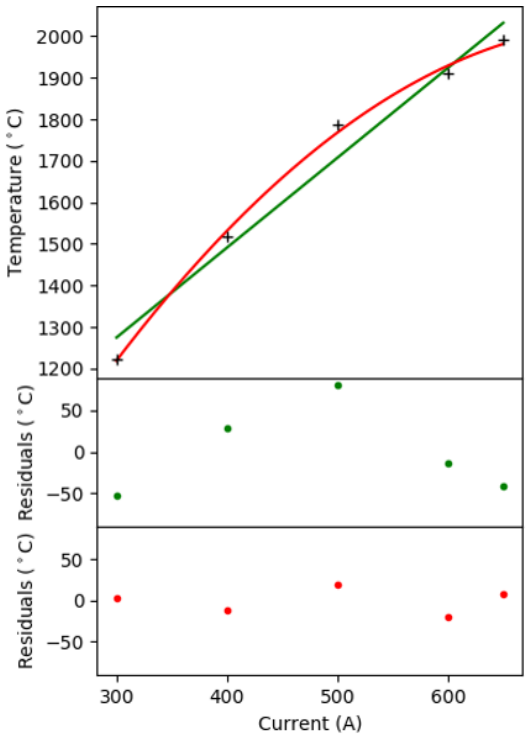

Figure 5.2: Temperature of the target in function of the current. Data is fitted with a linear (green) and a quadratic (red) curve. The bottom figures show the residuals.

Table 5.2: Effect of the target temperature on the isotope collected.

Target temperature (°C)	Collected isotope
1750	^{139}Ce
1950	^{139}Ce
2050	^{155}Tb

Table 5.2. This shows that by playing with the temperature, it is possible to first extract unwanted contaminations before collecting the wanted isotopes. This clearly shows one of the advantages of off-line facilities, having the possibility to adjust different parameters, such as temperature.

5.3.2 Ambient dose equivalent

Measurements

The data of four dose monitors are recorded during the first isotope collection at CERN-MEDICIS. The first detector, PAHIS802, is located near the target inside the bunker at a height of 175 cm. Figure 5.3 shows the output of this detector on the 7th of December 2017. At around 11h15 this graph shows a steep increase from a background value of about 0.18 μSv/h to about 500 μSv/h. This corresponds to the moment the target was placed on its location. Afterwards, an exponential decay is visible originating from the

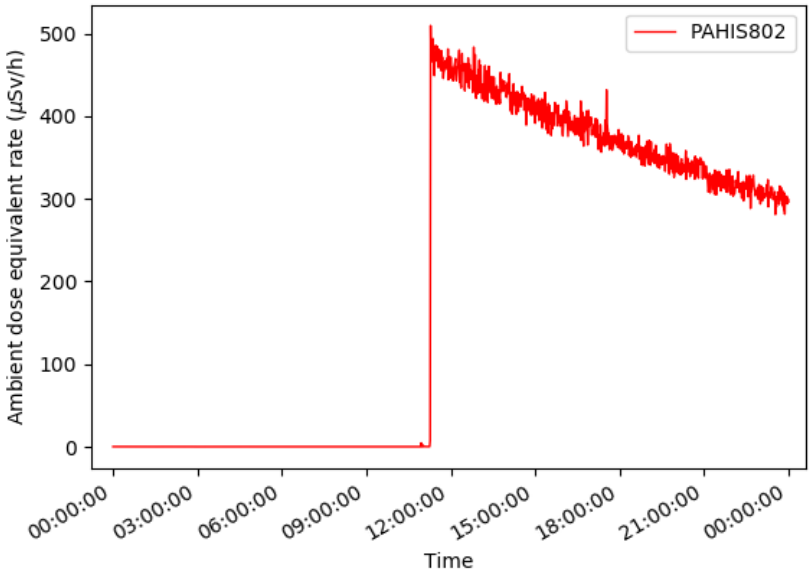

Figure 5.3: Ambient dose equivalent rate vs time measured from PAHIS802 when the target is installed.

decay of nuclei in the target. By the time the collections start, 4 days later, the ambient dose equivalent rate has dropped to about 50 μSv/h. On the other three detectors, no increase is visible due to the target installation.
The other detectors, PAGIS803, PAGIS804 and PAGIS805 are located in the experimental hall. PAGIS803 and PAGIS804 are placed against the wall at a height of 180 cm and PAGIS805 is positioned close to the collection point at a much lower height of 110 cm, corresponding to the height of the collection point. Figure 5.4 shows the ambient dose equivalent rate for these detectors on the 11th and the 12th of December 2017, when the collections took place. This figure shows that the collections did not have a measurable effect on the dose rate measured with the detectors on the wall; the same background level remains. It does however have an effect on the detector positioned near the collection point. Figure 5.5 shows the increase of the ambient dose equivalent rate due to the three collections in PAGIS805. During the first collection, the target temperature was increased; this is visible as a slightly higher increase in dose rate near the end of the collection. After this collection, a small decrease is visible. This is because at that point the sample is removed for analysis. The ambient dose equivalent rate does not drop back to the background level, because parts of the collection chamber, such as the slits, are contaminated during collection. During this collection $^{139}Ce^{16}O$ was collected. The result of the first collection is an increase in the ambient dose equivalent rate of about 0.01 μSv/h. The second collection takes place at a higher temperature than the first. Therefore, the dose rate increase is much larger here. At around 19h30, the collection stopped due to problems with the magnet. Afterwards, one would expect to see exponential decay. However, due to the long half-life of ^{139}Ce ($t_{1/2}$ = 138 d), which is collected here, the ambient equivalent dose rate stays almost constant. This collection results in an increase in the ambient dose equivalent rate of about 0.02 μSv/h. With respect to the background

level, the ambient dose equivalent rate has increased with about 0.03 μSv/h. At around 10h in the morning, the sample of the second collection is removed. This results in a small decrease of the ambient dose equivalent rate. Subsequently, the third collection is started. For this collection, the target temperature is even more increased. However, the increase in the dose rate is smaller than with the first collection. This is mainly because now all $^{139}Ce^{16}O$ has be extracted from the target and only ^{155}Tb is collected, which is harder to extract from the target. This final collection resulted in an increase in the ambient dose equivalent rate of about 0.015 μSv/h. With respect to the background level, the ambient dose equivalent rate has increased with about 0.035 μSv/h. After this collection, again the sample is removed for analysis.

Simulations

The first part of the simulations considers the irradiation of the target. Figure 5.6 shows the ambient dose equivalent rate distribution that results from the irradiated target at the time the last collection is ended. This figure shows that indeed the bunker stops most of the radiation, as is expected from the measurements.
Besides an estimate of the ambient dose equivalent rate, this simulation also provides information on the activity of the isotopes that are produced. Figure 5.7 shows the activity of the isotopes that are present in the target at the start of the first collection. This figure shows that the isotopes that are mainly produced are high in mass (A $>$ 100) and are on the neutron deficient side, as also observed experimentally and discussed in the previous chapter.

Here, we are mainly interested in the isotopes of Ce and Tb. Since these are the only ones that are collected, it is assumed that these are the only ones that are extracted from the target, which is of course an approximation. Figure 5.8 shows a detailed view of the activity of the Ce and Tb isotopes. This information is used to decide which beams need to be defined for the simulation of the collections, only isotopes with an activity higher than 10^4 Bq are included in the simulations. Isotopes with an activity lower than that will not have a significant influence on the ambient dose equivalent rate as there are isotopes with an activity of 10^8 Bq.
For the simulation of the first and the second collection, only beams of Ce are used. Actually CeO will be extracted from the target, but the oxygen is stable and will not contribute to the dose. Table 5.3 shows the activity of the different Ce isotopes at the time the first collection starts. For the second collection a similar table is made, which is not shown. For the isotopes that are included in the simulations, i.e. ^{134}Ce, ^{135}Ce, ^{137}Ce and ^{139}Ce, the absolute and relative yield are calculated. During the experiment, the beam current of the collected beam, in this case ^{139}Ce, was measured. With the relative yields, the beam current of the other isotopes can be calculated.
For the third collection, only Tb isotopes are included in the simulations. In a similar way, Table 5.4 shows the activity of the Tb isotopes at the start of the third collection and the absolute and relative yield, for those that are included in the simulations. The beam current of ^{155}Tb is measured during the experiment and the beam currents of the other Tb isotopes are calculated from the relative yields.
As explained at the end of section 5.2.2, FLUKA also includes short-lived isomers. To correct for this, the calculated beam currents are adjusted for ^{135}Ce, ^{139}Ce, ^{151}Tb and

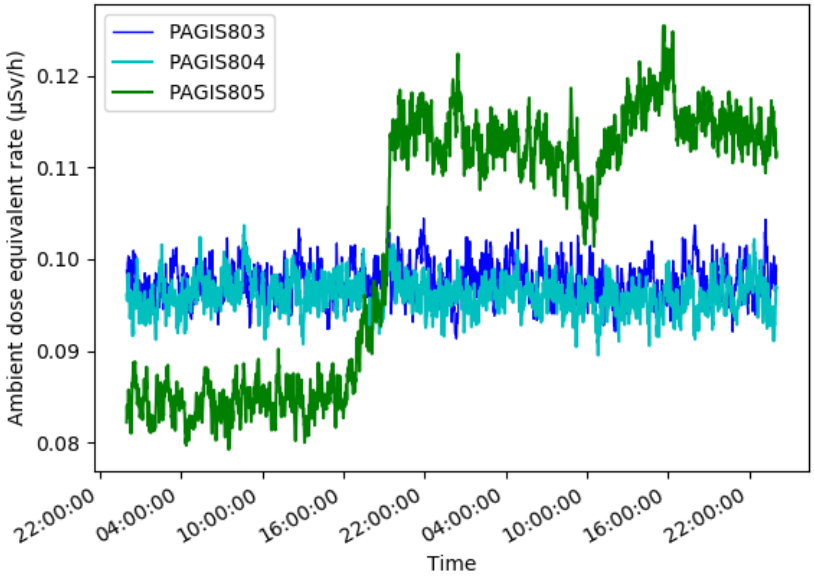

Figure 5.4: Ambient dose equivalent rate vs time measured from PAGIS803, PAGIS804 and PAGIS805 during the collections. Data is shown for the 11th and 12th of December 2017.

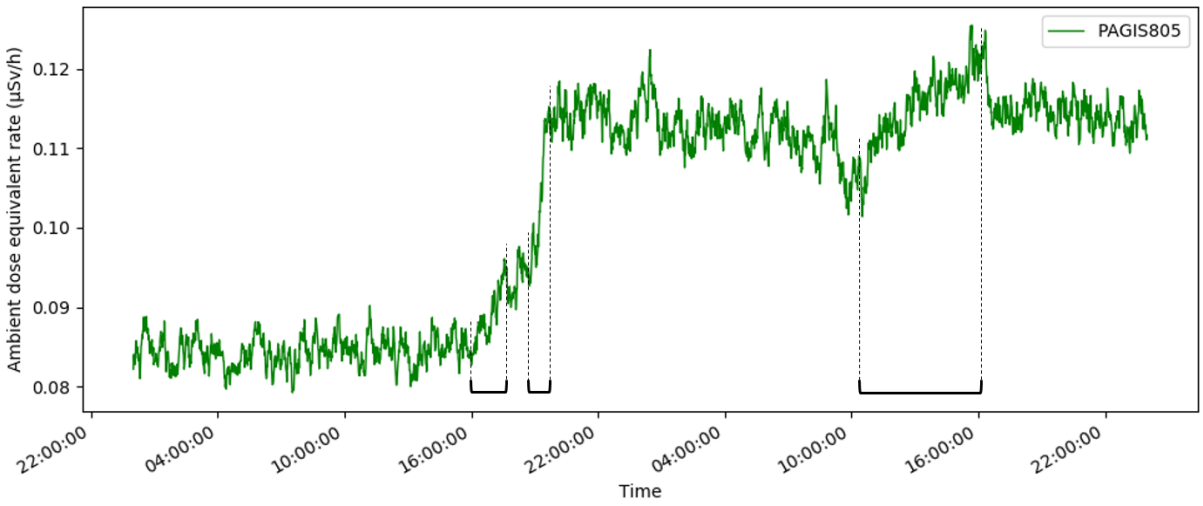

Figure 5.5: Ambient dose equivalent rate vs time measured from PAGIS805 during the three collections, which are indicated on the graph. Data is shown for the 11th and 12th of December 2017.

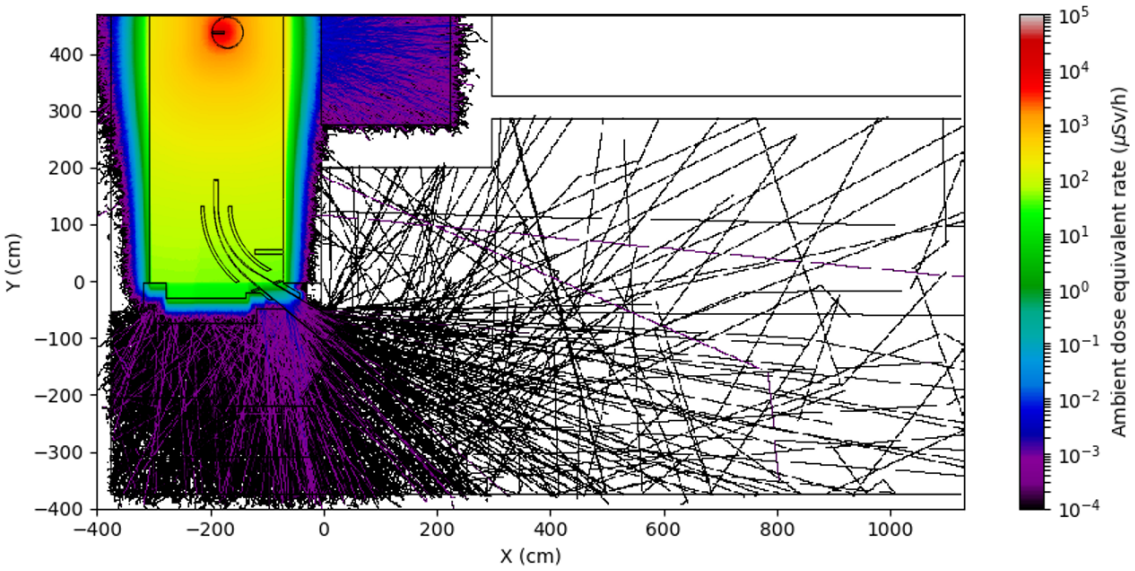

Figure 5.6: Ambient dose equivalent rate distribution due to the irradiated target, at the end of the last collection. This image shows an average over the z-direction between floor and ceiling.

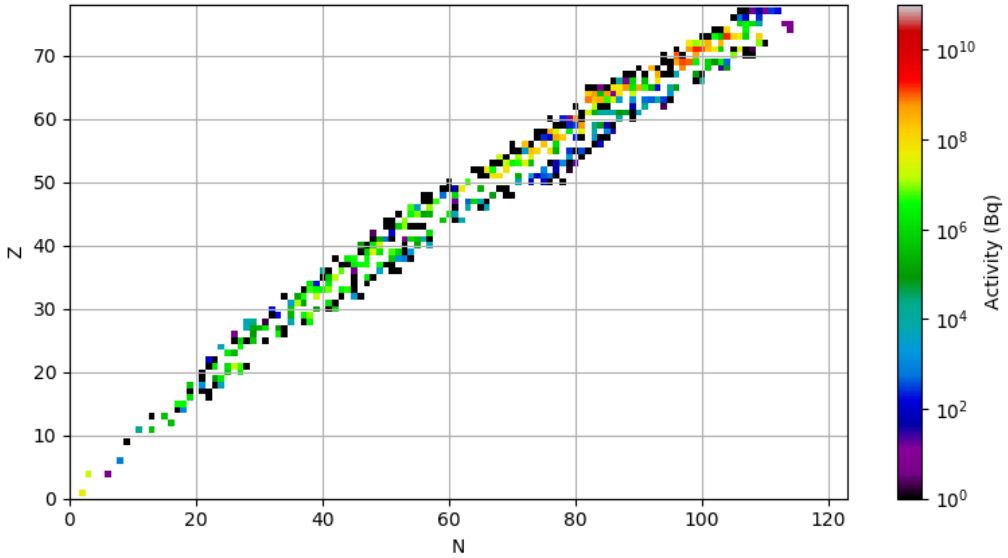

Figure 5.7: Activity of the isotopes that are present in the Ta target at the start of the first collection according to the FLUKA simulation.

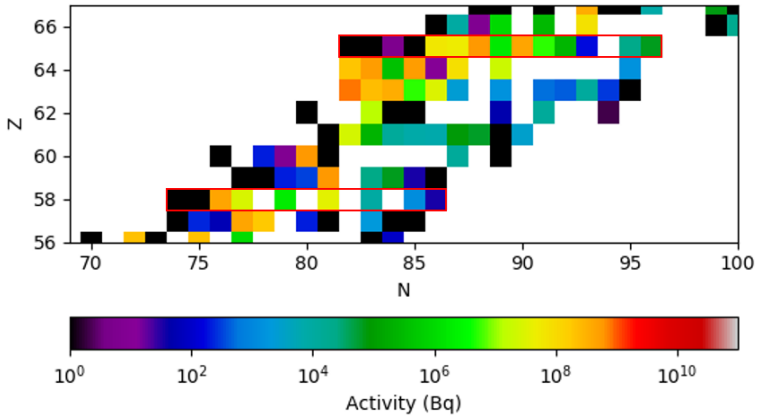

Figure 5.8: Detailed view of the activity of the isotopes that are present in the Ta target at the start of the first collection according to the FLUKA simulation. The Tb isotopes (Z=65) and the Ce isotopes (Z=58) are indicated.

Table 5.3: Activity of the Ce isotopes in the target at the beginning of the first collection according to the simulation. The absolute and relative yield are calculated for those isotopes that are included in the simulation of the collections.

Isotope	Half-life	Activity (Bq)	Absolute yield	Relative yield
^{132}Ce	3.5 h	$8.096(3)\times10^{-2}$		
^{133}Ce	97 m	$1.6331(5)\times10^{-14}$		
^{134}Ce	3.2 d	$4.359(1)\times10^{8}$	$1.7191(5)\times10^{14}$	20.42%
^{135}Ce	17.7 h	$2.9379(9)\times10^{7}$	$2.7008(8)\times10^{12}$	0.32%
^{136}Ce	stable			
^{137}Ce	9.0 h	$1.956(4)\times10^{6}$	$9.14(2)\times10^{10}$	0.01%
^{138}Ce	stable			
^{139}Ce	137.6 d	$3.885(3)\times10^{7}$	$6.666(2)\times10^{14}$	79.25%
^{140}Ce	stable			
^{141}Ce	32.5 d	$9.4(3)\times10^{3}$		
^{142}Ce	stable			
^{143}Ce	33 h	$1.3(1)\times10^{3}$		
^{144}Ce	284.9 d	37(8)		

Table 5.4: Activity of the Tb isotopes in the target at the beginning of the third collection according to the simulation. The absolute and relative yield are calculated for those isotopes that are included in the simulation of the collections.

Isotope	Half-life	Activity (Bq)	Absolute yield	Relative yield
^{147}Tb	1.7 h	$1.7686(4)\times10^{-16}$		
^{148}Tb	60 m	$3.3973(7)\times10^{-34}$		
^{149}Tb	4.2 h	$2.8750(6)\times10^{-1}$		
^{150}Tb	3.5 h	$2.3475(5)\times10^{-3}$		
^{151}Tb	17.6 h	$3.0875(5)\times10^{7}$	$2.8237(5)\times10^{12}$	0.21%
^{152}Tb	17.5 h	$2.4993(5)\times10^{7}$	2.2716×10^{12}	0.17%
^{153}Tb	2.3 d	$4.679(1)\times10^{8}$	$1.3649(3)\times10^{14}$	10.15%
^{154}Tb	21.5 h	$9.68(1)\times10^{5}$	$1.081(1)\times10^{11}$	0.01%
^{155}Tb	5.3 d	$4.3041(9)\times10^{8}$	$2.8542(6)\times10^{14}$	21.23%
^{156}Tb	5.4 d	$4.74(1)\times10^{6}$	$3.163(8)\times10^{12}$	0.24%
^{157}Tb	71 y	$2.8268(6)\times10^{5}$	$9.137(2)\times10^{14}$	67.97%
^{158}Tb	180 y	179(1)		
^{159}Tb	stable			
^{160}Tb	72.3 d	$2.22(3)\times10^{4}$	$2.00(3)\times10^{11}$	0.01%
^{161}Tb	6.9 d	$6.3(1)\times10^{4}$	$5.3(1)\times10^{10}$	0.004%

^{152}Tb, because they all have a short-lived isomer. For ^{137}Ce, ^{154}Tb and ^{156}Tb the isomers are too long-lived to correct for. Fortunately, their contribution to the dose will not be too large because the activity of these isotopes is quite small.

The effect of the collections on the ambient dose equivalent rate can now be estimated by simulating the beams of the Ce and Tb isotopes. Figures 5.9 and 5.10 show the beam paths of the different Ce and Tb isotopes, respectively. Only ^{139}Ce and ^{155}Tb reach the collection point, the other isotopes are deposited on the slits. Figure 5.11 shows the combined ambient dose equivalent rate distribution due to all collections at the end of the last collection. This shows that the collections are by far the largest contribution to the dose in the experimental hall. In future experiments, extra shielding will be placed around the collection point. This should strongly reduce the dose due to the collections.

The results from the simulations of the irradiated target and the collections, can now be combined. Figure 5.12 shows the total effect on the ambient dose equivalent rate of the irradiated target and the collection of isotopes.
As explained before, the ambient dose equivalent rate is also estimated by the simulations at the locations of the 4 detectors, at different points in time. These results are shown in Table 5.5 with a statistical uncertainty. In the experiment, the collection sample is removed after each collection. In the simulation, this is included by only including the dose due to the collected isotope at the time of that collection and removing it later. For example the dose due to the first ^{139}Ce beam is only included at the end of the first collection and not at the end of the second and third collection, because all ^{139}Ce isotopes should be removed when the sample is removed after the collection. However, it is unlikely that all ^{139}Ce or ^{155}Tb isotopes hit the sample. Probably some of them also end up on the slits and are not removed when the sample is removed. Therefore, the ambient dose

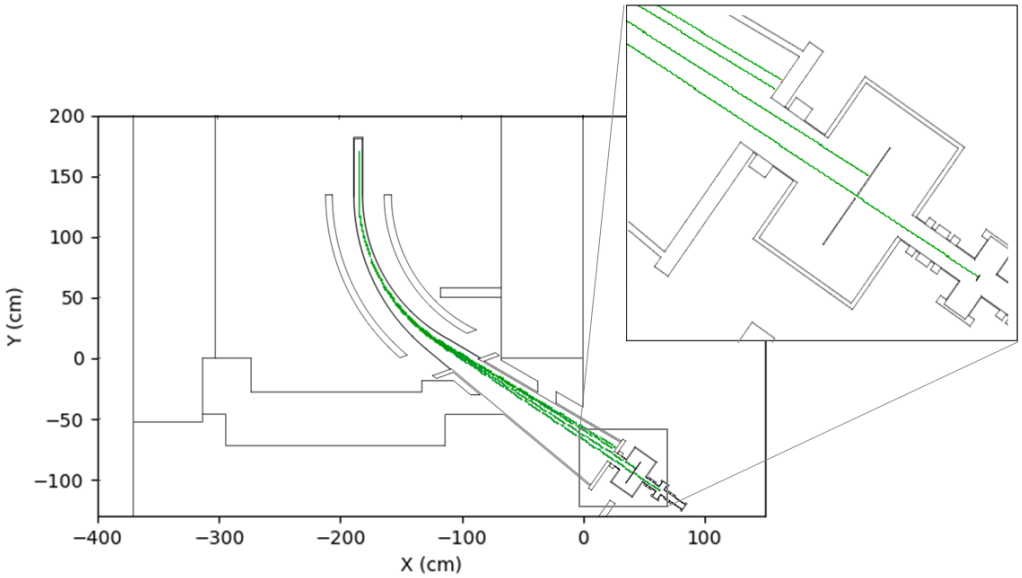

Figure 5.9: The beam paths of the different Ce isotopes used in the simulation are shown in green. The beams correspond to ^{139}Ce, ^{137}Ce, ^{135}Ce and ^{134}Ce from left to right. Only ^{139}Ce reaches the collection point.

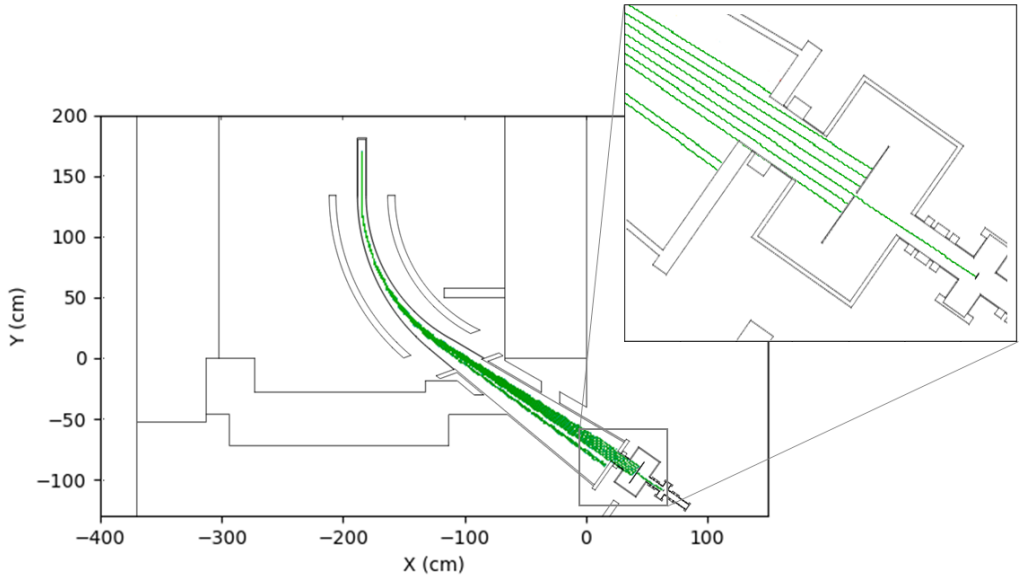

Figure 5.10: The beam paths of the different Ce isotopes used in the simulation are shown in green. The beams correspond to ^{161}Tb, ^{160}Tb, ^{157}Tb, ^{156}Tb, ^{155}Tb, ^{154}Tb, ^{153}Tb, ^{152}Tb and ^{151}Tb from left to right. Only ^{155}Tb reaches the collection point.

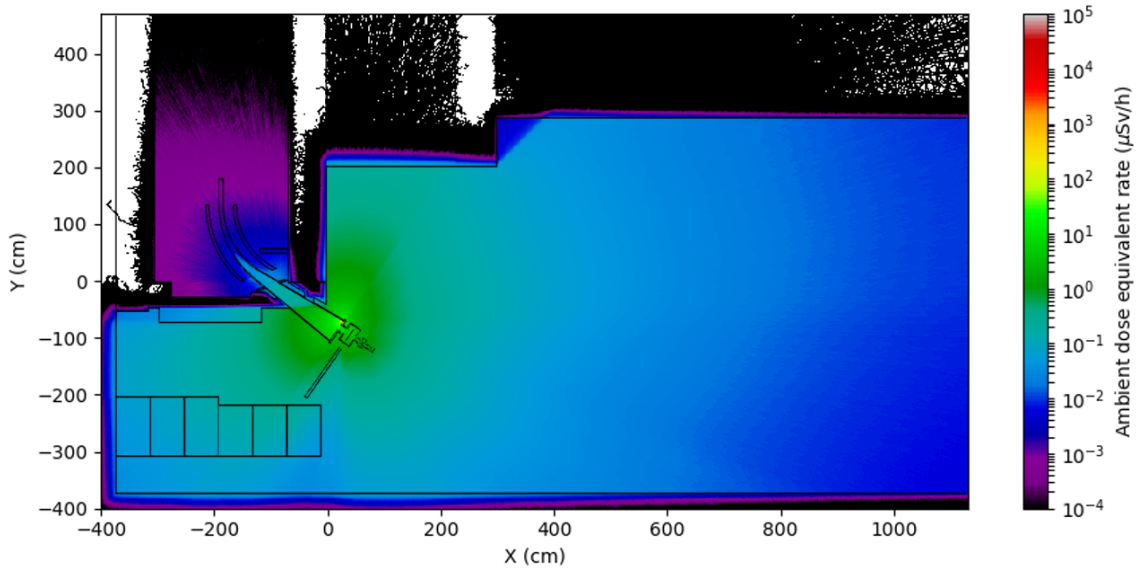

Figure 5.11: Ambient dose equivalent rate distribution due to the collections, at the end of the last collection. This image shows an average over the z-direction between floor and ceiling.

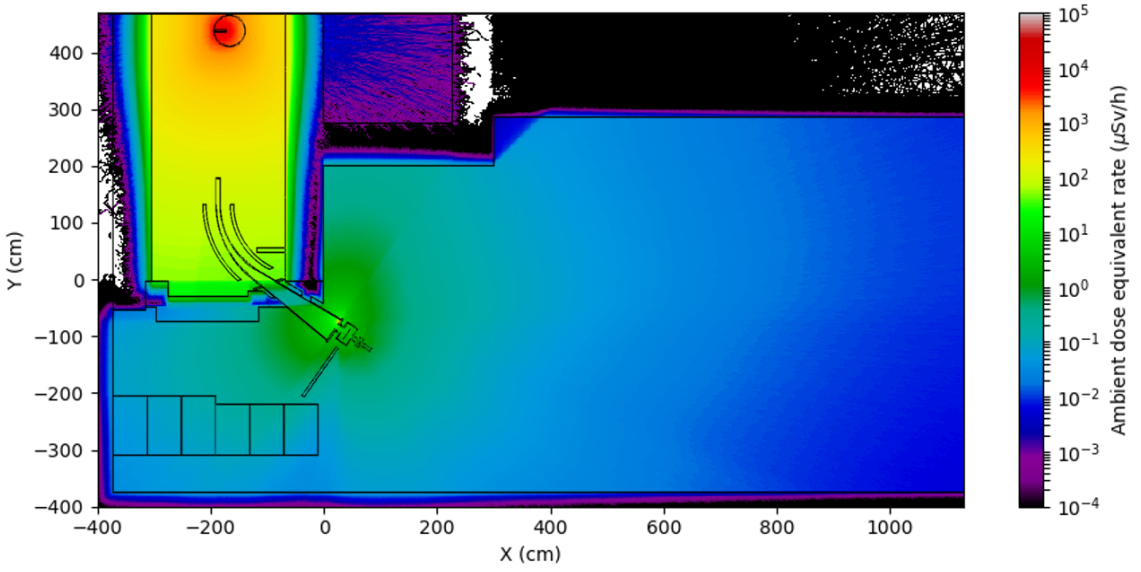

Figure 5.12: Ambient dose equivalent rate distribution due to the irradiated target and the collections, at the end of the last collection. This image shows an average over the z-direction between floor and ceiling.

equivalent rate is also calculated without taking the sample removal into account. The real value probably lies somewhere between the two.

Table 5.5: Ambient dose equivalent rate (μSv/h) in the different detectors, according to the simulations. In the first part of the table the removal of the sample is included, in the second part not.

	PAHIS802	PAGIS803	PAGIS804	PAGIS805
end first collection	$5.7(2.8)\times10^2$	0.000082(11)	0.00088(4)	0.00452(12)
end second collection	$5.6(2.7)\times10^2$	0.0061(9)	0.065(4)	0.342(10)
end third collection	$4.4(2.1)\times10^2$	0.0057(8)	0.0586(31)	0.277(9)

(a) Sample removal included

	PAHIS802	PAGIS803	PAGIS804	PAGIS805
end first collection	$5.7(2.8)\times10^2$	0.000082(11)	0.00088(4)	0.00452(12)
end second collection	$5.6(2.7)\times10^2$	0.0061(9)	0.065(4)	0.343(10)
end third collection	$4.4(2.1)\times10^2$	0.0060(8)	0.0646(31)	0.384(9)

(b) Sample removal not included

The results of this simulation can now be compared with the measurements. First, this simulation shows that, within error bars, the irradiated target has no effect on the ambient dose equivalent rate in detectors PAGIS803, PAGIS804 and PAGIS805 and the collections have no effect on the ambient dose equivalent rate in detector PAHIS802 (this is not shown in Table 5.5). This corresponds with what is seen in the measurements.
Table 5.5 shows that at the end of the first collection, the ambient dose equivalent rate in PAHIS802 is of the order of 500 μSv/h. This is 10 times higher than what is seen in the measurements. This is possibly because in reality the target is placed in a steal capsule, which is not yet included in the simulation. This extra shielding can strongly reduce the dose. Moreover, as soon as the target is heated, volatile substances will escape the target. This can reduce the dose in PAHIS802 since it is positioned very close to the target. One can see that there is no difference between whether or not the sample removal is included in results for PAHIS802, which is logical since the collections have no effect on the ambient dose equivalent rates measured with this detector.
For PAGIS803 and PAGIS804 the measurement do not show an increase in the ambient dose equivalent rate due to the collections. However, the simulation suggests that certainly the second collection should result in an visible increase in ambient dose equivalent rate on both detectors. It seems that the simulation overestimates the effect of the second collection.
Similar things are seen for PAGIS805. The simulation estimates that the ambient dose equivalent rate increases by about 0.005 μSv/h due to the first collection. This is 2 times less than what the measurements show. A possible explanation for this is that in the simulations only the Ce isotopes are taken into account, while in reality also other isotopes will be extracted from the target and ionised. Depending on their mass, these isotopes will be deposited on the wall of the magnet or on the slits, where they can contribute to the dose. The simulation correctly shows that the effect of the removal of the sample after the first collection is small. For the second collections, the simulation estimates that the ambient dose equivalent rate has increased to about 0.3 μSv/h. This is 10 times more than the 0.03 μSv/h the measurement shows. The origin of this discrepancy is not

entirely clear. Inaccuracies in the duration of the collection would probably not result in such a large difference. If the composition of the beams would be responsible, probably a similar effect would be present after the first collection. According to the logbook, some beam tuning was done during the second collection. Therefore, the beam current, that is mentioned in the logbook and used in the simulation, is probably the maximum beam current that is reached during this collection. If the average beam current is much smaller than this, this can possibly explain why the simulations overestimate the dose. When looking at the results with the removal of the sample included, one can see that the ambient dose equivalent rate after the third collection is smaller than after the second collection. This indicates that according to the simulations the dose is more reduced by the removal of the sample and the decay between the second and third collection, than that it is increased by the third collection. This is logical if the dose due to the second collection is overestimated by a factor 10. The results where the sample removal is not included show that due to the third collection, the ambient dose equivalent increases by about 0.04 μSv/h, whereas the measurement showed an increase of 0.015 μSv/h. This can again be explained by the fact that the simulation only takes the Tb isotopes into account, while probably other isotopes contribute to the dose.

The comparison between simulations and measurements shows that these kind of simulations can be used to make rough estimates of the expected dose rates. Moreover, they can be used to point out the main sources contributing to the dose and to identify for example places where extra shielding is needed. Quantitative results should however not be trusted too much and should be handled with care.

6 | Conclusions & Outlook

This work looked at two methods to optimise the production of neutron deficient Tb isotopes, especially ^{155}Tb, by proton-induced spallation reactions in Ta targets for medical research applications. In the first part, the energy dependence of the production of longer-lived contaminants was analysed by measuring cumulative cross sections. This showed that the cross section for the production of ^{139}Ce, which is often present as a contaminant under the form of ^{139}Ce^{16}O during the collection of ^{155}Tb, reaches a maximal value at a proton energy well above 1000 MeV. From literature it is known that for the production of ^{155}Tb a maximal cross section is reached at around 800 MeV. Therefore, it is beneficial to use protons with an energy of 800 MeV or less for the production of ^{155}Tb by proton induced spallation of Ta in order to minimise the contamination with ^{139}Ce^{16}O. Accordingly, ISOL@MYRRHA at SCK•CEN in Mol, which will operate at 600 MeV, will be nearly ideal for the production of ^{155}Tb.
Besides the results from the γ-analysis, new data on the cumulative cross section of ^{149}Tb was presented here. The main goal of this was to solve the discrepancy between different literature values. The results presented here, showed that the literature values of Winsberg [1] and Miranov [2] are preferred.

Some improvements can be made to the analysis that was performed here. Because the uncertainty on the count rates turned out to be the largest contribution to the uncertainty on the cumulative cross sections, it might be interesting in the future to measure the spectra for a longer time or to use thicker foils, to increase the statistics. It would also be interesting to do an in depth analysis of the efficiency of the detector setup used to measure the Ta foils. Ideally, the efficiency should be measured with low activity sources, to avoid dead time problems and with sources that only emit a small number of γ-rays, to minimise summing effects. Furthermore, the efficiency of the detectors that were used to measure the Al foils, should be reanalysed. From this work, it is expected that the efficiency of the detector, that was used to measure the foil irradiated with 900 MeV protons, is not correct. Finally, the results obtained here should be compared with the results of the other analyses of the same experiment: data collected from thicker Ta foils at a close time after the experiment are still under analysis, together with the Al foils.

The second part of this work focused on the first isotope production from CERN-MEDICIS, where ^{155}Tb was collected after the irradiation of a Ta target with protons. This showed a second method to optimise the production of ^{155}Tb, namely by selecting the correct temperature for the extraction of isotopes from the target. At temperatures below 2000 °C, ^{139}Ce can be extracted in the form of ^{139}Ce^{16}O, while a temperature above 2000 °C is needed to extract ^{155}Tb. Heating the target to a lower temperature can thus be used to

eliminate contaminants before collecting ^{155}Tb. Note however that such target conditioning becomes more difficult for isotopes with shorter half-lives, such as ^{149}Tb, where the whole process much be accomplished much faster.
This experiment was also used to compare ambient dose equivalent rates estimated by FLUKA simulations, with measured rates. The results showed that these kinds of simulations can be used to make rough estimates of the expected dose rates. However, quantitative results should be handled with care. The collection that was done here, was only a small one. It would be interesting to redo the comparison between measurements and simulations for a larger collection, such as those performed in the course of 2018.

Appendices

A | Background spectrum

The background γ-ray energy spectrum that was measured for the analysis of the Ta foils is shown in the figure below. For some of the most prominent peaks, the origin is indicated.

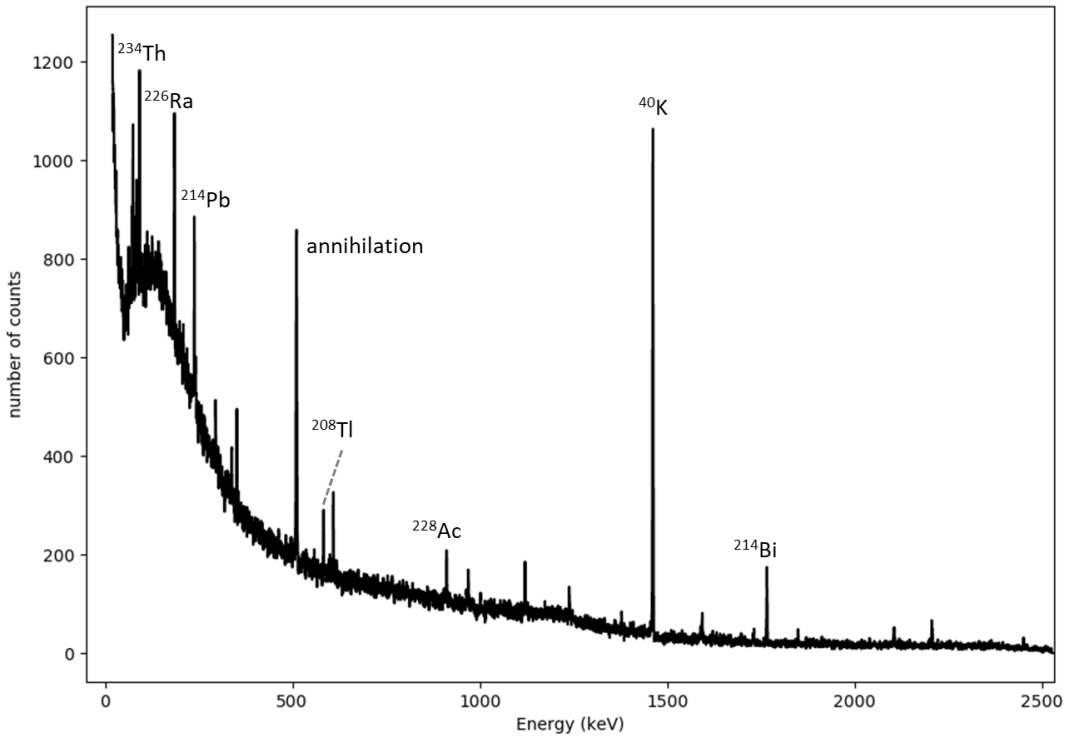

Figure A.1: Background spectrum with the origin of some of the most prominent peaks. The measurement time is 427 130 s ($\sim$ 5 d).

B | Example spectrum

Figure B.1 shows an example of a γ-ray energy spectrum that was measured for one of the Ta foils. For some of the most prominent peaks, the origin is indicated. In Figure B.2 part of this spectrum is shown with the fit.

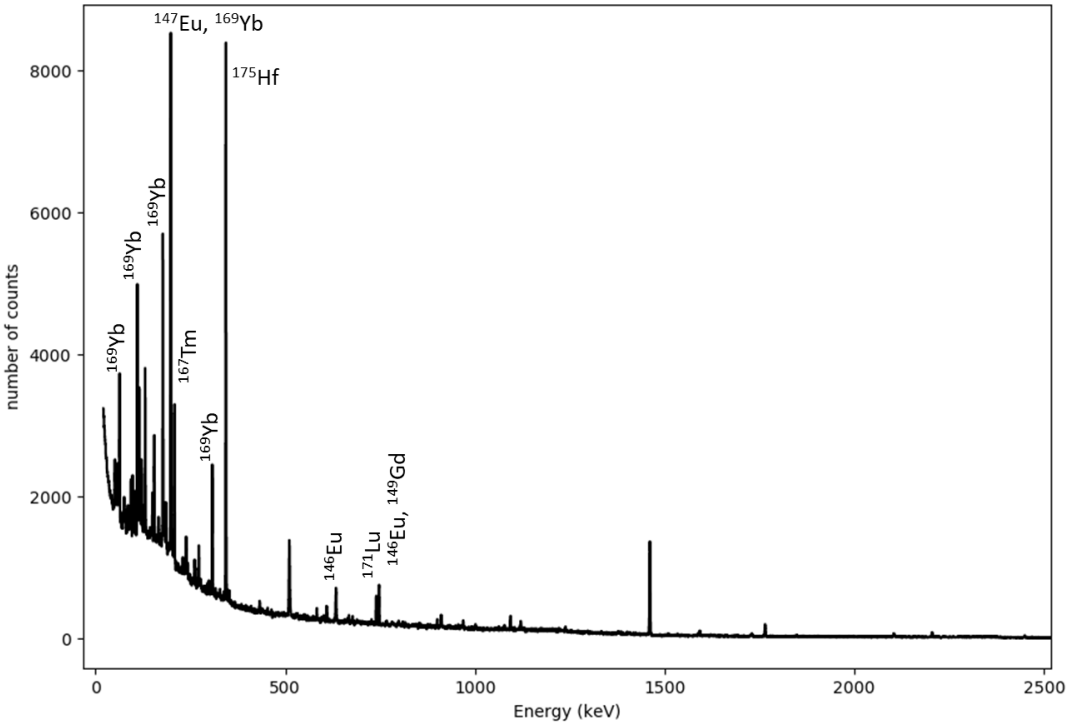

Figure B.1: Example of a spectrum of one of the Ta foils. This foil was irradiated with 600 MeV protons and was measured for 354 483 s ($\sim$ 4 d), about 50 d after the irradiation.

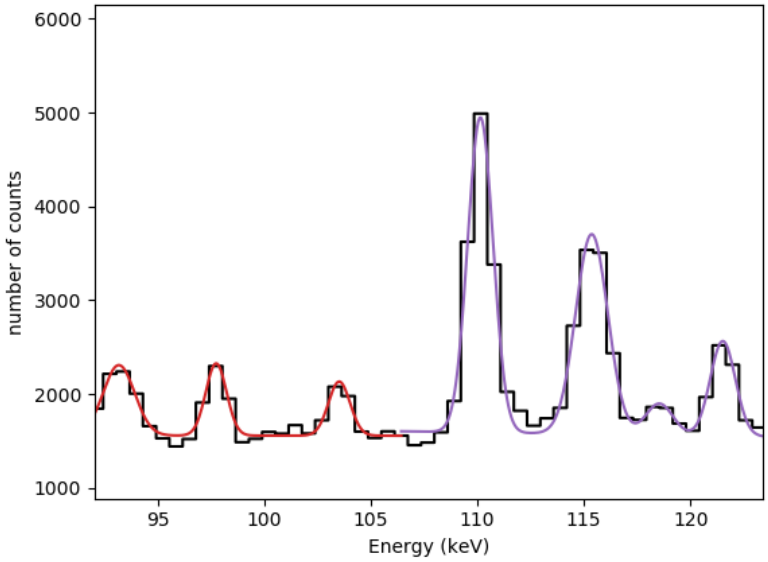

Figure B.2: Part of the spectrum of Figure B.1, with the peaks fitted with a Gaussian curve.

C | Cumulative cross sections

The following figures show the cumulative cross sections as a function of energy for the ^{175}Hf, ^{173}Lu, ^{172}Hf, ^{171}Lu, ^{167}Tm, ^{151}Gd, ^{149}Gd, ^{147}Eu, ^{146}Gd, ^{143}Pm, ^{127}Xe, ^{121}Te, ^{113}Sn and ^{105}Ag and compares these with their literature values.

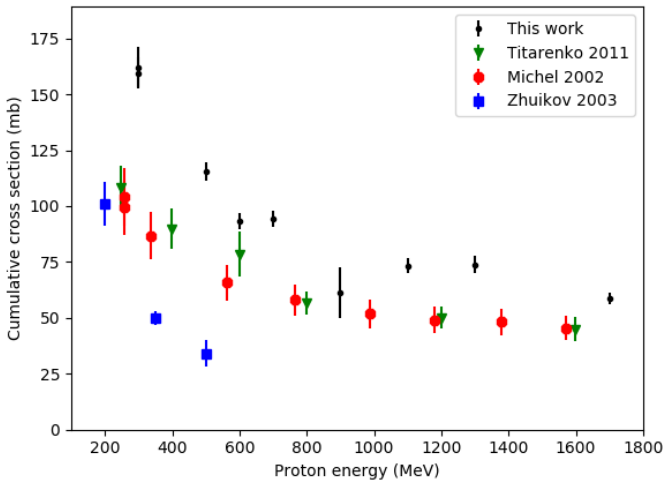

Figure C.1: Cumulative cross section as a function of incident proton energy for ^{175}Hf [46, 47, 52].

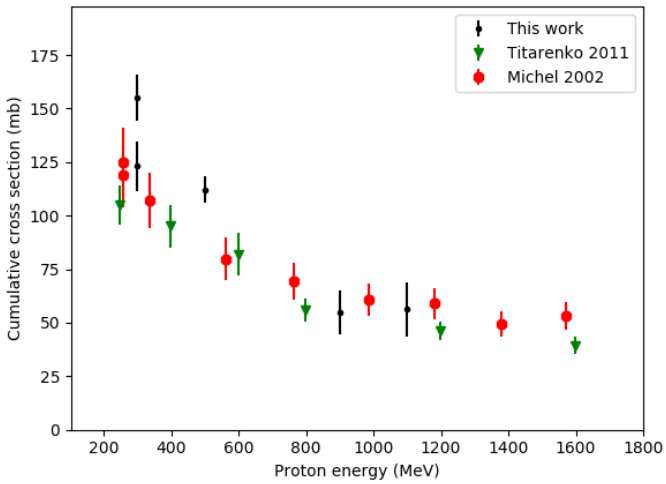

Figure C.2: Cumulative cross section as a function of incident proton energy for ^{173}Lu [46, 47].

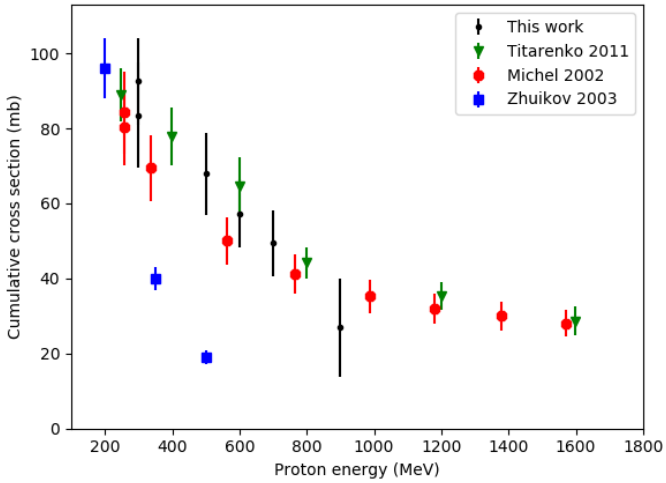

Figure C.3: Cumulative cross section as a function of incident proton energy for ^{172}Hf [46, 47, 52].

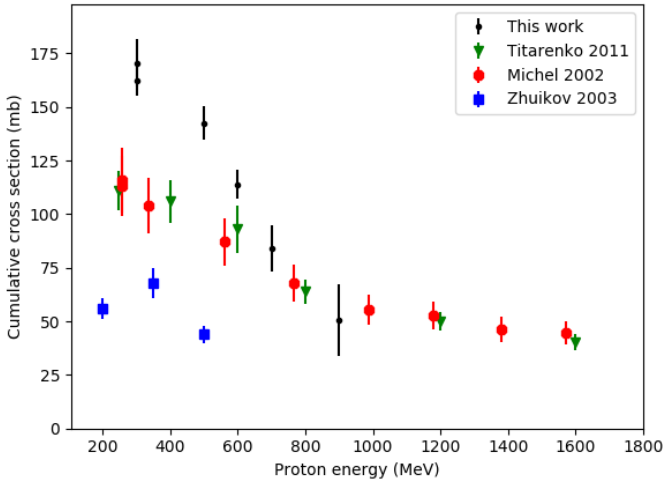

Figure C.4: Cumulative cross section as a function of incident proton energy for ^{171}Lu [46, 47].

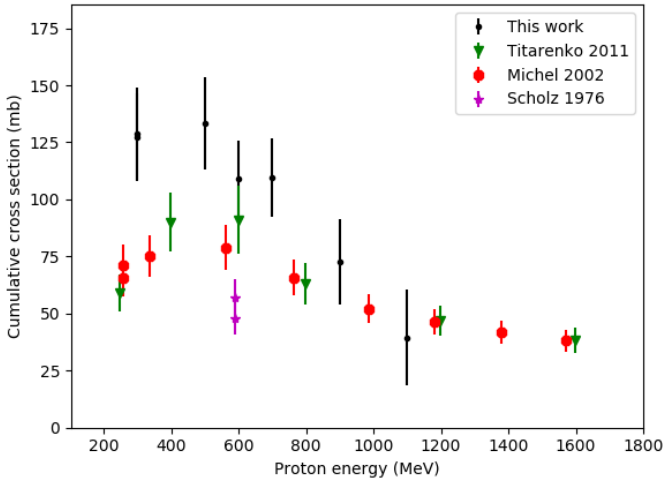

Figure C.5: Cumulative cross section as a function of incident proton energy for ^{167}Tm [46, 47, 53].

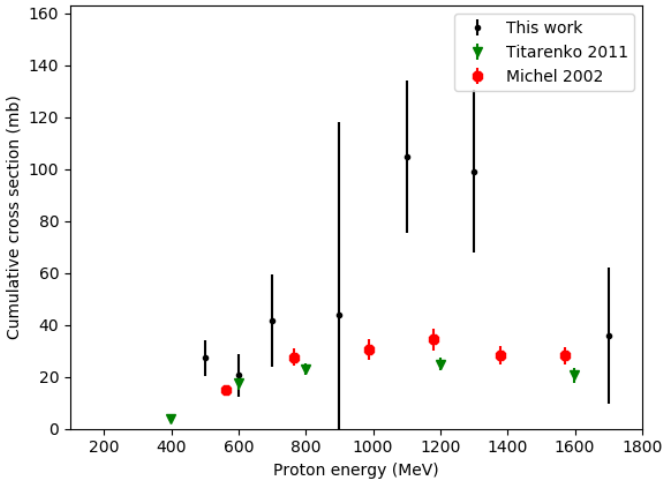

Figure C.6: Cumulative cross section as a function of incident proton energy for ^{151}Gd [46, 47].

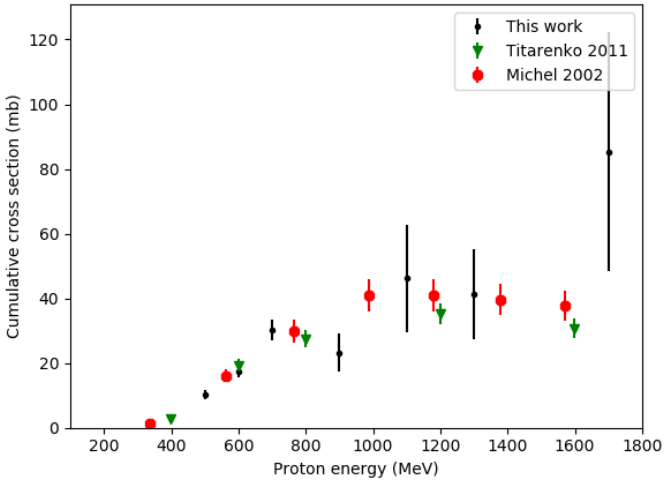

Figure C.7: Cumulative cross section as a function of incident proton energy for ^{149}Gd [46, 47].

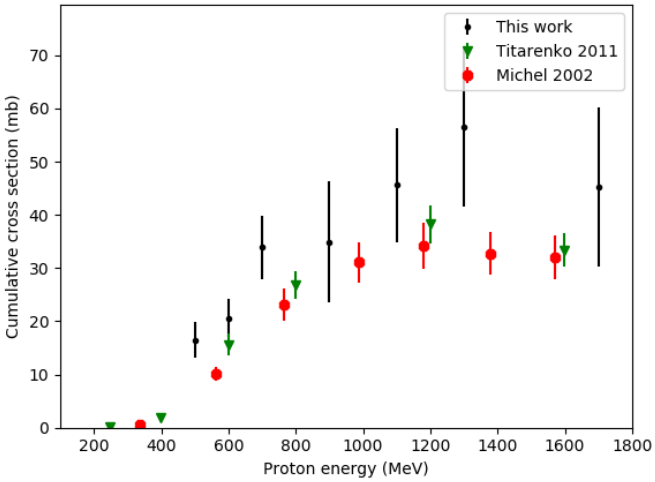

Figure C.8: Cumulative cross section as a function of incident proton energy for ^{147}Eu [46, 47].

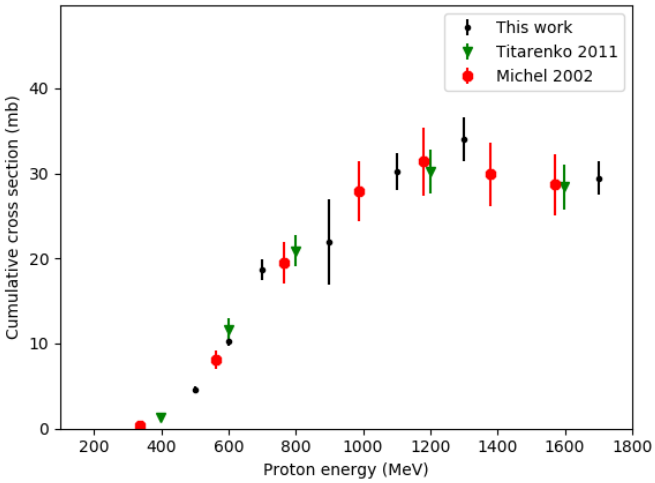

Figure C.9: Cumulative cross section as a function of incident proton energy for ^{146}Gd [46, 47].

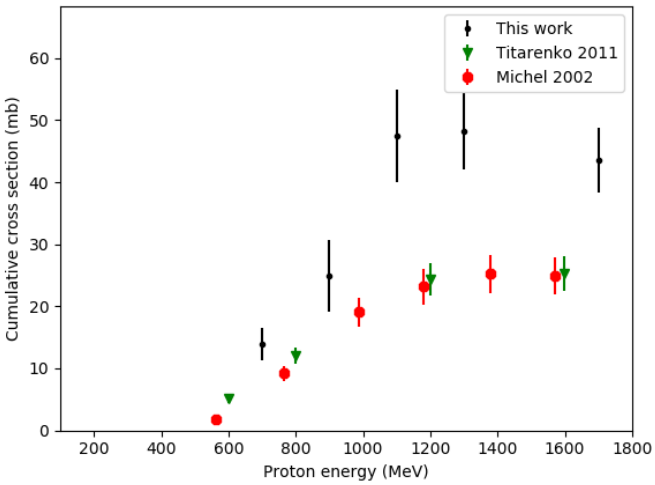

Figure C.10: Cumulative cross section as a function of incident proton energy for ^{143}Pm [46, 47].

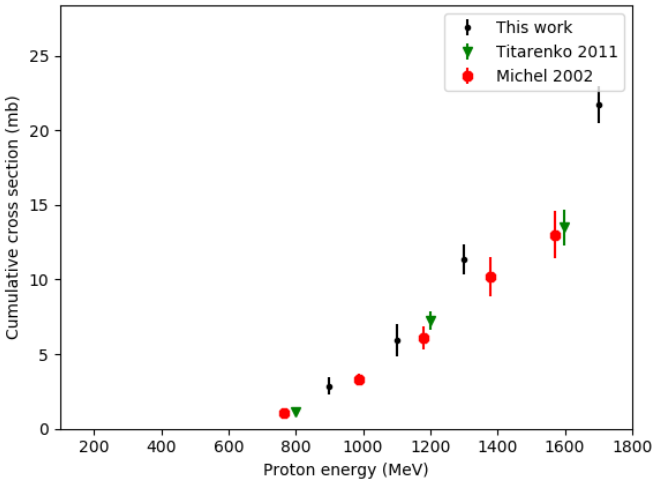

Figure C.11: Cumulative cross section as a function of incident proton energy for ^{127}Xe [46, 47].

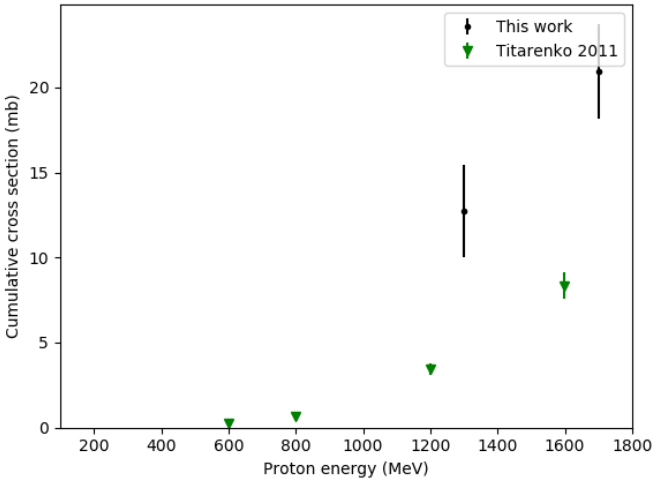

Figure C.12: Cumulative cross section as a function of incident proton energy for ^{121}Te [46].

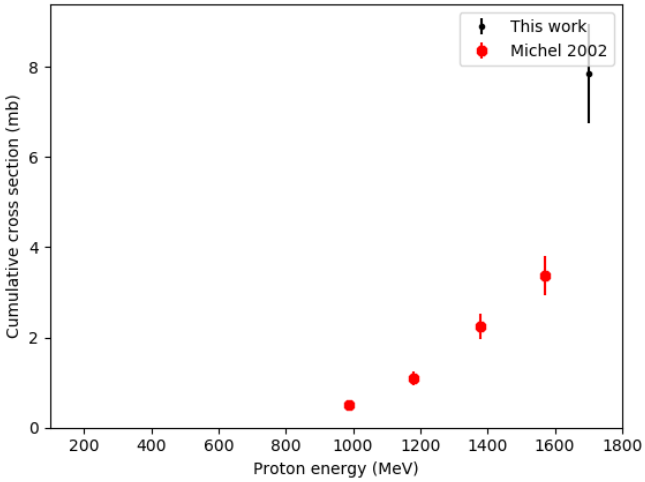

Figure C.13: Cumulative cross section as a function of incident proton energy for ^{113}Sn [47].

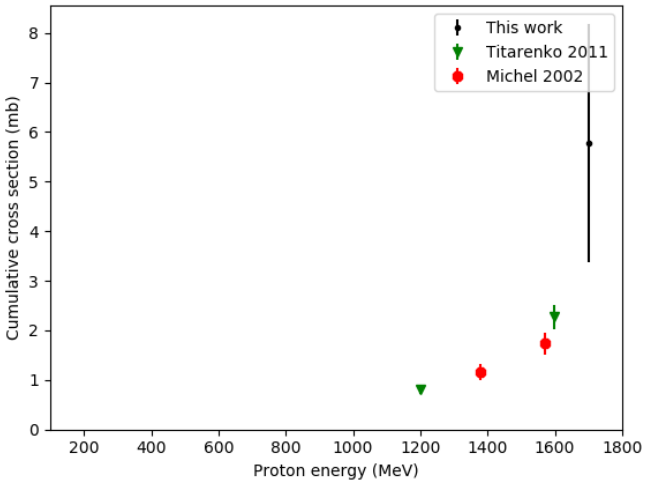

Figure C.14: Cumulative cross section as a function of incident proton energy for ^{105}Ag [46, 47].

Bibliography

[1] L. Winsberg. Recoil studies of nuclear reactions induced by high- energy particles. I. Production of Tb-149. *Physical Review*, 135:B1105, 1964.

[2] Yu.T. Mironov. Features of investigation excitation function of nuclear reactions on internal beam synchrocyclotron PIYaPh. *Conference on Nuclear Spectroscopy and Nuclear Structure*, page 276, 2001.

[3] S.M. Seidlin, L.D. Martinelli, and E. Oshry. Radioactive iodine therapy: Effect on functioning metastases of adenocarcinoma of the thyroid. *Journal of the American Medical Association*, 132.14:838–847, 1946.

[4] C. Müller et al. A unique matched quadruplet of terbium radioisotopes for PET and SPECT and for α- and β^--radionuclide therapy: An in vivo proof-of-concept study with a new receptor-targeted folate derivative. *Journal of Nuclear Medicine*, 53:1951–1959, 2012.

[5] J. Nuyts. Lecture notes: Nuclear medicine technology and techniques, 2017.

[6] G.F. Knoll. *Radiation Detection and Measurement.* John Wiley & Sons, fourth edition, 2010.

[7] T.L. Alford, L.C. Feldman, and J.W. Mayer. *Fundamentals of Nanoscale Film Analysis.* Springer, 2007.

[8] K.S. Krane. *Introductory Nuclear Physics.* John Wiley & Sons, 1988.

[9] F.F. Knapp and A. Dash. *Radiopharmaceuticals for Therapy.* Springer, 2016.

[10] Wikipedia. Stopping power (particle radiation). `https://en.wikipedia.org/wiki/Stopping_power_(particle_radiation)`. [last visited on 30/06/2018].

[11] R. Bogaerts. Lecture notes: Radiation protection, 2016.

[12] E.B. Podgoršak. *Radiation Physics for Medical Physicists.* Springer, third edition, 2016.

[13] N. Severijns. Lecture notes: Ionizing radiation detection techniques, 2017.

[14] H. Cember. *Introduction to Health Physics.* McGraw-Hill, third edition, 1996.

[15] Duke University Medical Center. What is cancer? `https://sites.duke.edu/missiontomars/the-mission/cancer/what-is-cancer/`. [last visited on 13/04/2018].

[16] International Commission on Radiological Protection. Nonstochastic effects of ionizing radiation. ICRP publication 41. *Ann. ICRP 14 (3)*, 1989.

[17] S. Mattsson and M. Söderberg. Dose quantities and units for radiation protection. In S. Mattsson and C. Hoeschen, editors, *Radiation Protection in Nuclear Medicine*, chapter 2, pages 7–18. Springer-Verlag, Berlin, Heidelberg, 2013.

[18] International Commission on Radiological Protection. The 2007 recommendations of the international commission on radiological protection. ICRP publication 103. *Ann. ICRP 37 (2-4)*, 2007.

[19] U. Köster et al. Experiment proposal to the COSY facility, defended in 2017.

[20] K. Goffin. Lecture notes: Technologie en technieken in de nucleaire geneeskunde, 2017.

[21] T. Cardinaels. Lecture notes: Nuclear and radiochemistry, 2018.

[22] C. Müller et al. Alpha-pet with terbium-149: evidence and perspectives for radiotheragnostics. *EJNMMI Radiopharmacy and Chemistry*, 1, 2017.

[23] Nucleonica. `https://nucleonica.com`. [last visited on 27/06/2018].

[24] S.Y.F. Chu, L.P. Ekström, and R.B. Firestone. The lund/LBNL nuclear data search. `http://nucleardata.nuclear.lu.se/toi/index.asp`, 1999. [last visited on 09/08/2018].

[25] S. Lehenberger et al. The low-energy β^- and electron emitter ^{161}Tb as an alternative to ^{177}Lu for targeted radionuclide therapy. *Nuclear Medicine and Biology*, 38:917–924, 2011.

[26] C. Vermeulen et al. Cross sections of proton-induced reactions on ^{nat}Gd with special emphasis on the production possibilities of ^{152}Tb and ^{155}Tb. *Nuclear Instruments and Methods in Physics Research, Section B: Beam Interactions with Materials and Atoms*, 275:24–32, 2012.

[27] P. Van Duppen. Isotope separation on line and post acceleration. In J. Al-Khalili and E. Roeckl, editors, *The Euroschool Lectures on Physics With Exotic Beams, Vol. II*, chapter 2, pages 37–77. Springer, Berlin, Heidelberg, 2006.

[28] R. Raabe. Making radioactive ion beams - detecting reaction products. *The European Physical Journal Plus*, 131:362, 2016.

[29] C. Müller et al. Future prospects for SPECT imaging using the radiolanthanide terbium-155 - production and preclinical evaluation in tumor-bearing mice. *Nuclear Medicine and Biology*, 41:Suppl:e58–65, 2014.

[30] R.M. dos Santos Augusto et al. CERN-MEDICIS (medical isotopes collected from ISOLDE): a new facility. *Applied science*, 4:265–281, 2014.

[31] J.M. Miller and J. Hudis. High-energy nuclear reactions. *Annual Review on Nuclear Science*, 9:159–202, 1959.

[32] J. Benlluire. Spallation reactions in applied and fundamental research. In J. Al-Khalili and E. Roeckl, editors, *The Euroschool Lectures on Physics With Exotic Beams, Vol. II*, chapter 5, pages 191–238. Springer, Berlin, Heidelberg, 2006.

[33] G.J. Russell. Spallation physics - an overview. *International Collaboration on Advanced Neutron Sources*, pages 22–26, 1990.

[34] J. Zeman. *Reactor Physics I.* CVUT, 2003.

[35] P. Armbruster et al. Measurement of a complete set of nuclides, cross sections, and kinetic energies in spallation of ^{238}U 1A GeV with protons. *Physical Review Letters*, 93:212701, 2004.

[36] T.T. Böhlen et al. The FLUKA code: Developments and challenges for high energy and medical applications. *Nuclear Data Sheets*, 120:211–214, 2014.

[37] A. Ferrari et al. FLUKA: A multi-particle transport code. *CERN*, 2005.

[38] M. Pelliccioni. Overview of fluence-to-effective dose and fluence-to-ambient dose equivalent conversion coefficients for high energy radiation calculated using the FLUKA code. *Radiation Protection Dosimetry*, 88:279–297, 2000.

[39] Jülich Forschungszentrum. COSY - the accelerator in Jülich. `http://www.fz-juelich.de/ikp/ikp-4/EN/Forschung_2/Beschleuniger/_node.html`. [last visited on 29/06/2018].

[40] Laboratoire National Henri Becquerel. Recomanded data. `http://www.nucleide.org/DDEP_WG/DDEPdata.htm`. [last visited on 05/04/2018].

[41] Brookhaven National Laboratory. National nuclear data center. `http://www.nndc.bnl.gov/index.jsp`. [last visited on 06/04/2018].

[42] W. Gins et al. Analysis of counting data: Development of the SATLAS python package. *Computer Physics Communications*, 222:286 – 294, 2018.

[43] T.E. Cocolios. Lecture notes: Artificial radioactivity, 2018.

[44] International Union of Pure and Applied Chemistry. Commission on isotopic abundances and atomic weights. `http://ciaaw.org/`. [last visited on 08/05/2018].

[45] Yu.V. Aleksandrov et al. (p,x) reactions cross sections on aluminum at intermediate energy of protons. *Conference on Nuclear Spectroscopy and Nuclear Structure*, page 223, 1996.

[46] Yu.E. Titarenko et al. Measurement and simulation of the cross sections for nuclide production in ^{nat}W and ^{181}Ta targets irradiated with 0.04- to 2.6-GeV protons. *Physics of Atomic Nuclei*, 74:551–572, 2011.

[47] R. Michel et al. Cross sections for the production of radionuclides by proton-induced reactions on W, Ta, Pb and Bi from thresholds up to 2.6 GeV. *Journal of Nuclear Science and Technology*, 39:242–245, 2002.

[48] SCK•CEN. ISOL@MYRRHA: Fundamental physics at MYRRHA. `http://isolmyrrha.sckcen.be/`. [last visited on 13/08/2018].

[49] T.E. Cocolios for the MEDICIS Collaboration. Presentation: Radioisotopes for medicine: First collection at CERN MEDICIS. EURORIB 2018, Giens, France, 2018.

[50] U. Köster et al. (Im-)possible ISOL beams. *The European Physical Journal Special Topics*, 150:285–291, 2007.

[51] B. Dewit. Towards the first collection of ^{44}Sc at CERN MEDICIS - Realistic FLUKA simulations of the CERN MEDICIS collection of ^{44}Sc. Master's thesis, KULeuven, 2017.

[52] B.L. Zhuikov et al. Production of high-spin isomers in proton induced reactions at 100-500 MeV on ^{181}Ta. *Physical Review C*, 68, 2003.

[53] K.L. Scholz, V.J. Sodd, and J.W. Blue. Production of thulium- 167 for medical use by irradiation of lutetium, hafnium, tantalum and tungsten with 590-MeV protons. *The International Journal of Applied Radiation and Isotopes*, 27:263–266, 1976.

DEPARTEMENT NATUURKUNDE EN STERRENKUNDE
Celestijnenlaan 200d bus 2412
3001 HEVERLEE, BELGIË
tel. + 32 16 32 71 24
fys.kuleuven.be